Supplementary Information (SI) for Physical Chemistry Chemical Physics.

Intermolecular interaction potential maps from energy decomposition for interpreting reactivity and intermolecular interactions

Amin Kiani,[†,‡] Wentong Zhou,[†,‡] and Lawrence M. Wolf[*,†]

†*Department of Chemistry, University of Massachusetts, Lowell, MA, 01854, United States*

‡*These authors contributed equally to this work*

E-mail: lawrence_wolf@uml.edu

List of Figures

List of Tables

1. IMIP surfaces generated using NOCV-ETS and xTB-iff EDA

Depicted in **Figure S1** are surfaces generated using the NOCV-ETS EDA and xTB-IFF EDA schemes for comparison. The provided surfaces are of aniline using a CH_3^+ probe. The ortho- and para-regions of aniline (excluding the amino nitrogen) are identified as the most favorable interaction sites on both surfaces. This aligns with experimental observations and demonstrates qualitative consistency between the two EDA methods. As expected, some minor quantitative differences can be traced to differences in the two decomposition schemes. Furthermore, a brief introduction to both these methods is presented here:

Within the xTB-IFF EDA scheme, the total interaction energy (ΔE_{int}) of two systems can be divided into repulsion (ΔE_{rep}), electrostatic (ΔE_{elec}), dispersion (ΔE_{disp}), induction (ΔE_{ind}), and charge transfer (ΔE_{CT}) energies.

In the NOCV-ETS EDA scheme implemented in Orca, the total interaction energy can be divided into distortion(ΔE_{dist}), electrostatic (ΔE_{elec}), Pauli repulsion (ΔE_{rep}), and orbital interaction (ΔE_{orb}). The orbital interaction can be further decomposed using eigenvalue pairs derived from the deformed density matrix. This analysis offers insights into the nature of bonding, revealing regions of electron density depletion and gain. From this gain or depletion of electron density, the degree and energetics of bonding and back-bonding interactions between the fragments can be determined.

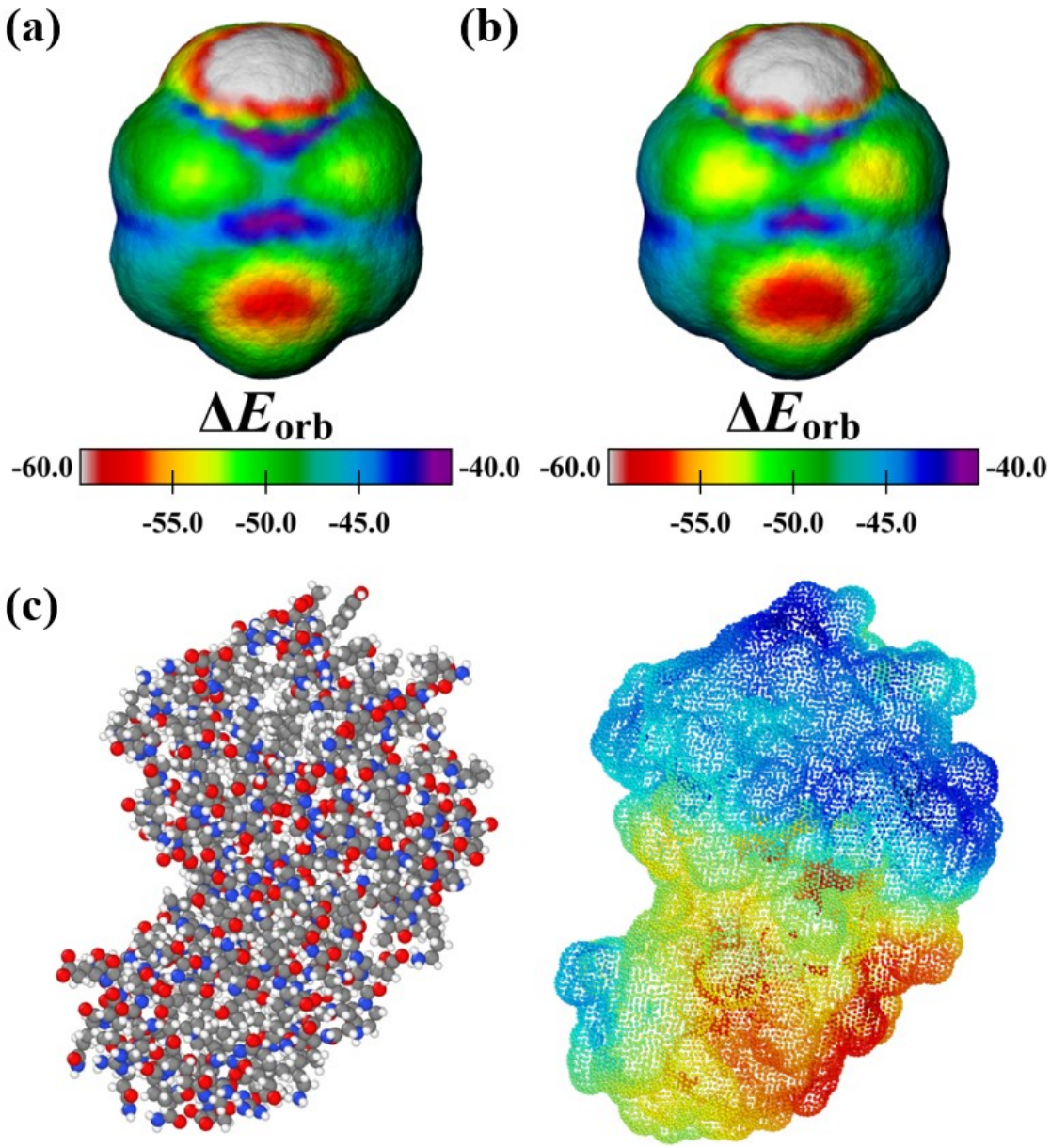

Figure S1. ΔE_{orb} surfaces of aniline generated using a $CH_3{}^+$ probe within the (a) NOCV-ETS EDA and (b) LMO-EDA framework framework (r^2-SCAN); (c) The ball-stick model of the Barnase-Barstar protein complex (left) and its corresponding ΔE_{int} surface generated with Li^+ probe within the xTB-iFF framework (right).

2. Variable probes and their usages

A variety of probes designed to investigate distinct interaction types within molecular systems are incorporated into our Python package (**Figure S2**). For example, metal (M^+) and halogen (X^-) probes can be employed for studying cation-π and anion-π interactions, respectively. For electrophilic interactions, the $CH_3{}^+$ probe is ideal as it maps interaction with electron-rich areas of π electron density. In contrast, the $CH_3{}^-$ probe is best suited for probing electron-deficient regions of a molecule. SH^-, being a softer nucleophile than $CH_3{}^-$ can also serve as a nucleophilic probe. The acetylene (C_2H_2) and ethylene (C_2H_4) probes can be used for examining ligand interactions in transition metal complexes. The benzene probe is ideal for investigating π-stacking, polar-π, cation-π, anion-π, and lone pair-π interactions. Additionally, the carbon monoxide (CO) probe can be used to assess bonding and back-bonding interactions in transition metal complexes. Finally, BH_3 and BF_3 can be used as Lewis acid probes. Additional probes can readily be included. Each probe is oriented perpendicular to the tangential plane of the surface being investigated. This orientation is illustrated in **Figure S2** by blue arrows. The placement of these arrows about the molecular structure indicates the point used to align and orient the probe. Once positioned, each molecular probe undergoes a semi-empirical (xTB) rigid rotor scan about the normal vector to obtain a minimum energy probe orientation.

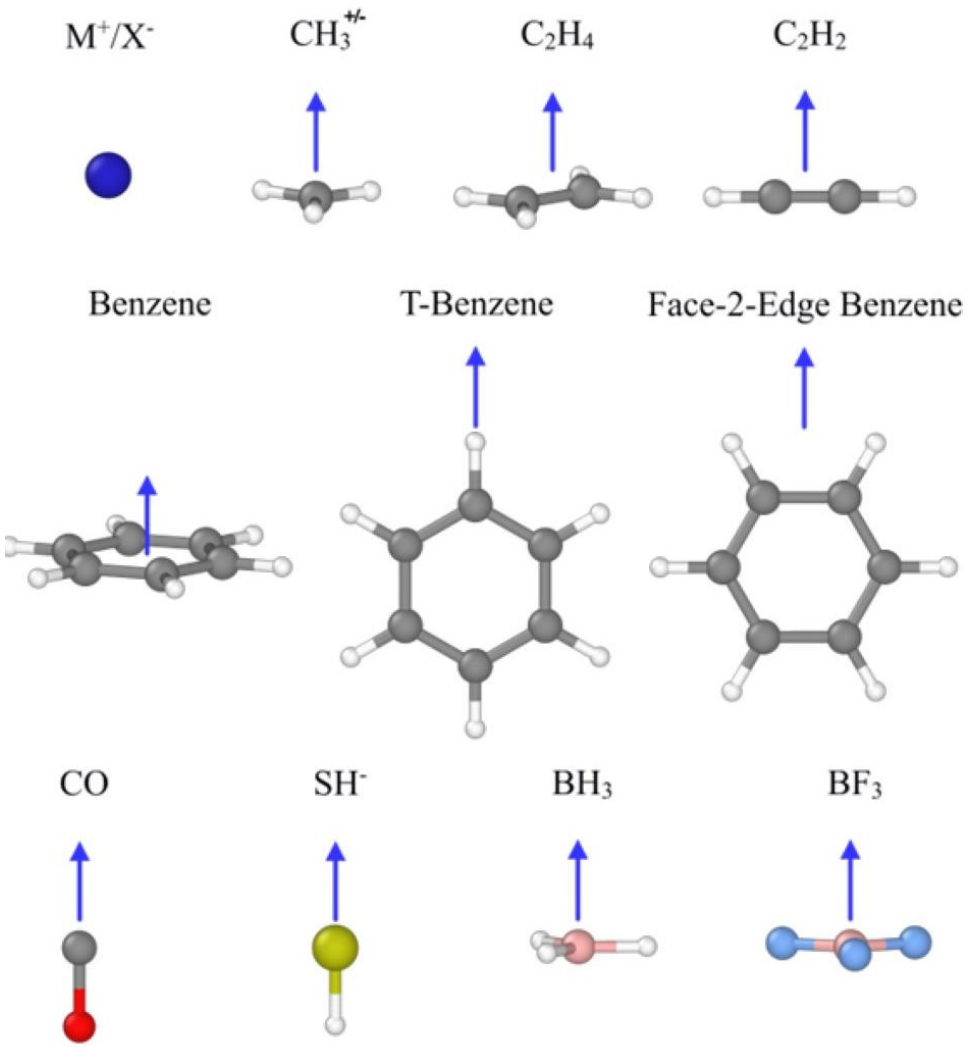

Figure S2. Probes and their geometries. Blue arrows indicate the alignment/orientation of probes toward the surface.

3. Spherical grid generation

The visualization of probes around a benzene molecule, as depicted in **Figure S3**, uses the Fibonacci sphere algorithm. The placement of probes around each atom follows the Fibonacci sphere distribution, with radii based on the atomic van der Waals radii. The number of probes can be fine-tuned, and those intersecting with neighboring atoms are removed to avoid overlap.

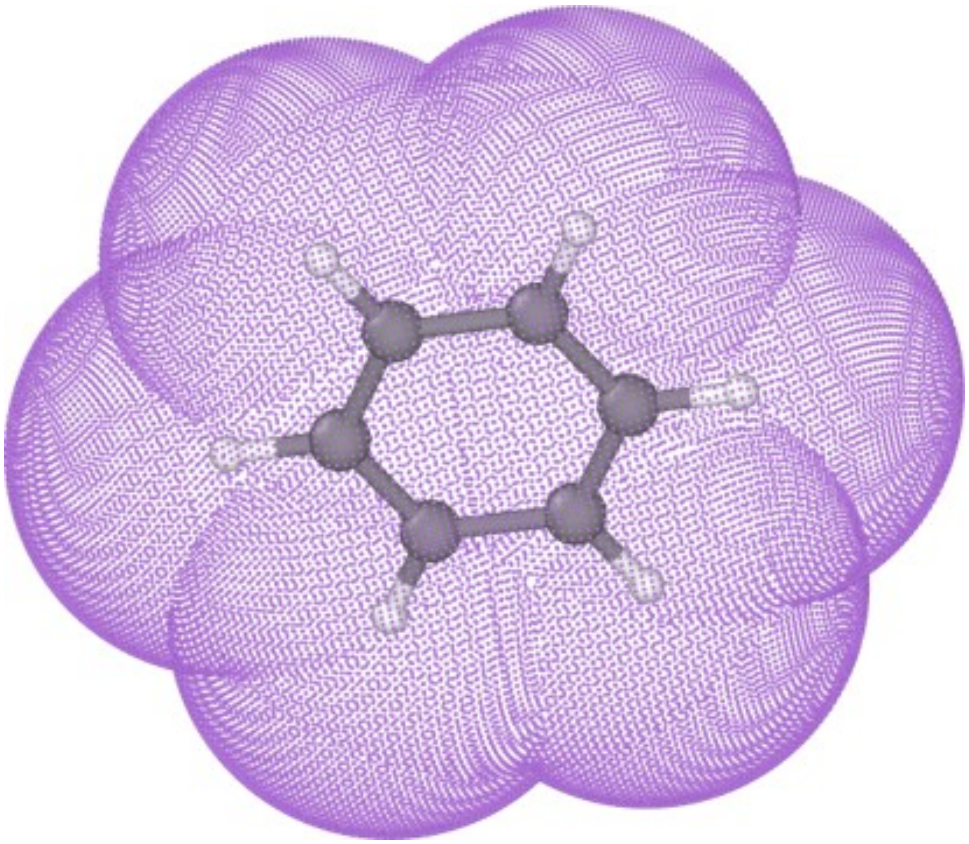

Figure S3. Spherical grid generated around benzene using the Fibonacci sphere algorithm.

4. Overview of IMIP map generation

An overview of the method used for surface generation is given in **Figure S4**. Benzene is used as an example using a CH_3^+ probe for surface generation. Initially, a sparse cubic grid is generated around the molecule (**Figure S4** (**a**, **b**)). For each grid point, the electron density is computed using Multiwfn, and the results are exported from wave function files and stored in the Molden format. An isodensity range is then set to filter off points (**Figure S4** (**c**)). Subsequently, a volume element is created for each remaining grid point, and within this volume, a finer grid is constructed and filtered. This refined grid captures grid points with a narrow electron density range (**Figure S4** (**d**, **e**, **f**)). After grid generation and filtration, probes are positioned at each grid point. Single-atom probes are positioned without ambiguity. If molecular probes are used, their alignment would be determined by vectors normal to the tangential plane of each grid point on the molecular surface (**Figure S4** (**g**)). This definition is intended to account for the orbital directionality of molecular probes. The normal vectors are computed using the Open3D Python library. Open3D estimates the normal vectors on the surface by statistical analysis of neighboring grid points. By combining this approach with a rigid rotor scan using GFN2-xTB (**Figure S4** (**g**)), the lowest energy orientation of the probe can be determined in a reasonable time frame. At this point, EDA computations are conducted on the grid points, and their corresponding energy values are stored as extended xyz files and used to construct the surfaces using Ovito Pro software (**Figure S4** (**h**, **i**)).

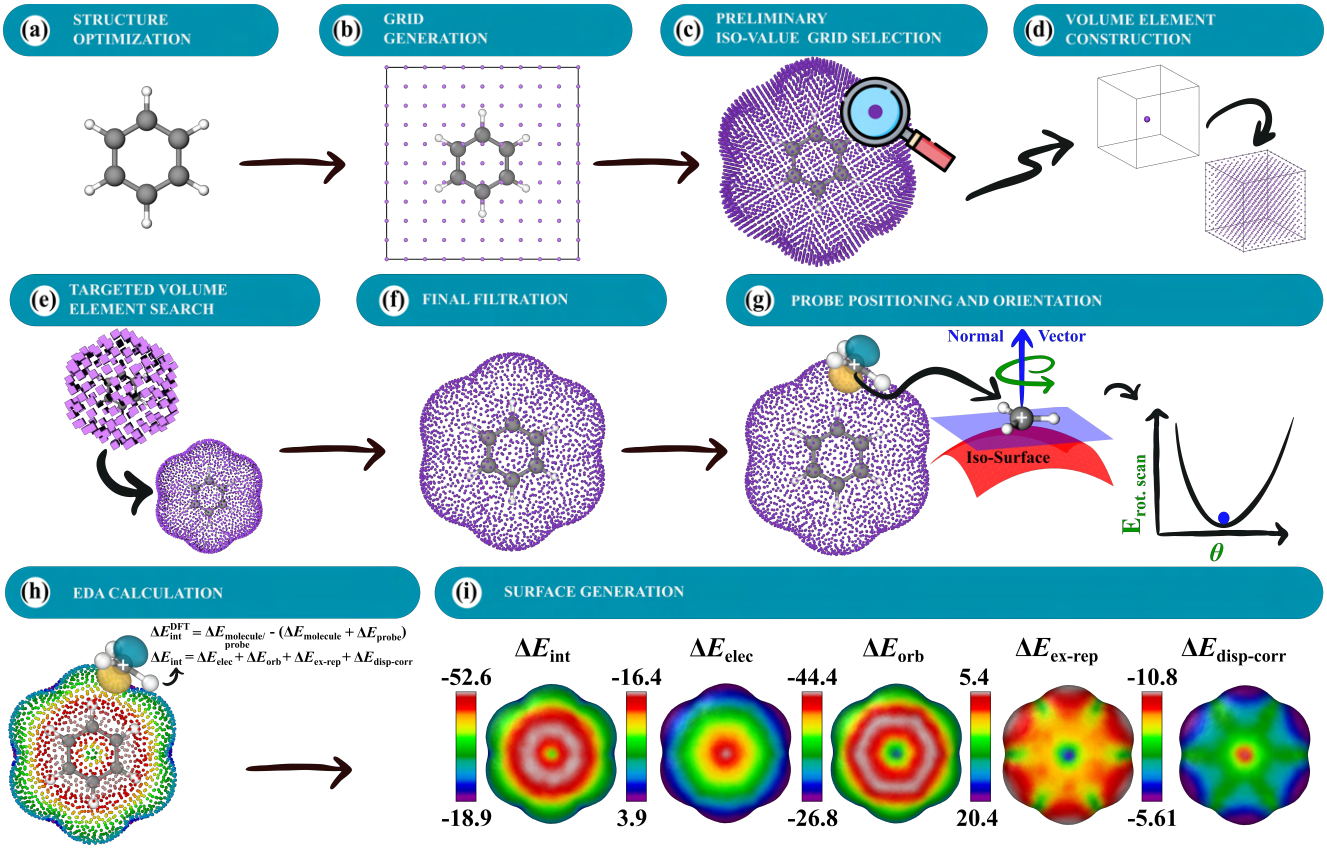

Figure S4. Overview of methodology for IMIP map generation (a) structure optimization (b) grid generation (c) preliminary isodensity selection (d) volume element construction (e) volume element search (f) final filtration (g) probe positioning and orientation (h) EDA calculation (i) surface generation (units: kcal/mol).

5. Dependence of IMIP surfaces on basis sets and functionals

It can be shown that IMIP surfaces using different sized basis sets or functionals are qualitatively similar. (**Figure S5**). Comparison of the surfaces for r^{2}SCAN/def2-SVP to r^{2}SCAN/def2-TZVP shows little difference between the surfaces. While the absolute values between different functionals differ slightly (cf. r^{2}SCAN to B3LYP), the qualitative trends hold.

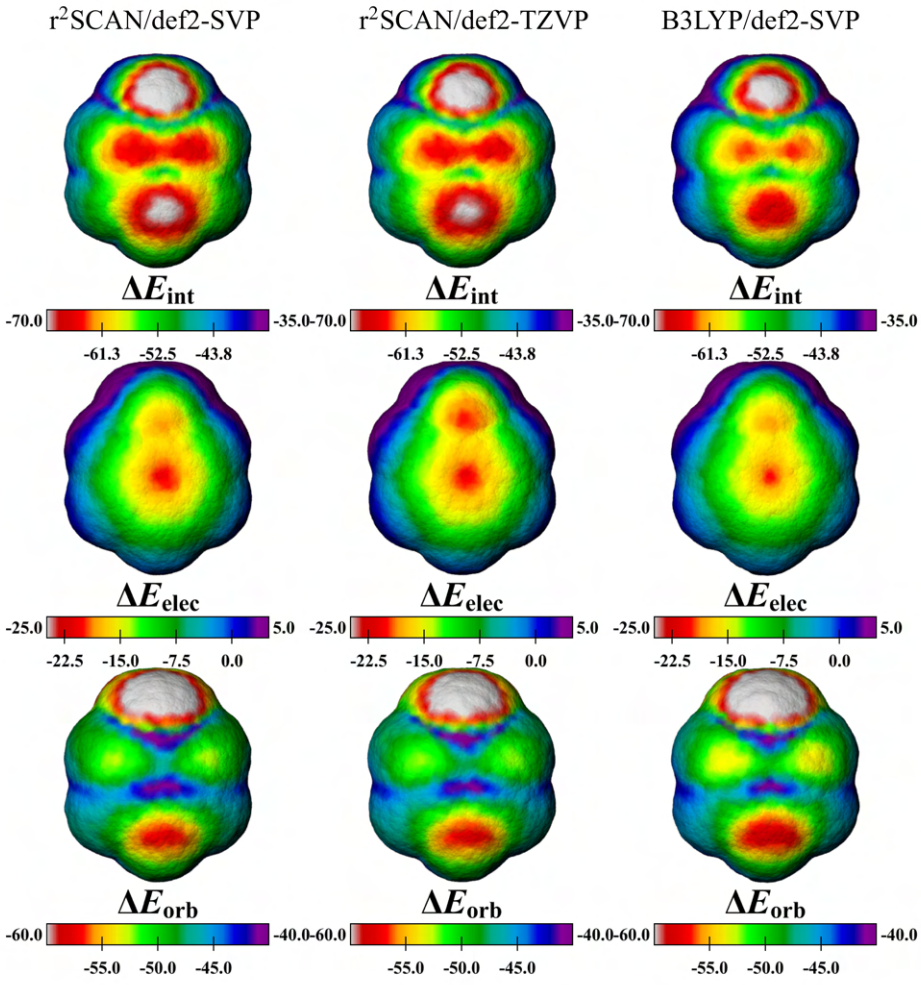

Figure S5. ΔE_{int}, ΔE_{elec}, and ΔE_{orb} surfaces of aniline generated at the r^{2}SCAN/def2-SVP, r^{2}SCAN/def2-TZVP, and B3LYP/def2-SVP level of theory, within the LMO-EDA framework.

6. Comparing IMIP surfaces generated from probe orientations via xTB and DFT scans

When molecular probes were employed, the lowest energy orientation of the probe was identified through a rigid rotor scan using the GFN2-xTB method. The comparison between molecular probe-based surfaces generated using GFN2-xTB and r^{2}SCAN/def2-SVP rotor scans shows qualitative consistency (**Figure S6**), suggesting that the faster semi-empirical xTB scans can replace the more costly DFT scans for determining probe orientations.

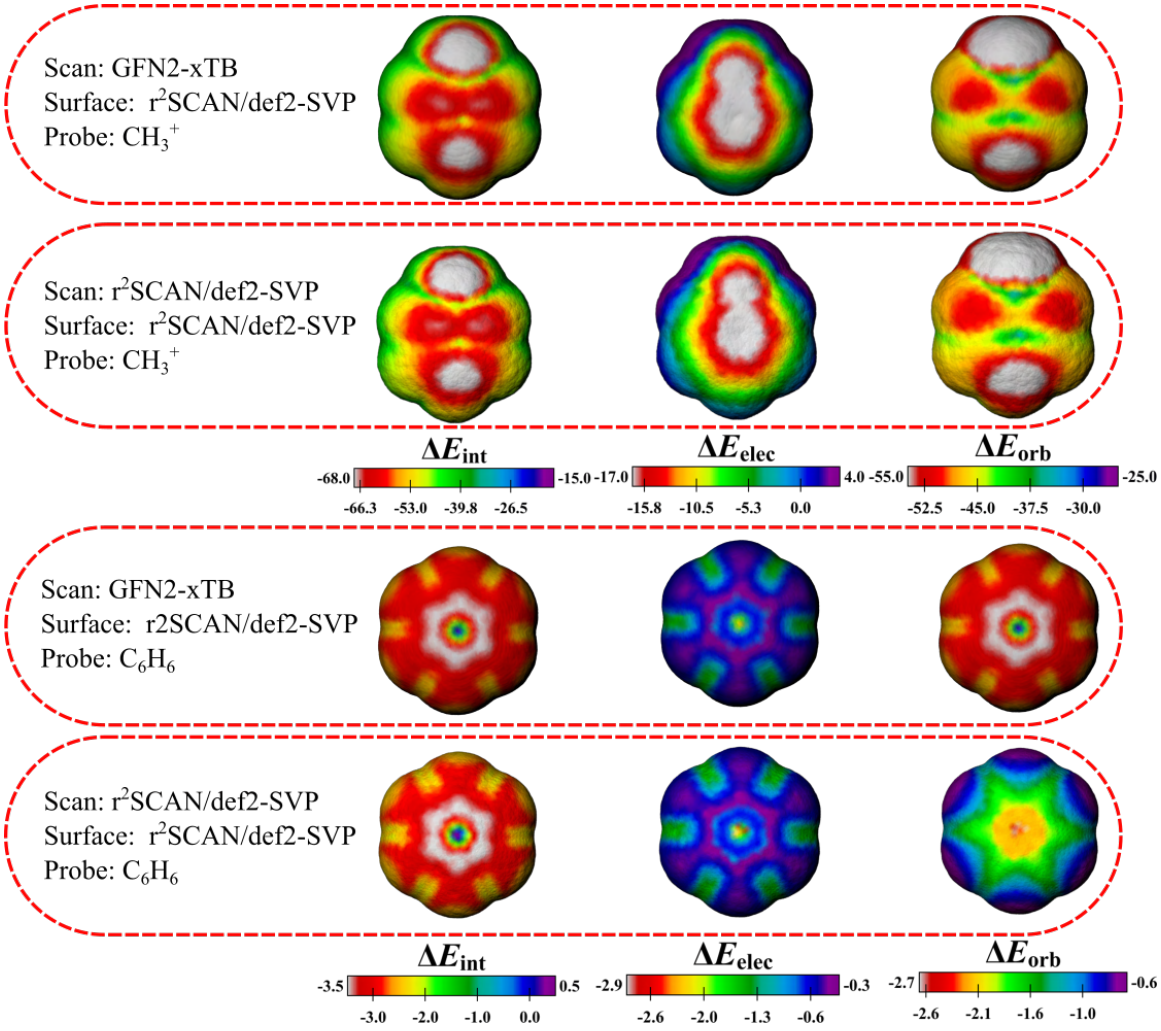

Figure S6. ΔE_{int}, ΔE_{elec}, and ΔE_{orb} surfaces of aniline (first and second rows) with CH_3^+ probe, and benzene (third and fourth rows) with stacked C_6H_6 probe. xTB scans (first and third rows), DFT scans (second and fourth rows).

7. ΔE_{int}, ΔE_{elec}, ΔE_{orb}, and σ^+ values for EAS Hammett plots

Table S1 lists ΔE_{int}, ΔE_{elec}, ΔE_{orb}, and σ^+ values used to generate Hammett plots shown in **Figure 6** (EAS section) in the main manuscript. ΔE_{int} and ΔE_{orb} show a stronger correlation with relative reactivity patterns observed in the literature than ΔE_{elec}. ΔE_{int}, ΔE_{elec}, and ΔE_{orb} values were collected at the most favorable ΔE_{int} sites within the para regions of the π systems.

Table S1. ΔE_{int}, ΔE_{elec}, and ΔE_{orb} (kcal/mol) and σ^+ values of variable mono-substituted benzene derivatives (and benzene). Energies were obtained at the para-positions of the π systems.

Groups	ΔE_{int}	ΔE_{elec}	ΔE_{orb}	σ^+
$N(CH_3)_2$	-77.4595	-14.86750	-61.8911	-1.70
NH_2	-70.2927	-14.34040	-56.1900	-1.30
$NHC(O)CH_3$	-63.7592	-10.53960	-53.7226	-0.60
OCH_3	-63.3863	-11.18530	-52.6538	-0.78
OH	-60.0525	-10.15930	-52.3355	-0.92
tBu	-59.5491	-11.15340	-48.5984	-0.26
iPr	-58.7684	-11.94530	-47.2946	-0.28
Propyl	-58.7562	-11.35270	-47.7845	-0.29
Ethyl	-57.9687	-11.15960	-47.3228	-0.30
CH_3	-57.7466	-11.15460	-46.8313	-0.31
$OC(O)CH_3$	-57.1349	-9.40318	-48.2091	-0.19
Br	-53.0551	-5.93261	-47.0005	0.15
H	-52.5277	-1.04272	-42.9562	0.00
Cl	-52.2368	-6.97245	-45.6446	0.11
F	-51.9715	-6.84082	-45.5959	-0.07
CHO	-45.4417	-4.64978	-42.0392	0.73
COOH	-43.6908	-1.84148	-42.7697	0.42
CF_3	-43.5836	-3.91859	-40.9728	0.61
CN	-43.3605	-1.24201	-43.3159	0.66
NO_2	-39.7259	-0.74441	-40.1554	0.79

8. Cation-π IMIP surfaces of benzene, naphthalene, anthracene, phenanthrene, and anthracene

Figures S7-S14 depict surfaces for benzene, naphthalene, anthracene, phenanthrene, and tetracene generated using Li^+, Na^+, K^+, Be^{2+}, Mg^{2+}, Ca^{2+}, Ag^+, and Zn^{2+}. The focus is on how these metal ions, varying in size and charge, interact within the π systems. The isodensity values used in each metal-PAH system are derived from those optimized isodensities between benzene and each respective probe (**Table S2**). This allows for comparing energy values between different molecules using the same probe. These figures include all energy components.

Table S2. Isodensities of various cation probes based on optimized interactions with benzene.

Probe	Li^+	Na^+	K^+	Be^{2+}	Ca^{2+}	Ag^{2+}	Zn^+
Isodensity	7.52×10^{-4}	9.15×10^{-6}	8.21×10^{-5}	3.15×10^{-3}	1.32×10^{-4}	1.93×10^{-4}	5.49×10^{-4}

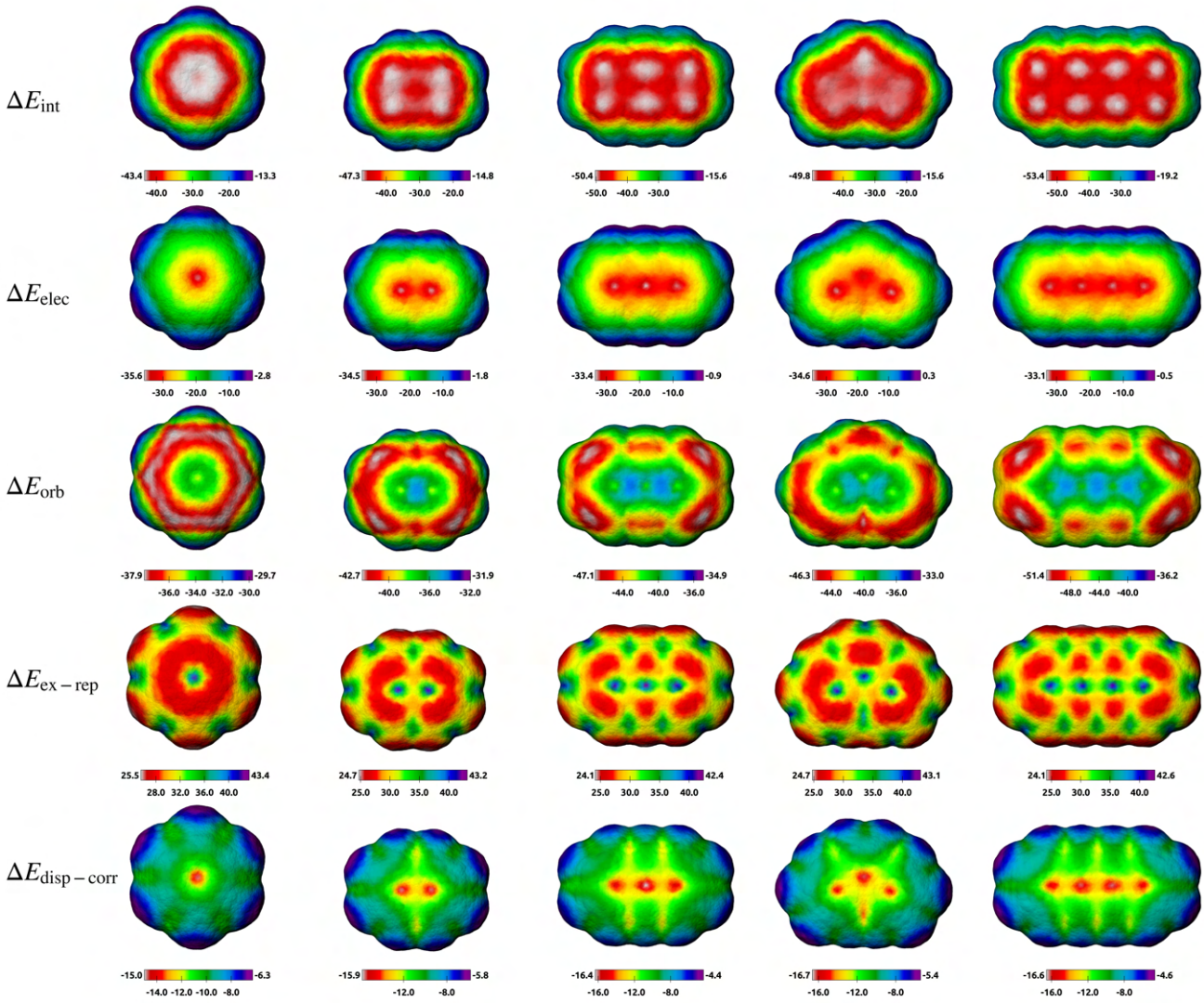

Figure S7. ΔE_{int}, ΔE_{elec}, ΔE_{orb}, $\Delta E_{\text{ex-rep}}$, and $\Delta E_{\text{disp-corr}}$ surfaces of benzene, naphthalene, anthracene, phenanthrene, and tetracene; Ag^+ probe.

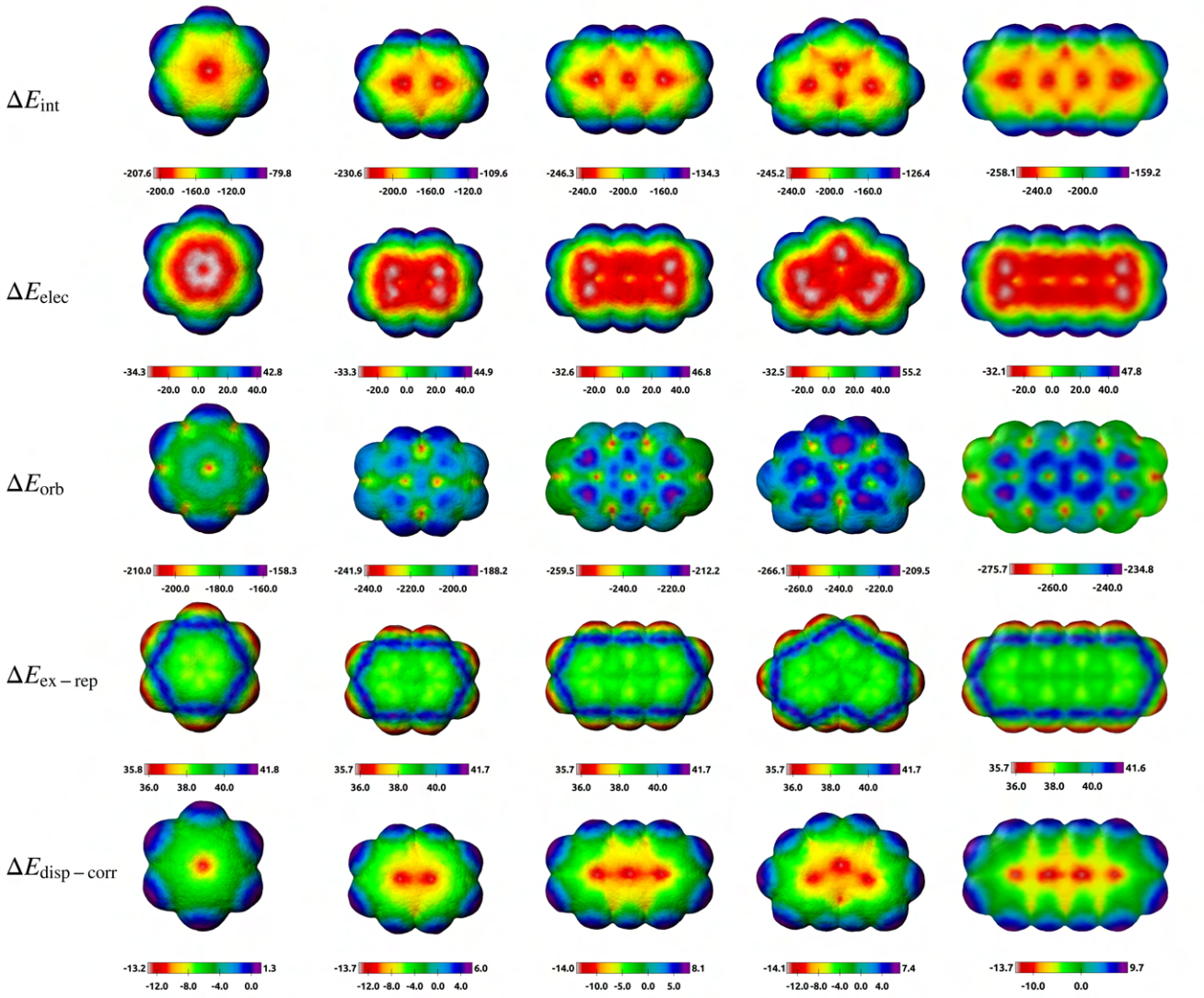

Figure S8. ΔE_{int}, ΔE_{elec}, ΔE_{orb}, $\Delta E_{\text{ex-rep}}$, and $\Delta E_{\text{disp-corr}}$ surfaces of benzene, naphthalene, anthracene, phenanthrene, and tetracene; Be^{2+} probe.

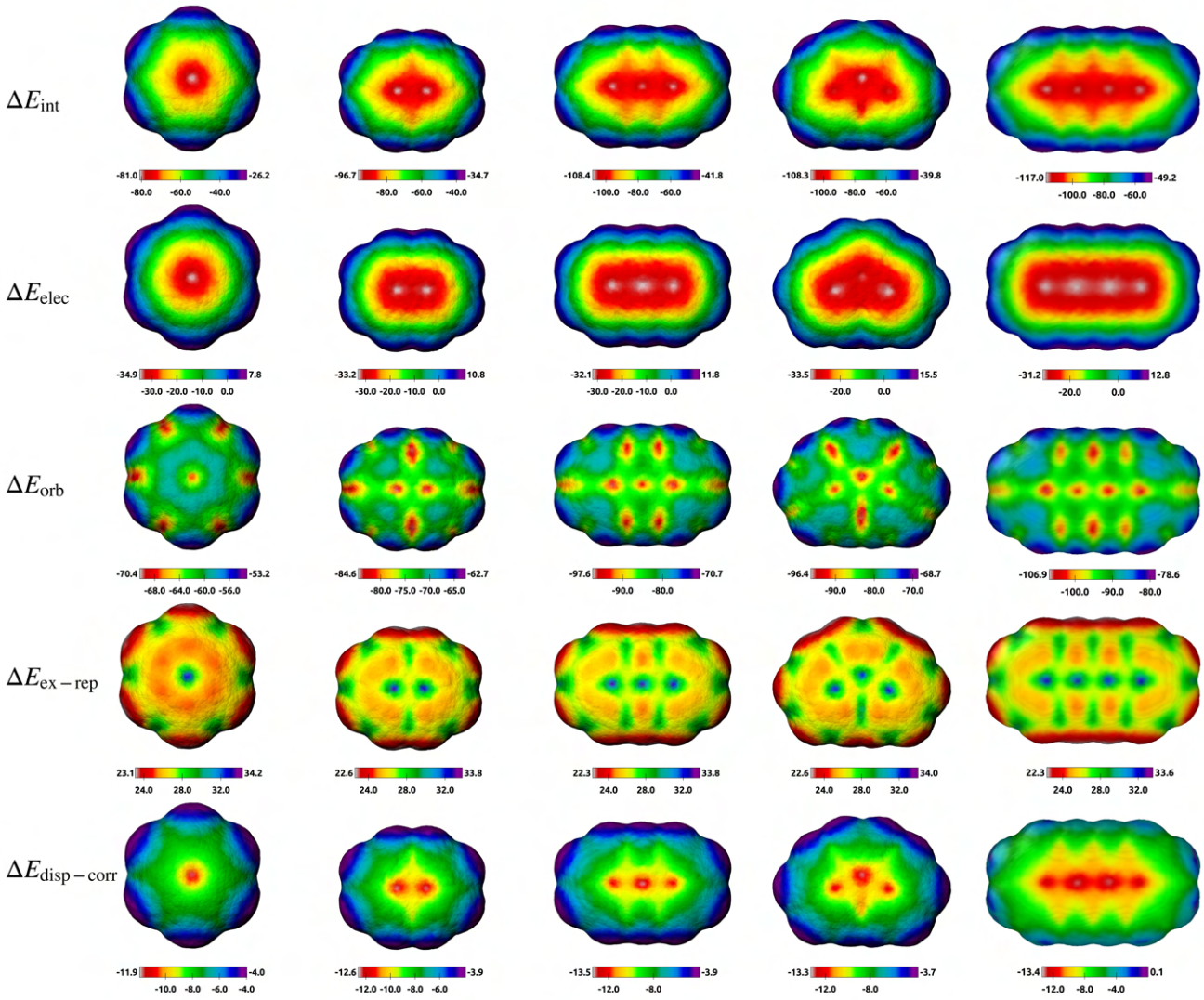

Figure S9. ΔE_{int}, ΔE_{elec}, ΔE_{orb}, $\Delta E_{\text{ex}-\text{rep}}$, and $\Delta E_{\text{disp}-\text{corr}}$ surfaces of benzene, naphthalene, anthracene, phenanthrene, and tetracene; Ca^{2+} probe.

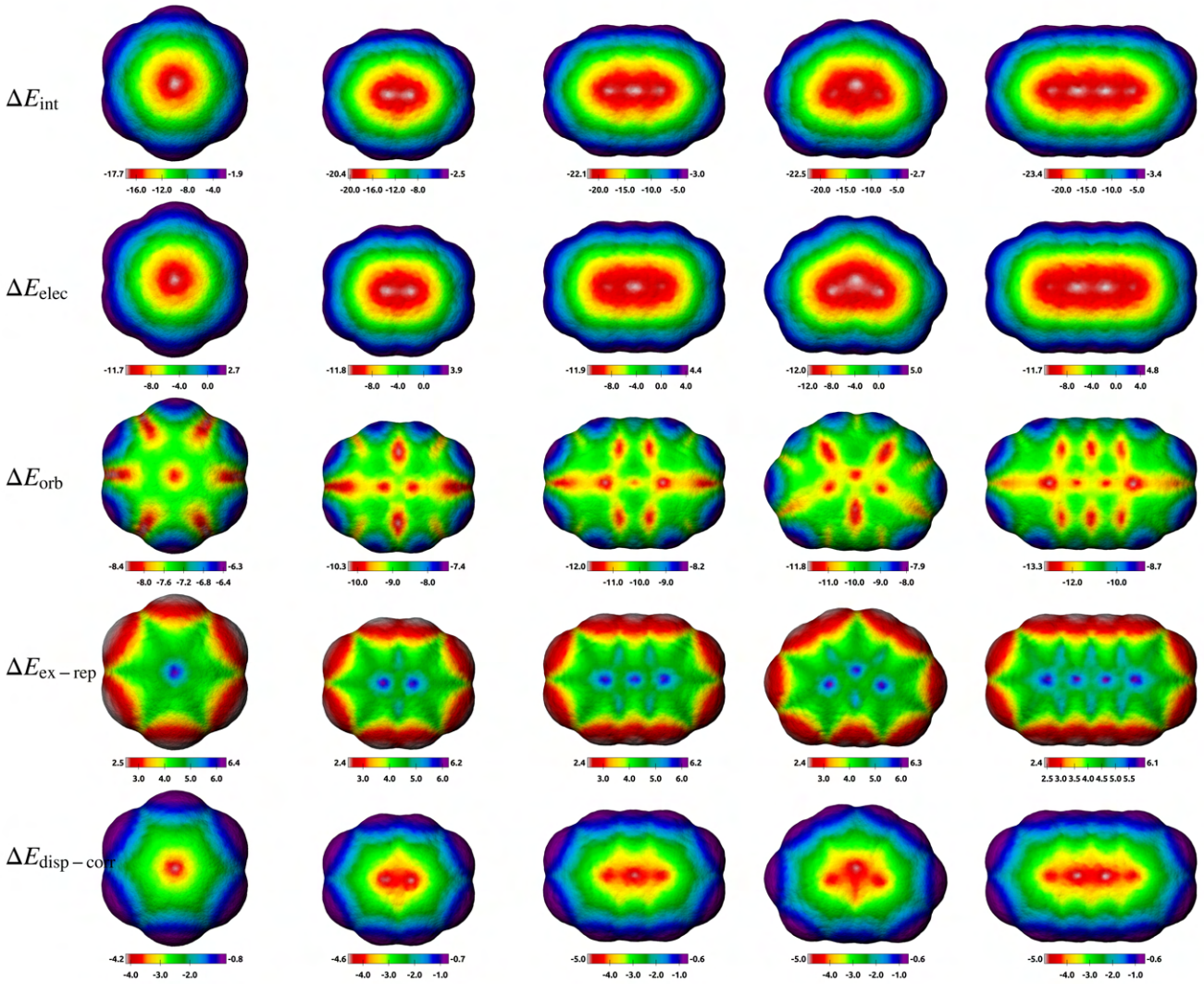

Figure S10. ΔE_{int}, ΔE_{elec}, ΔE_{orb}, $\Delta E_{\text{ex-rep}}$, and $\Delta E_{\text{disp-corr}}$ surfaces of benzene, naphthalene, anthracene, phenanthrene, and tetracene; K^+ probe.

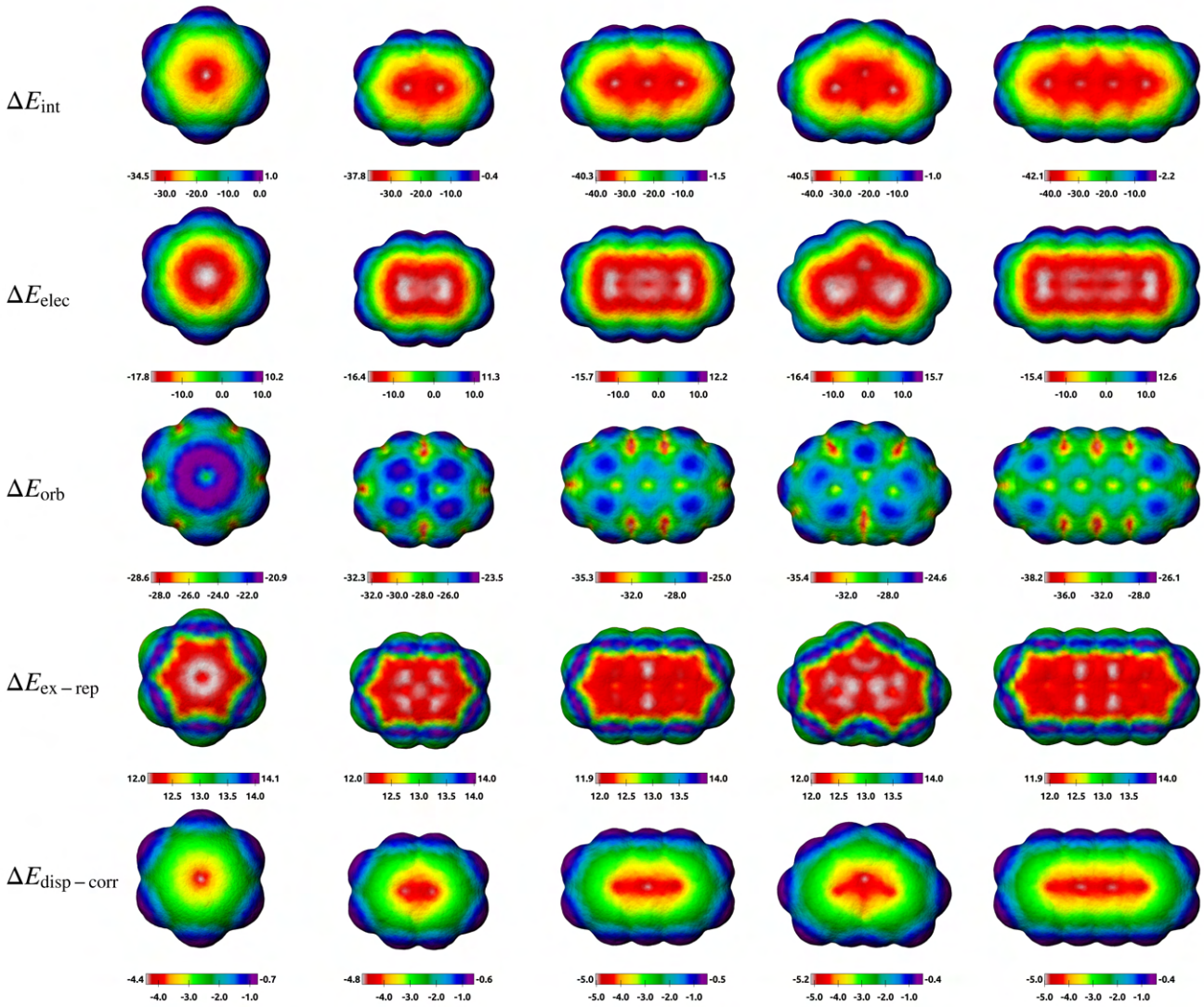

Figure S11. ΔE_{int}, ΔE_{elec}, ΔE_{orb}, $\Delta E_{\text{ex-rep}}$, and $\Delta E_{\text{disp-corr}}$ surfaces of benzene, naphthalene, anthracene, phenanthrene, and tetracene; Li^+ probe.

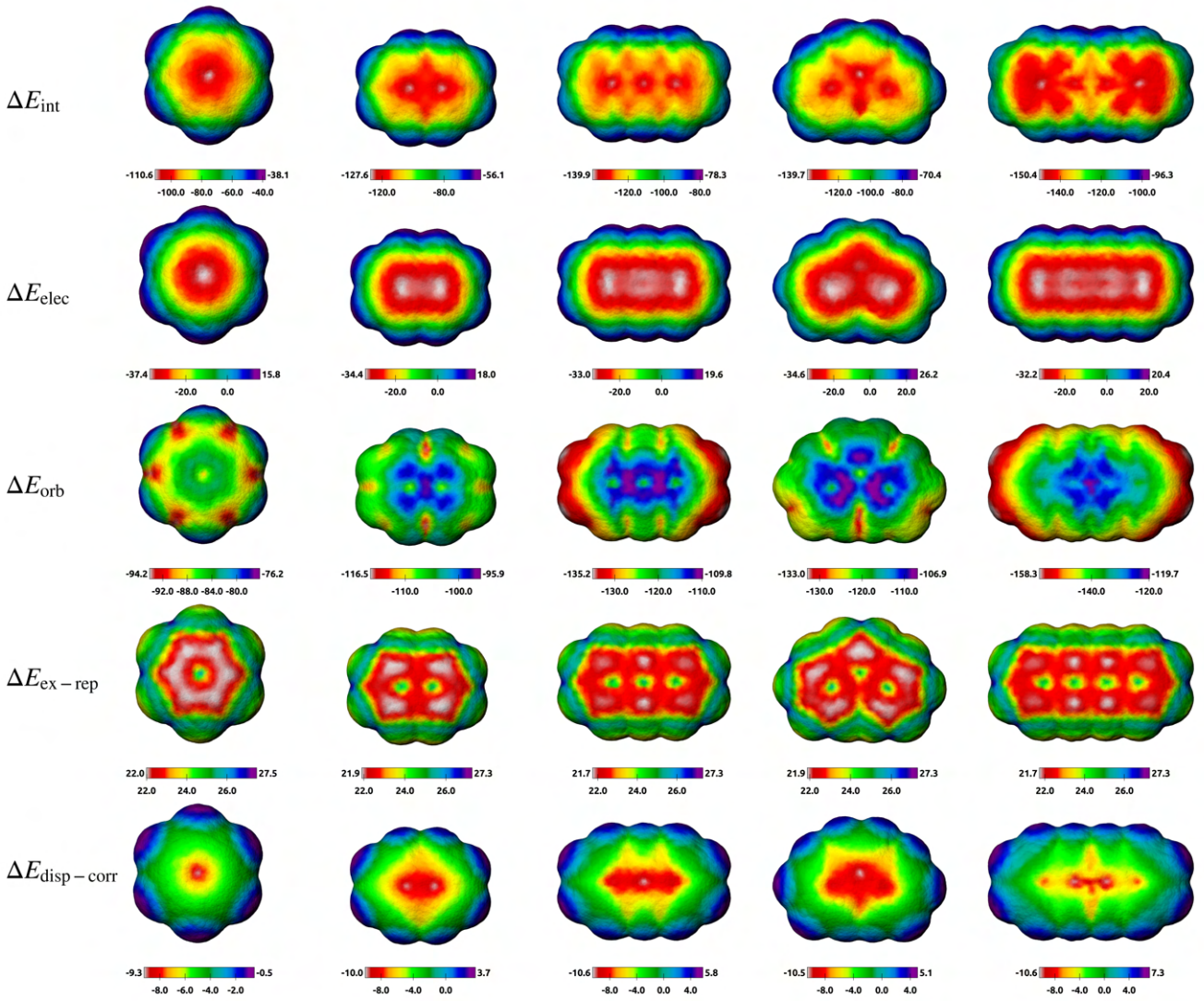

Figure S12. ΔE_{int}, ΔE_{elec}, ΔE_{orb}, $\Delta E_{\text{ex-rep}}$, and $\Delta E_{\text{disp-corr}}$ surfaces of benzene, naphthalene, anthracene, phenanthrene, and tetracene; Mg^{2+} probe.

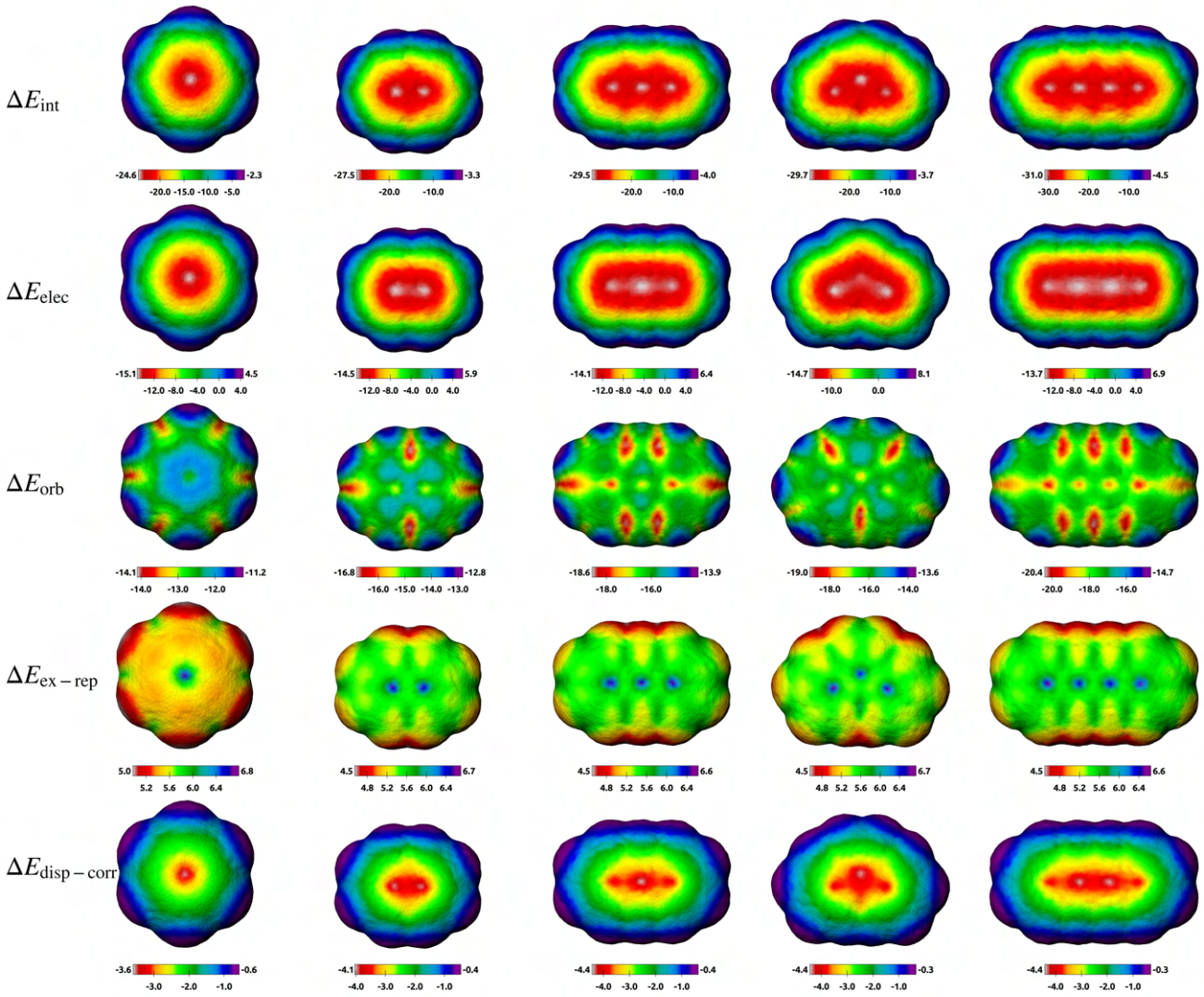

Figure S13. ΔE_{int}, ΔE_{elec}, ΔE_{orb}, $\Delta E_{\text{ex-rep}}$, and $\Delta E_{\text{disp-corr}}$ surfaces of benzene, naphthalene, anthracene, phenanthrene, and tetracene; Na^+ probe.

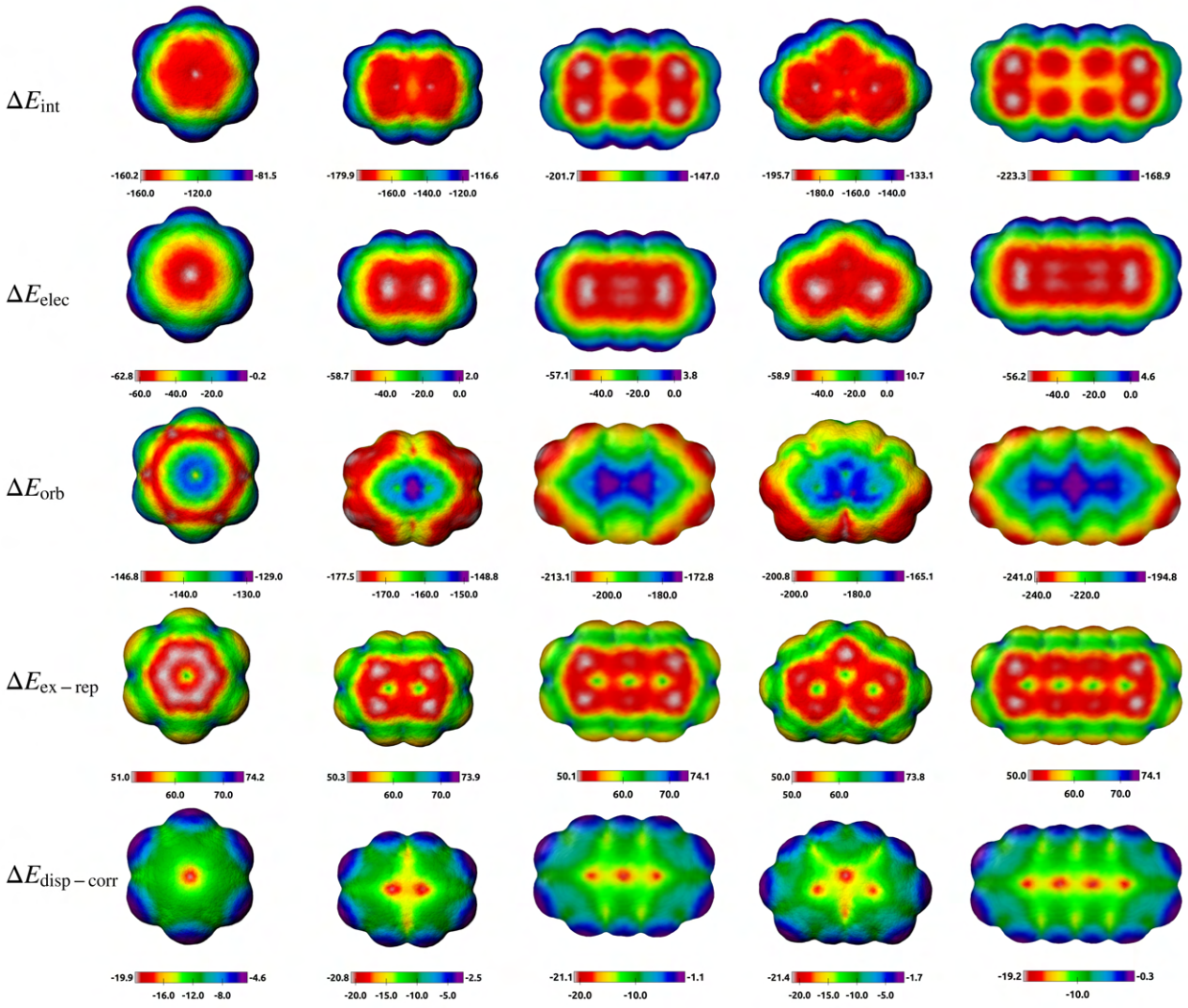

Figure S14. ΔE_{int}, ΔE_{elec}, ΔE_{orb}, $\Delta E_{\text{ex-rep}}$, and $\Delta E_{\text{disp-corr}}$ surfaces of benzene, naphthalene, anthracene, phenanthrene, and tetracene; Zn^{2+} probe.

9. IMIP surfaces between benzene derivatives and cation probes

Figures S15-S50 depict surfaces for benzene and several of its derivatives (R-Ph). This list includes: Iodo-benzene, bromo-benzene, chloro-benzene, fluoro-benzene, toluene, benzaldehyde, cyano-benzene, ethylbenzene, cumene, benzamide, aniline, nitrobenzene, anisole, acetoxy benzene, phenol, propyl benzene, thiophenol, benzenesulfonic acid and tert-butylbenzene, and benzotrifluoride. The isodensities used to generate each surface were based on the optimized values between benzene and the metal cation probe, as detailed in **Table S2**.

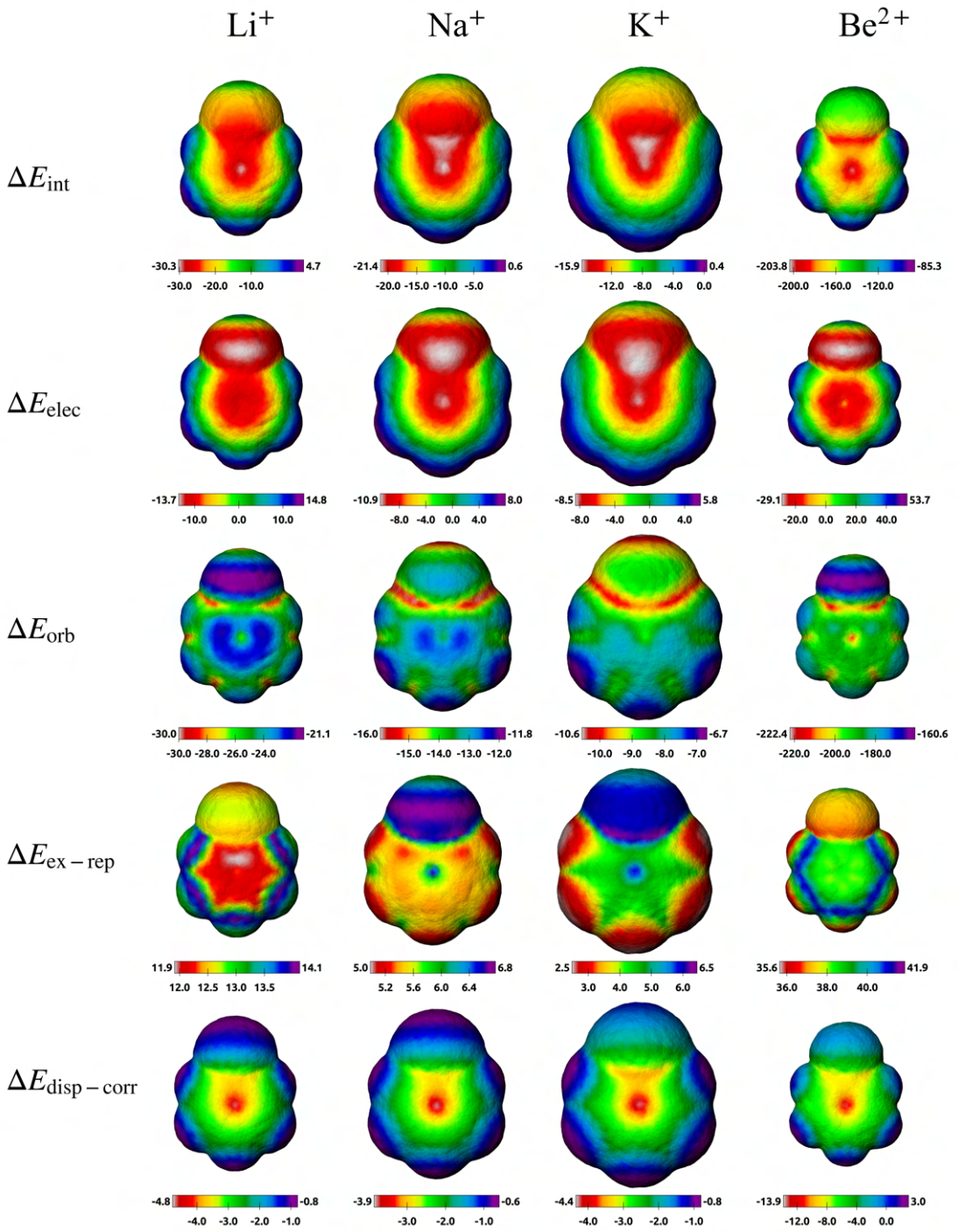

Figure S15. ΔE_{int}, ΔE_{elec}, ΔE_{orb}, $\Delta E_{\text{ex-rep}}$, and $\Delta E_{\text{disp-corr}}$ surfaces of bromobenzene with Li^+, Na^+, K^+, Be^{2+} probes.

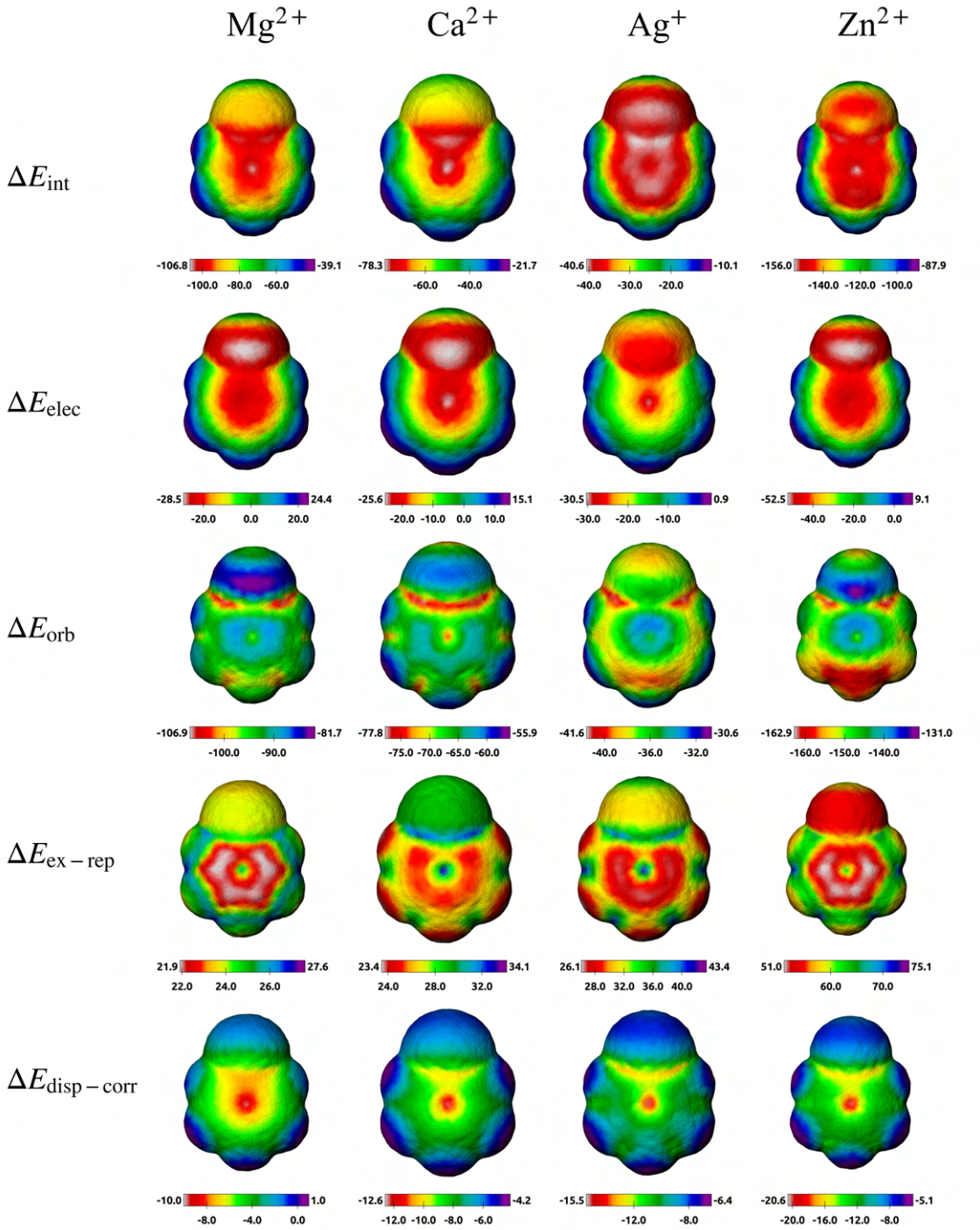

Figure S16. ΔE_{int}, ΔE_{elec}, ΔE_{orb}, $\Delta E_{\text{ex-rep}}$, and $\Delta E_{\text{disp-corr}}$ surfaces of bromobenzene with Mg^{2+}, Ca^{2+}, Ag^{+}, Zn^{2+} probes.

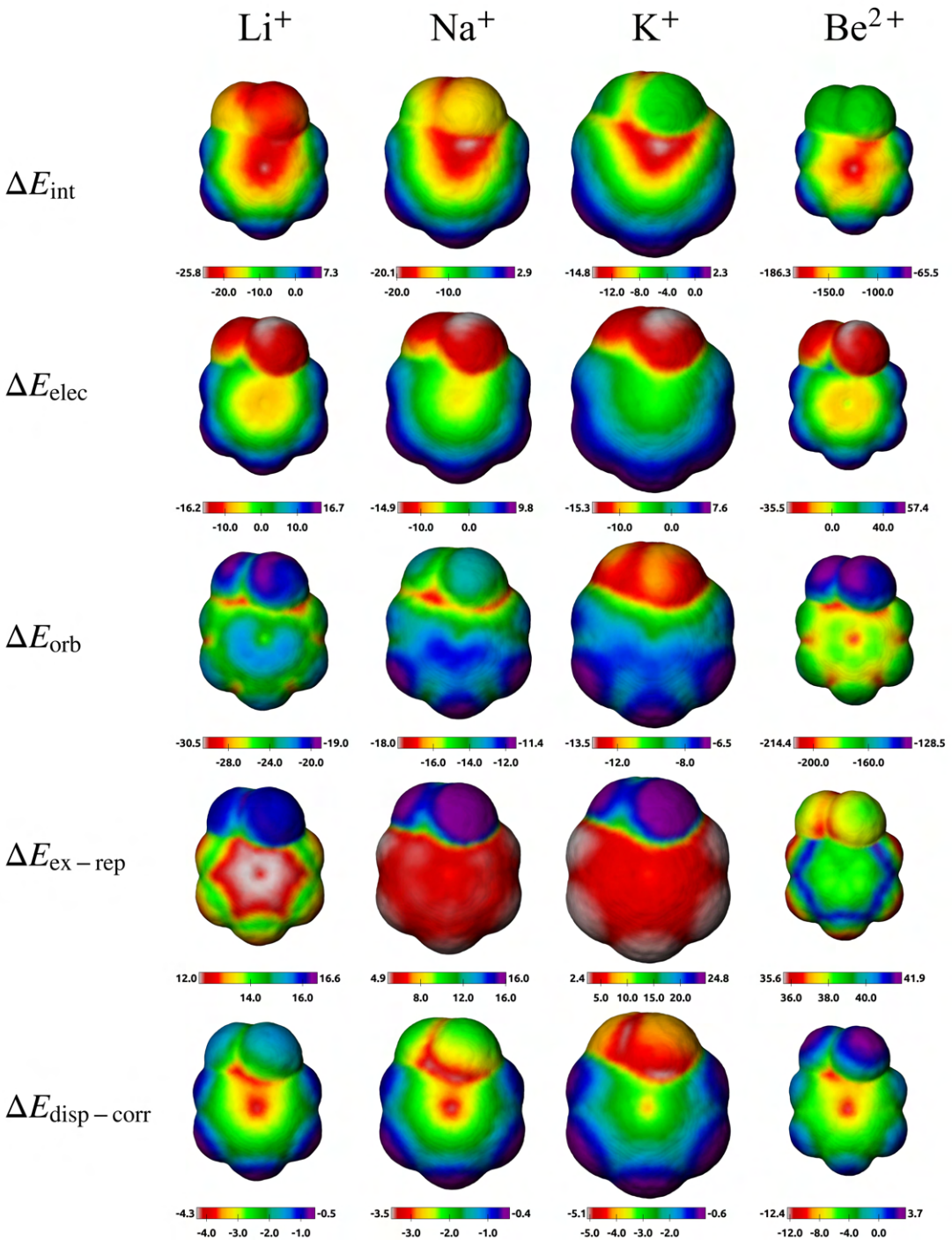

Figure S17. ΔE_{int}, ΔE_{elec}, ΔE_{orb}, $\Delta E_{\text{ex-rep}}$, and $\Delta E_{\text{disp-corr}}$ surfaces of trifluorotoluene with Li^+, Na^+, K^+, Be^{2+} probes.

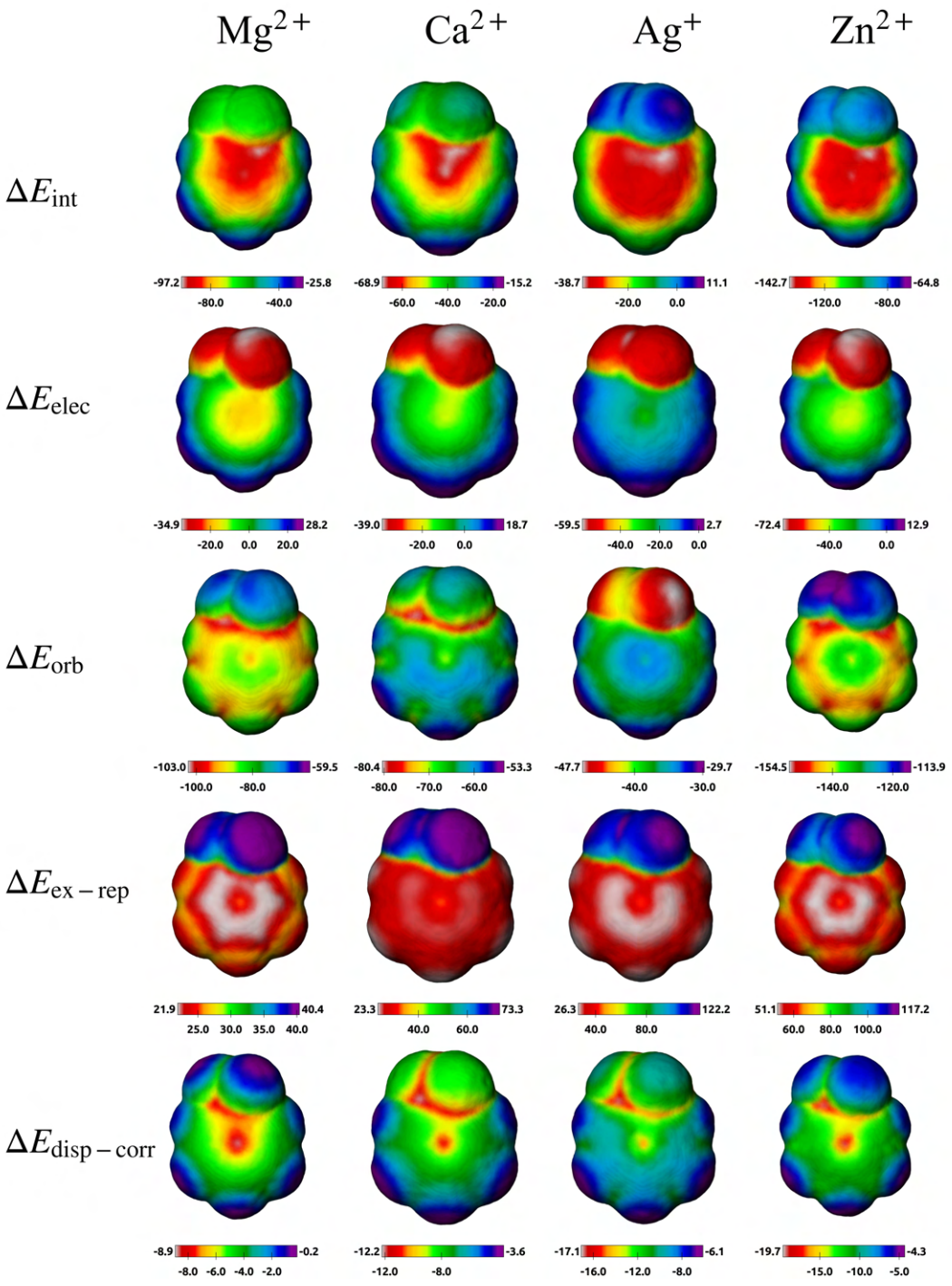

Figure S18. ΔE_{int}, ΔE_{elec}, ΔE_{orb}, $\Delta E_{\text{ex-rep}}$, and $\Delta E_{\text{disp-corr}}$ surfaces of trifluorotoluene with $Mg^{2+}, Ca^{2+}, Ag^{+}, Zn^{2+}$ probes.

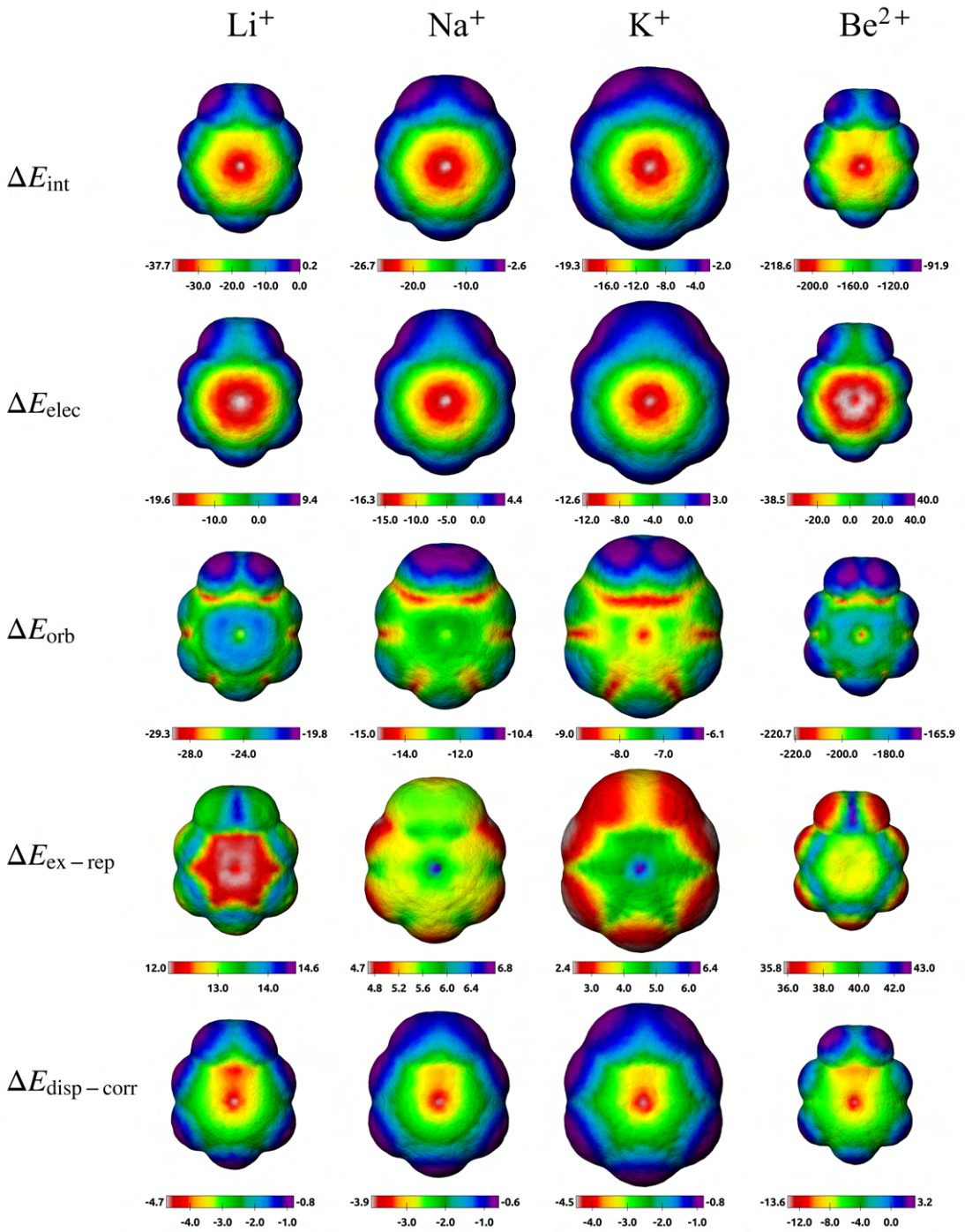

Figure S19. ΔE_{int}, ΔE_{elec}, ΔE_{orb}, $\Delta E_{\text{ex-rep}}$, and $\Delta E_{\text{disp-corr}}$ surfaces of toluene with Li^+, Na^+, K^+, Be^{2+} probes.

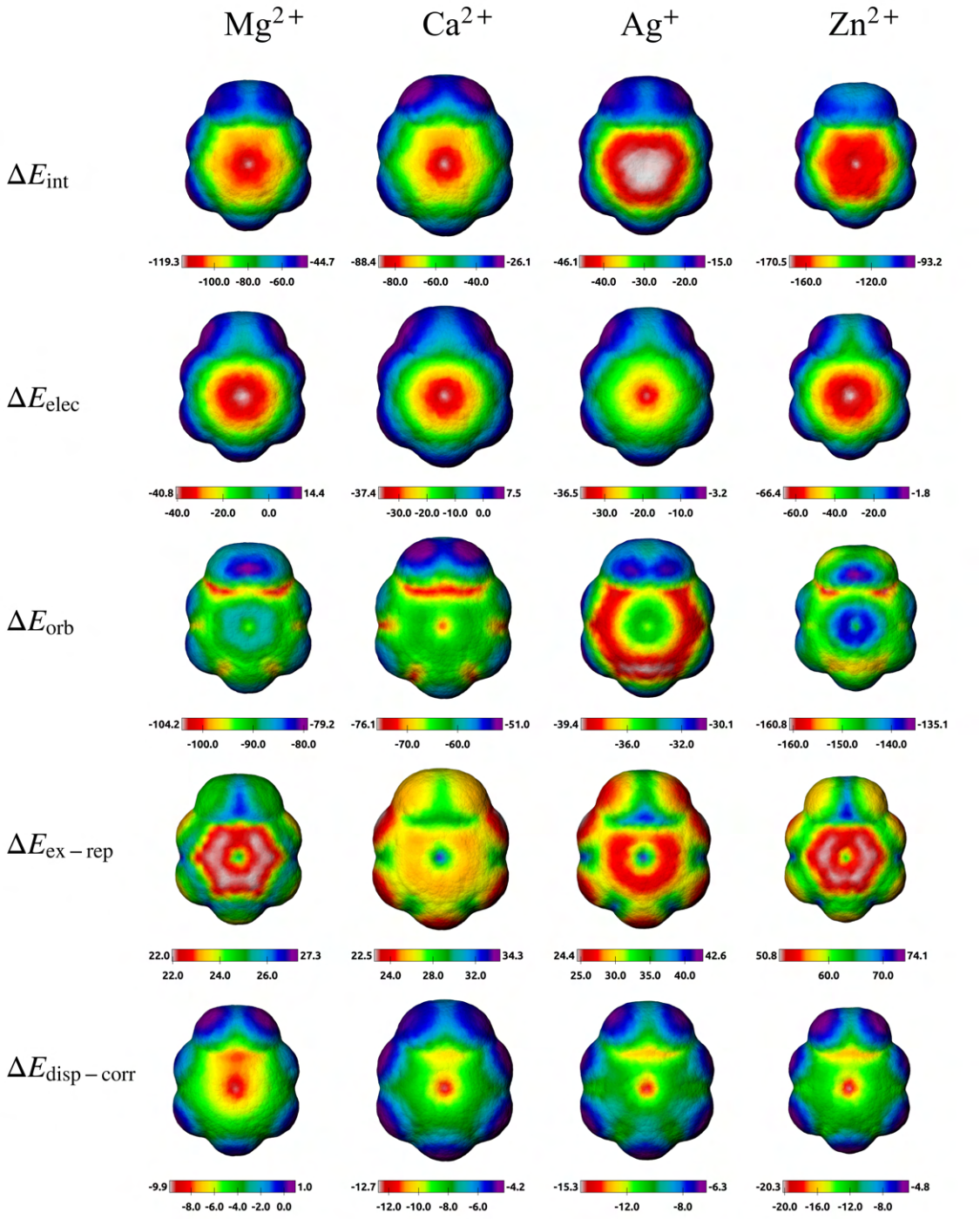

Figure S20. ΔE_{int}, ΔE_{elec}, ΔE_{orb}, $\Delta E_{\text{ex-rep}}$, and $\Delta E_{\text{disp-corr}}$ surfaces of toluene with $Mg^{2+}, Ca^{2+}, Ag^{+}, Zn^{2+}$ probes.

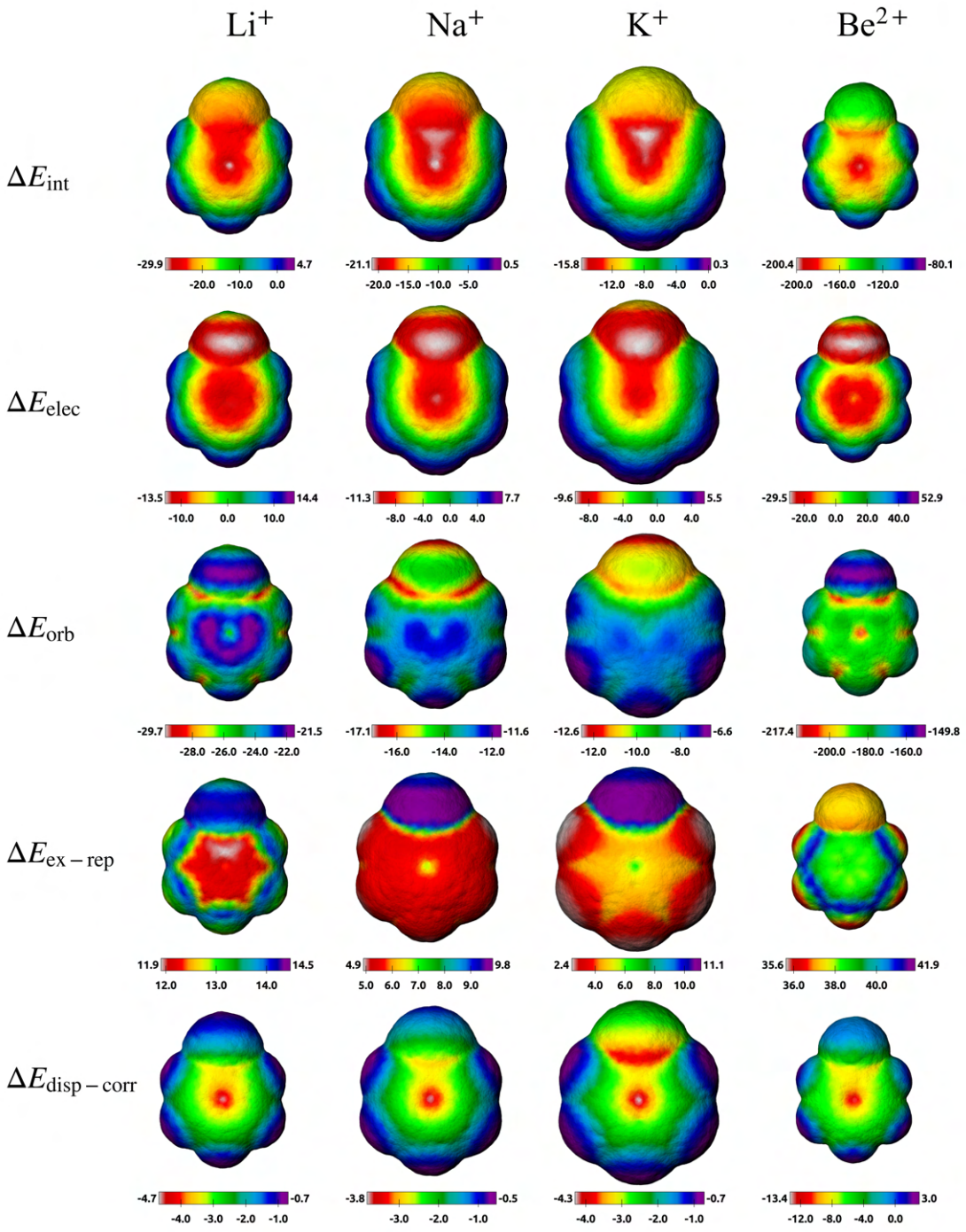

Figure S21. ΔE_{int}, ΔE_{elec}, ΔE_{orb}, $\Delta E_{\text{ex-rep}}$, and $\Delta E_{\text{disp-corr}}$ surfaces of chlorobenzene with Li^+, Na^+, K^+, Be^{2+} probes.

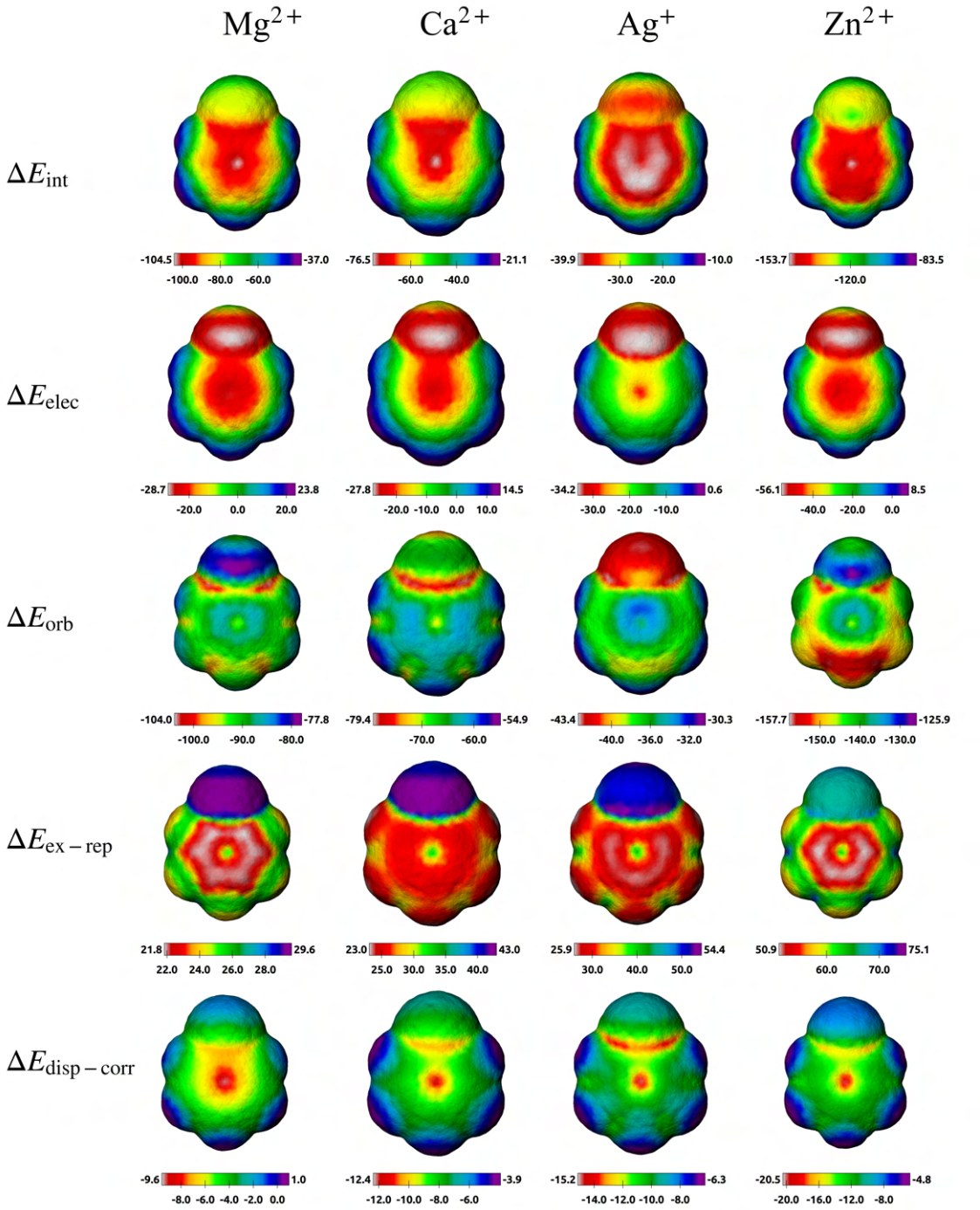

Figure S22. ΔE_{int}, ΔE_{elec}, ΔE_{orb}, $\Delta E_{\text{ex-rep}}$, and $\Delta E_{\text{disp-corr}}$ surfaces of chlorobenzene with $Mg^{2+}, Ca^{2+}, Ag^{+}, Zn^{2+}$ probes.

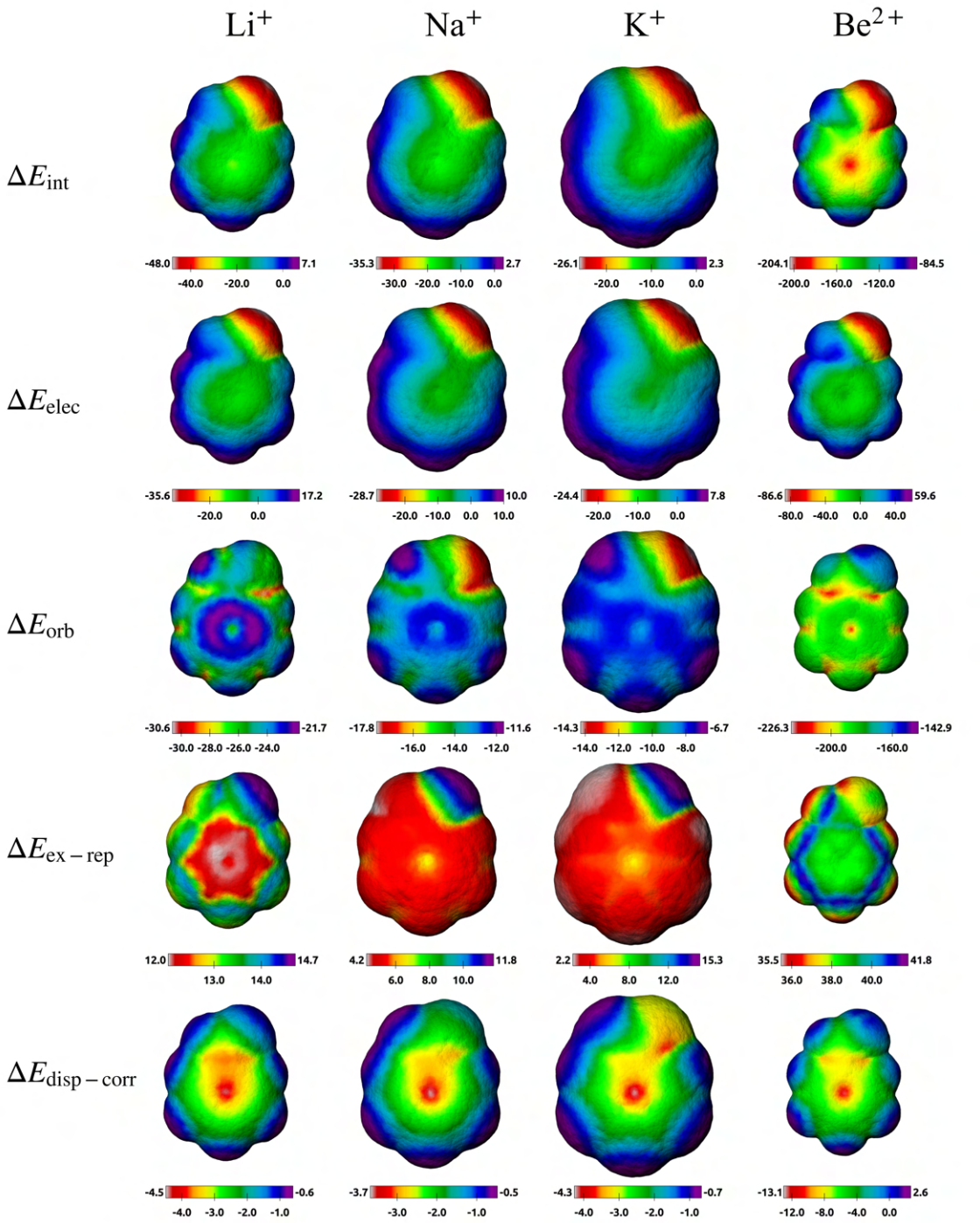

Figure S23. ΔE_{int}, ΔE_{elec}, ΔE_{orb}, $\Delta E_{\text{ex-rep}}$, and $\Delta E_{\text{disp-corr}}$ surfaces of benzaldehyde with Li^+, Na^+, K^+, Be^{2+} probes.

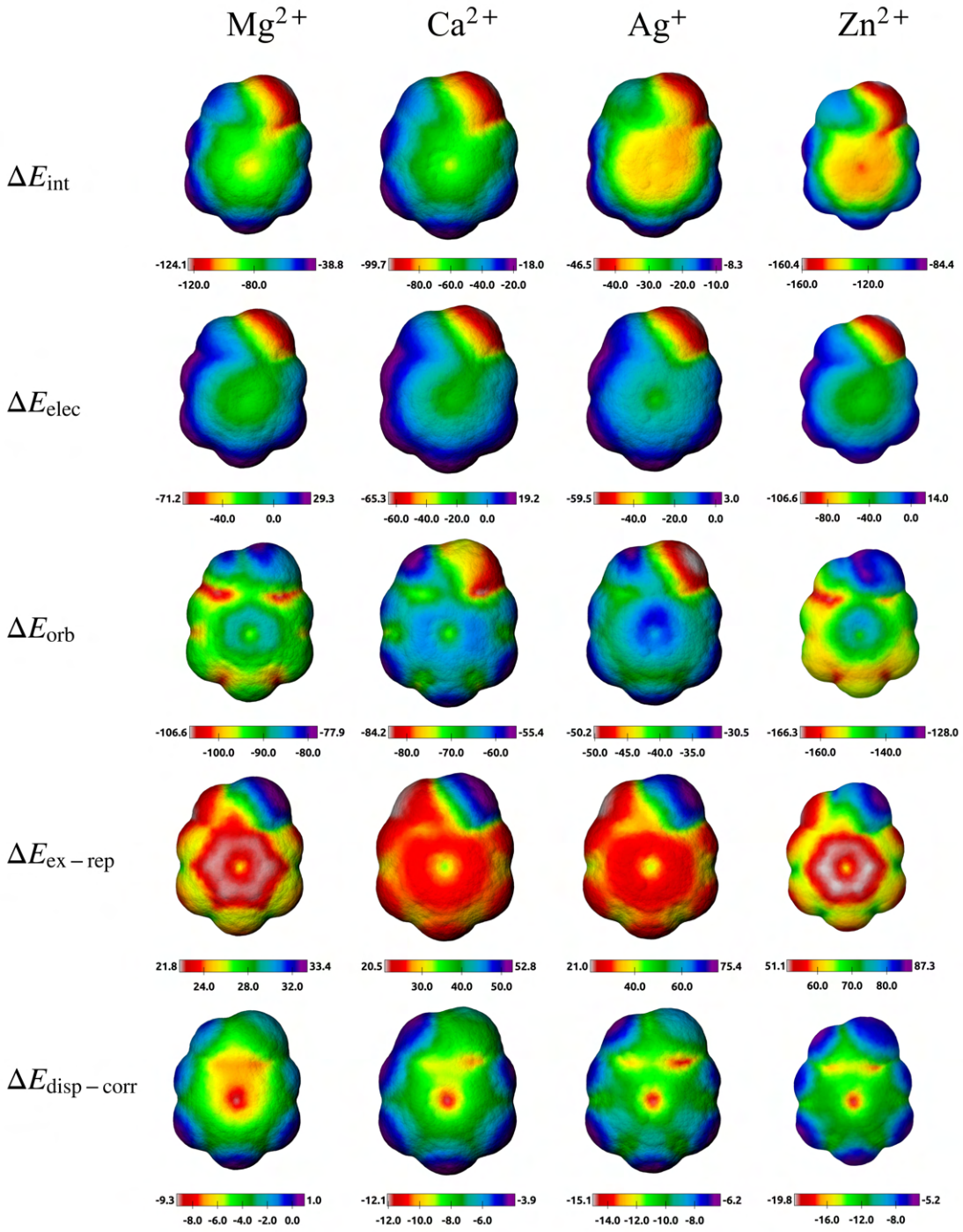

Figure S24. ΔE_{int}, ΔE_{elec}, ΔE_{orb}, $\Delta E_{\text{ex-rep}}$, and $\Delta E_{\text{disp-corr}}$ surfaces of benzaldehyde with $Mg^{2+}, Ca^{2+}, Ag^{+}, Zn^{2+}$ probes.

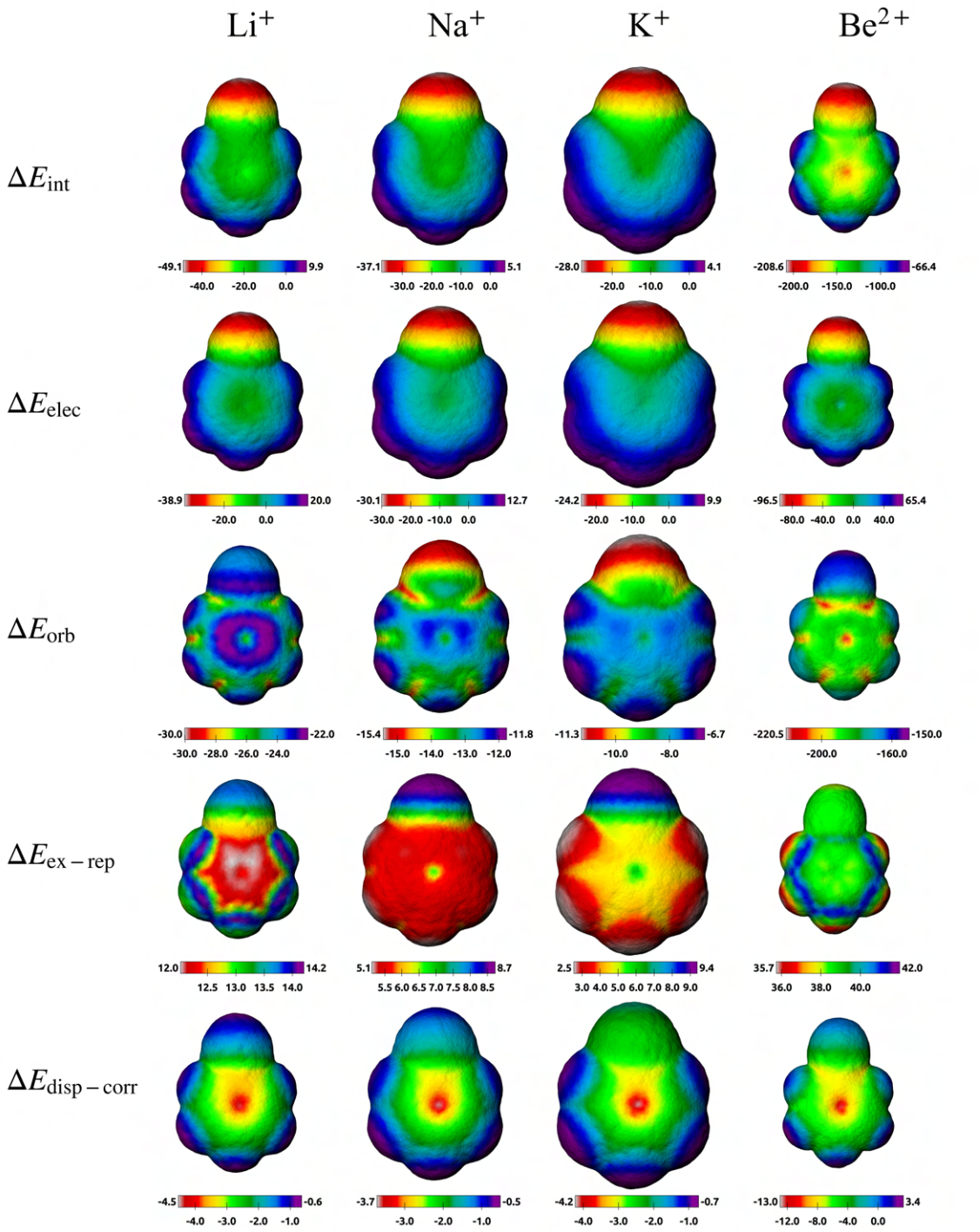

Figure S25. ΔE_{int}, ΔE_{elec}, ΔE_{orb}, $\Delta E_{\text{ex-rep}}$, and $\Delta E_{\text{disp-corr}}$ surfaces of benzonitrile with Li^+, Na^+, K^+, Be^{2+} probes.

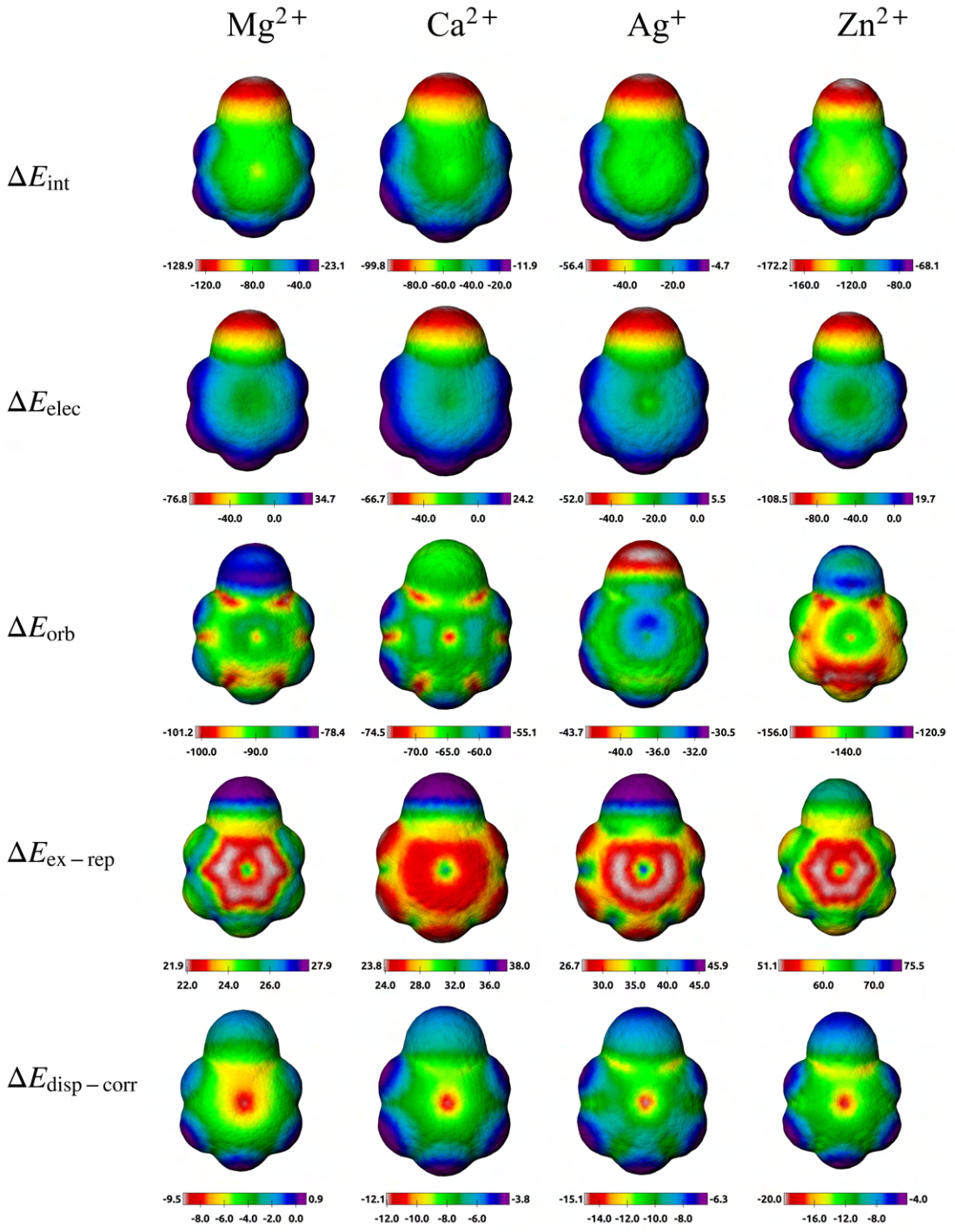

Figure S26. ΔE_{int}, ΔE_{elec}, ΔE_{orb}, $\Delta E_{\text{ex-rep}}$, and $\Delta E_{\text{disp-corr}}$ surfaces of benzonitrile with $Mg^{2+}, Ca^{2+}, Ag^{+}, Zn^{2+}$ probes.

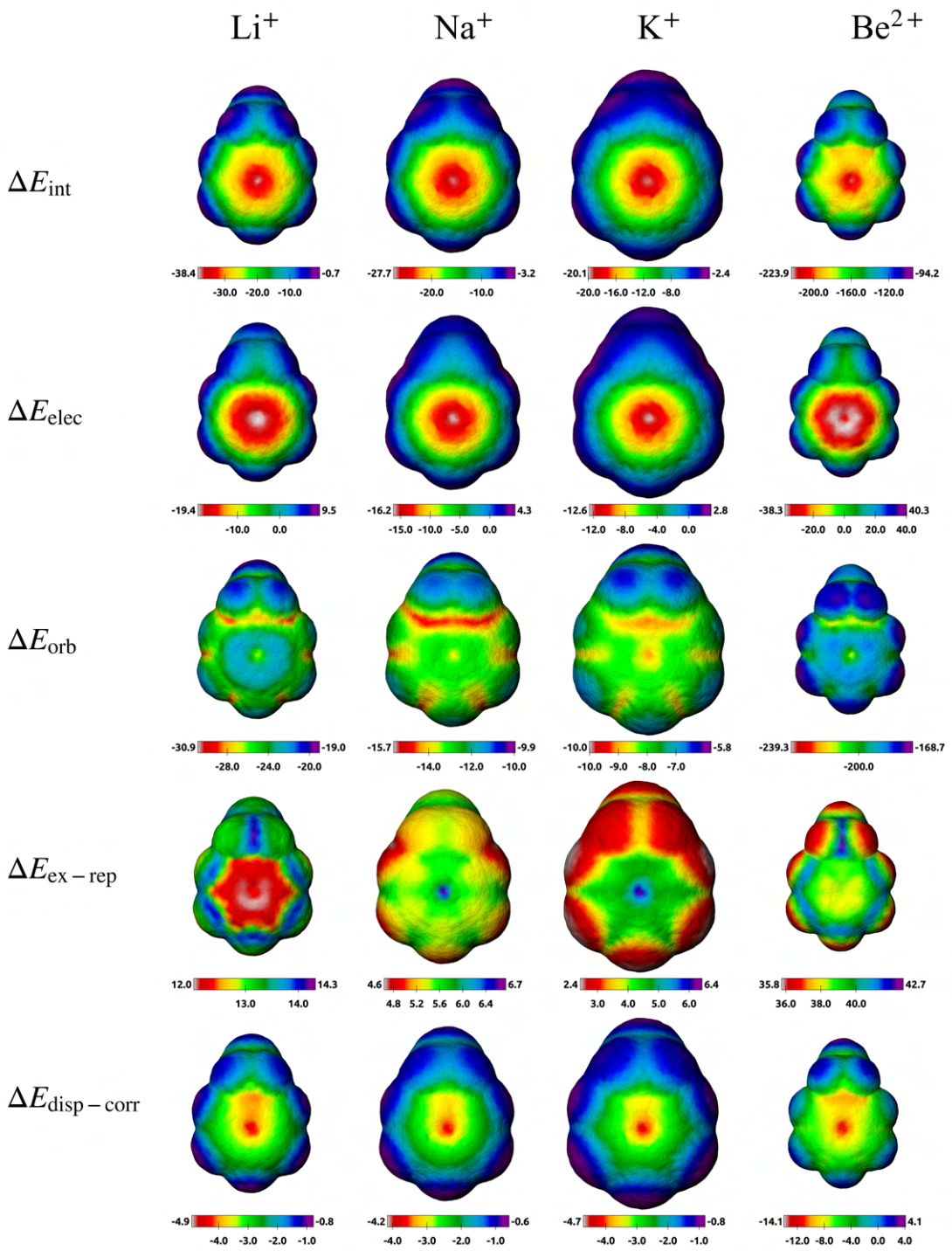

Figure S27. ΔE_{int}, ΔE_{elec}, ΔE_{orb}, $\Delta E_{\text{ex-rep}}$, and $\Delta E_{\text{disp-corr}}$ surfaces of ethylbenzene with Li^+, Na^+, K^+, Be^{2+} probes.

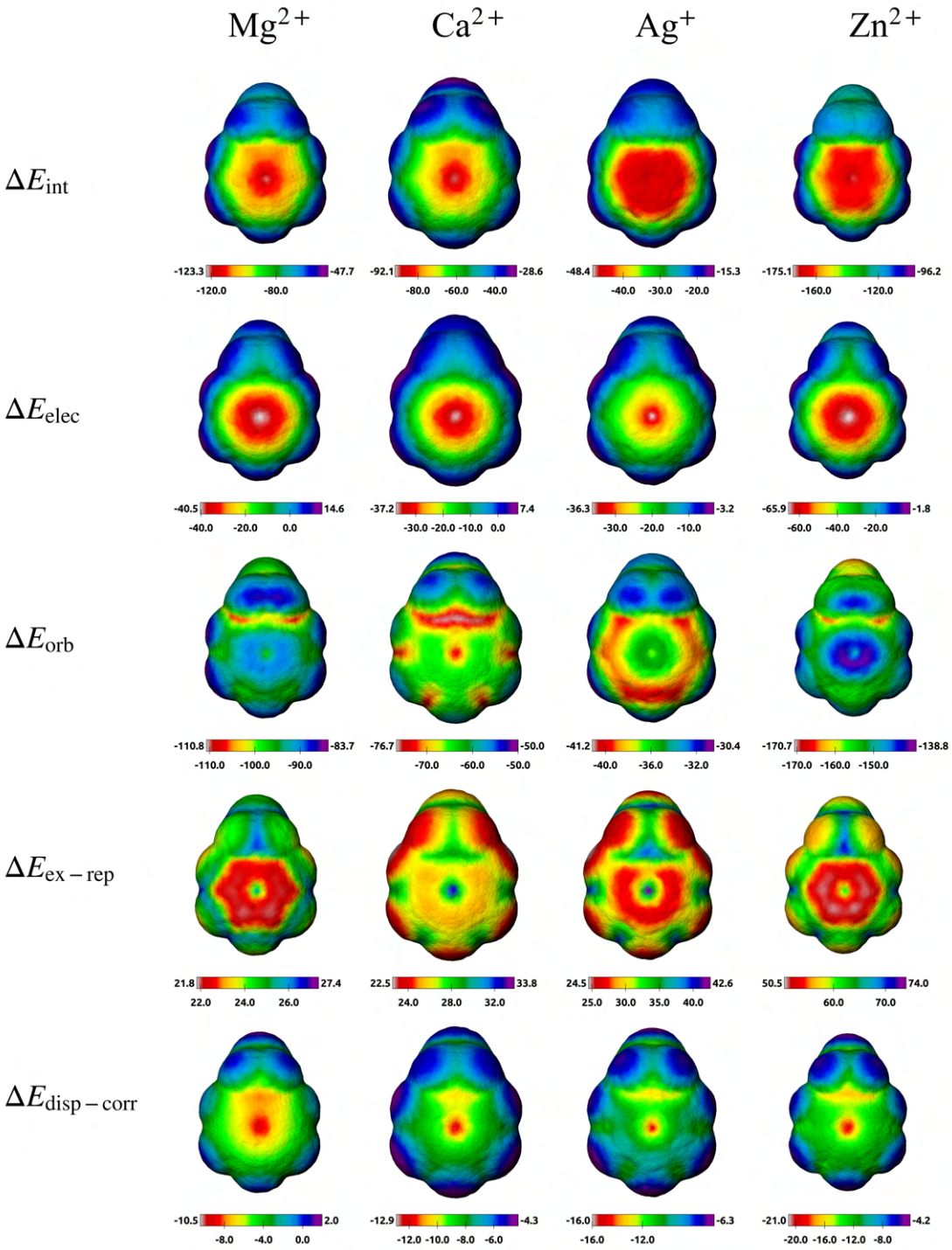

Figure S28. ΔE_{int}, ΔE_{elec}, ΔE_{orb}, $\Delta E_{\text{ex-rep}}$, and $\Delta E_{\text{disp-corr}}$ surfaces of ethylbenzene with Mg^{2+}, Ca^{2+}, Ag^{+}, Zn^{2+} probes.

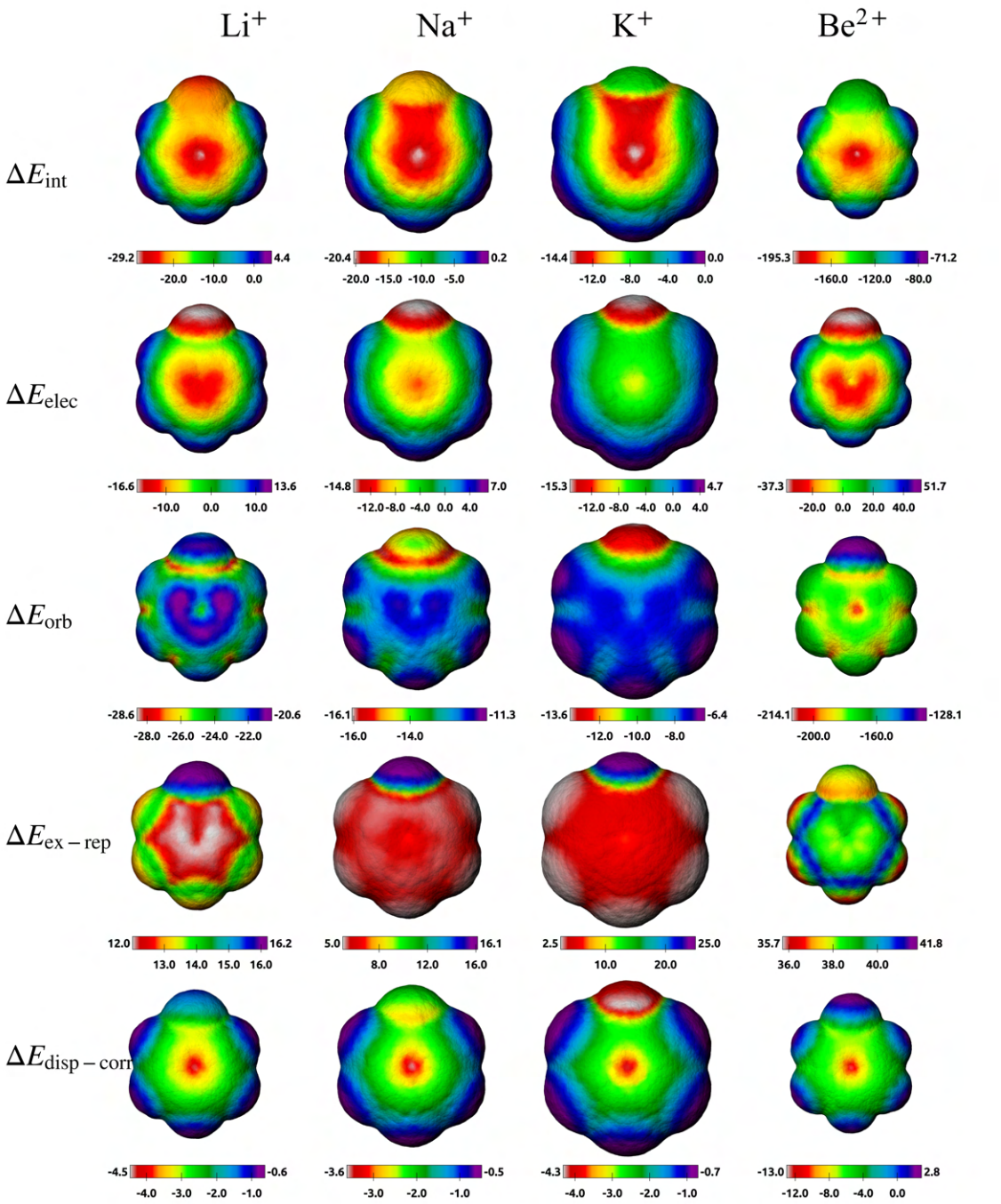

Figure S29. ΔE_{int}, ΔE_{elec}, ΔE_{orb}, $\Delta E_{\text{ex-rep}}$, and $\Delta E_{\text{disp-corr}}$ surfaces of fluorobenzene with Li^+, Na^+, K^+, Be^{2+} probes.

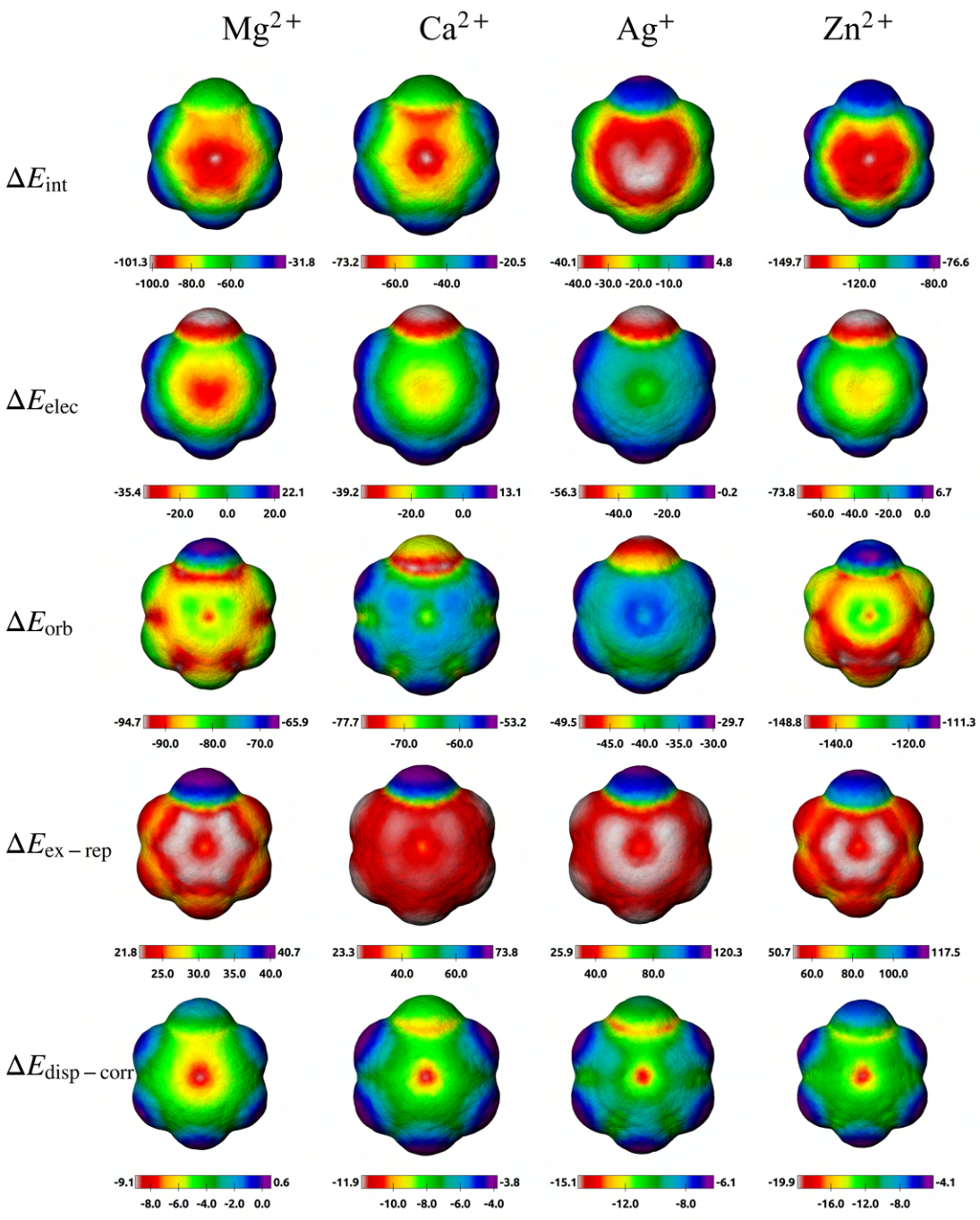

Figure S30. ΔE_{int}, ΔE_{elec}, ΔE_{orb}, $\Delta E_{\text{ex-rep}}$, and $\Delta E_{\text{disp-corr}}$ surfaces of fluorobenzene with $Mg^{2+}, Ca^{2+}, Ag^{+}, Zn^{2+}$ probes.

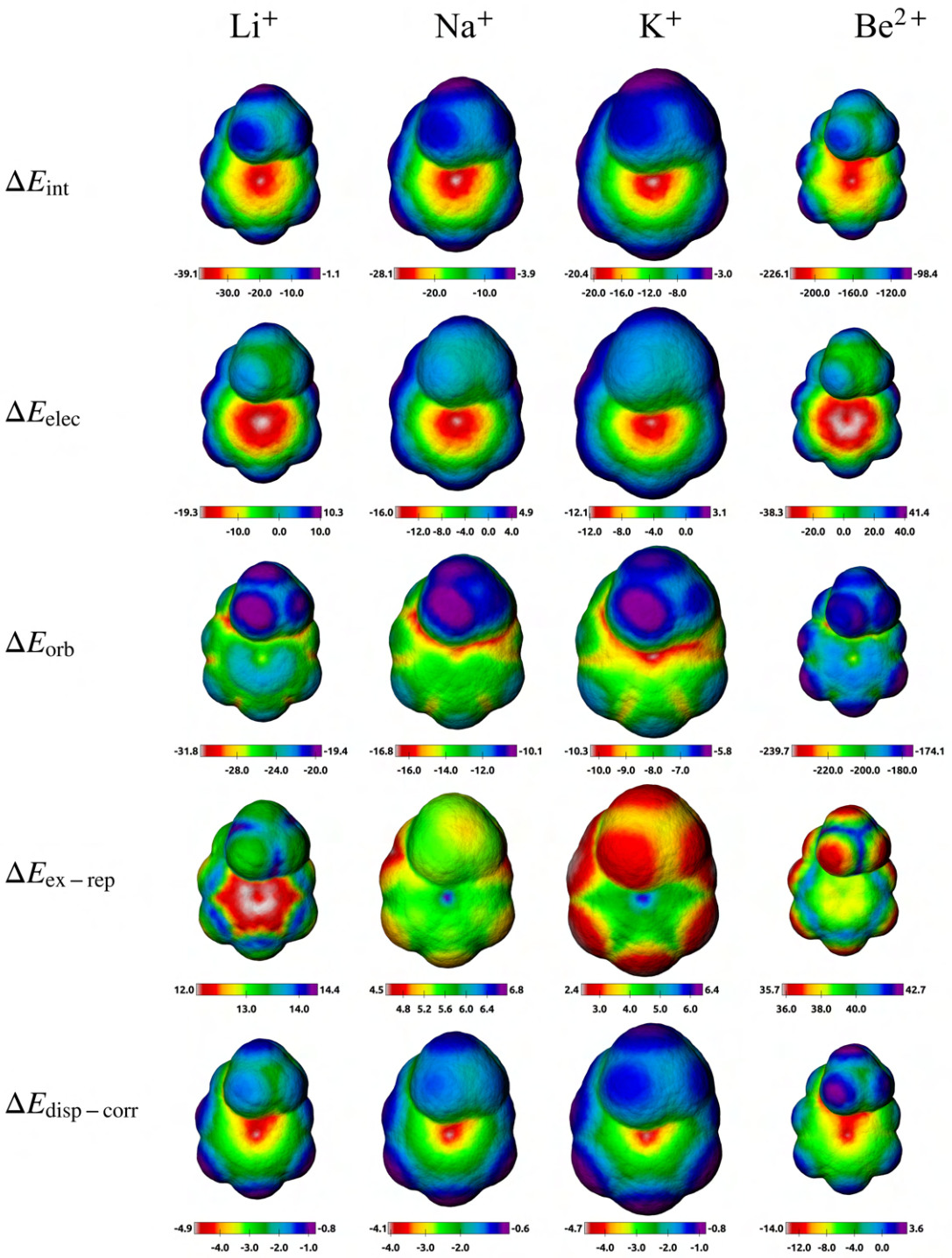

Figure S31. ΔE_{int}, ΔE_{elec}, ΔE_{orb}, $\Delta E_{\text{ex-rep}}$, and $\Delta E_{\text{disp-corr}}$ surfaces of cumene with Li^+, Na^+, K^+, Be^{2+} probes.

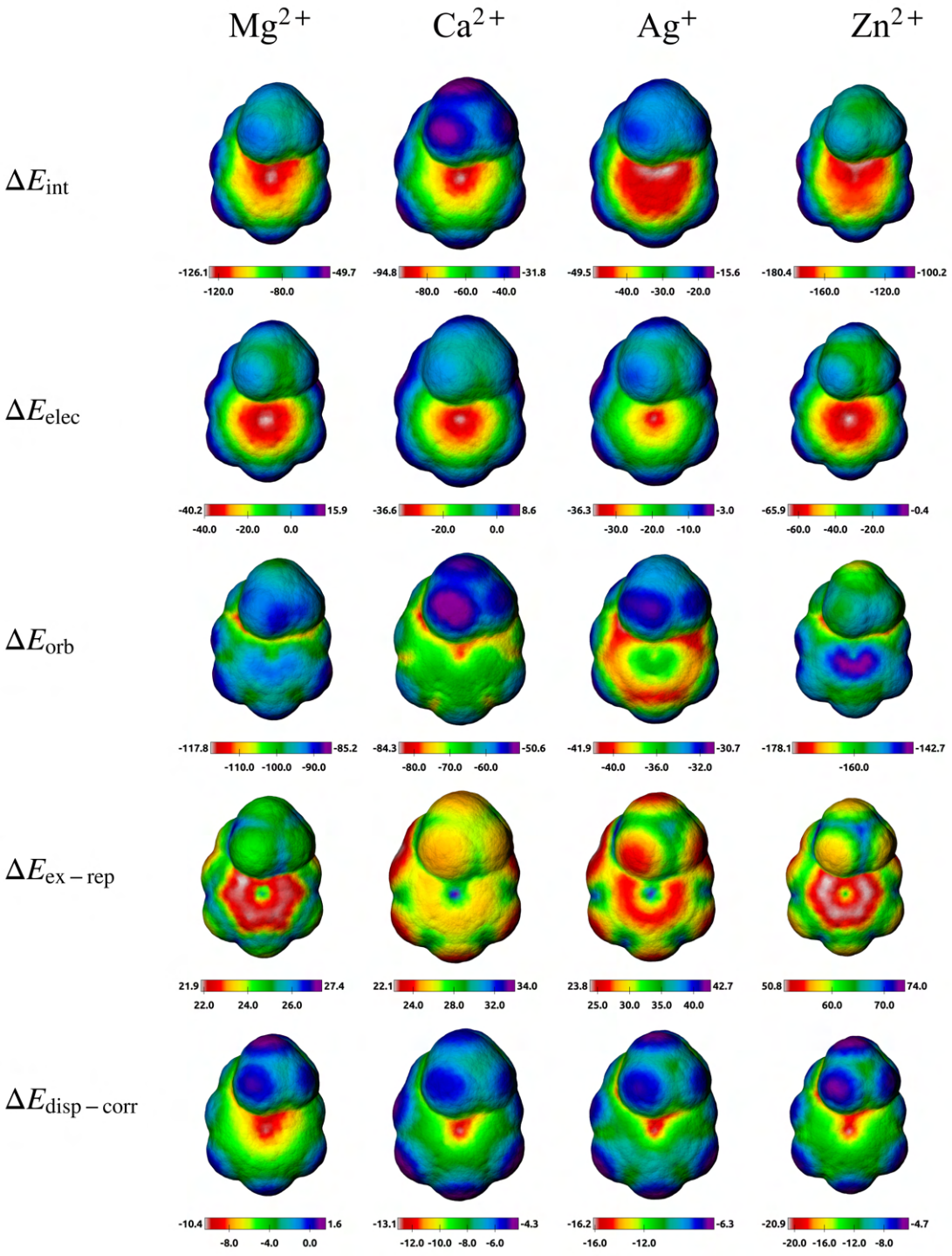

Figure S32. ΔE_{int}, ΔE_{elec}, ΔE_{orb}, $\Delta E_{\text{ex-rep}}$, and $\Delta E_{\text{disp-corr}}$ surfaces of cumene with Mg^{2+}, Ca^{2+}, Ag^{+}, Zn^{2+} probes.

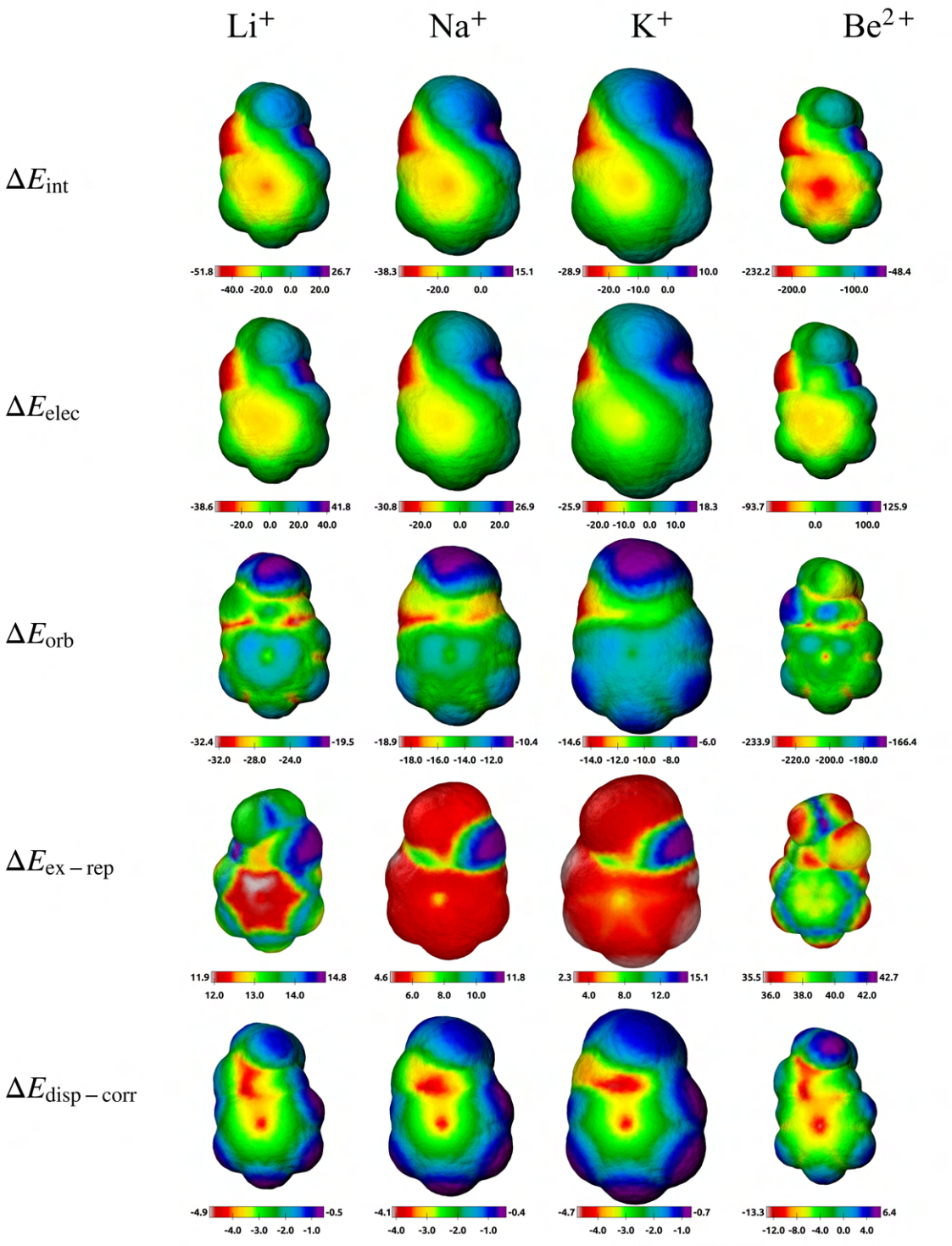

Figure S33. ΔE_{int}, ΔE_{elec}, ΔE_{orb}, $\Delta E_{\text{ex-rep}}$, and $\Delta E_{\text{disp-corr}}$ surfaces of acetanilide with Li^+, Na^+, K^+, Be^{2+} probes.

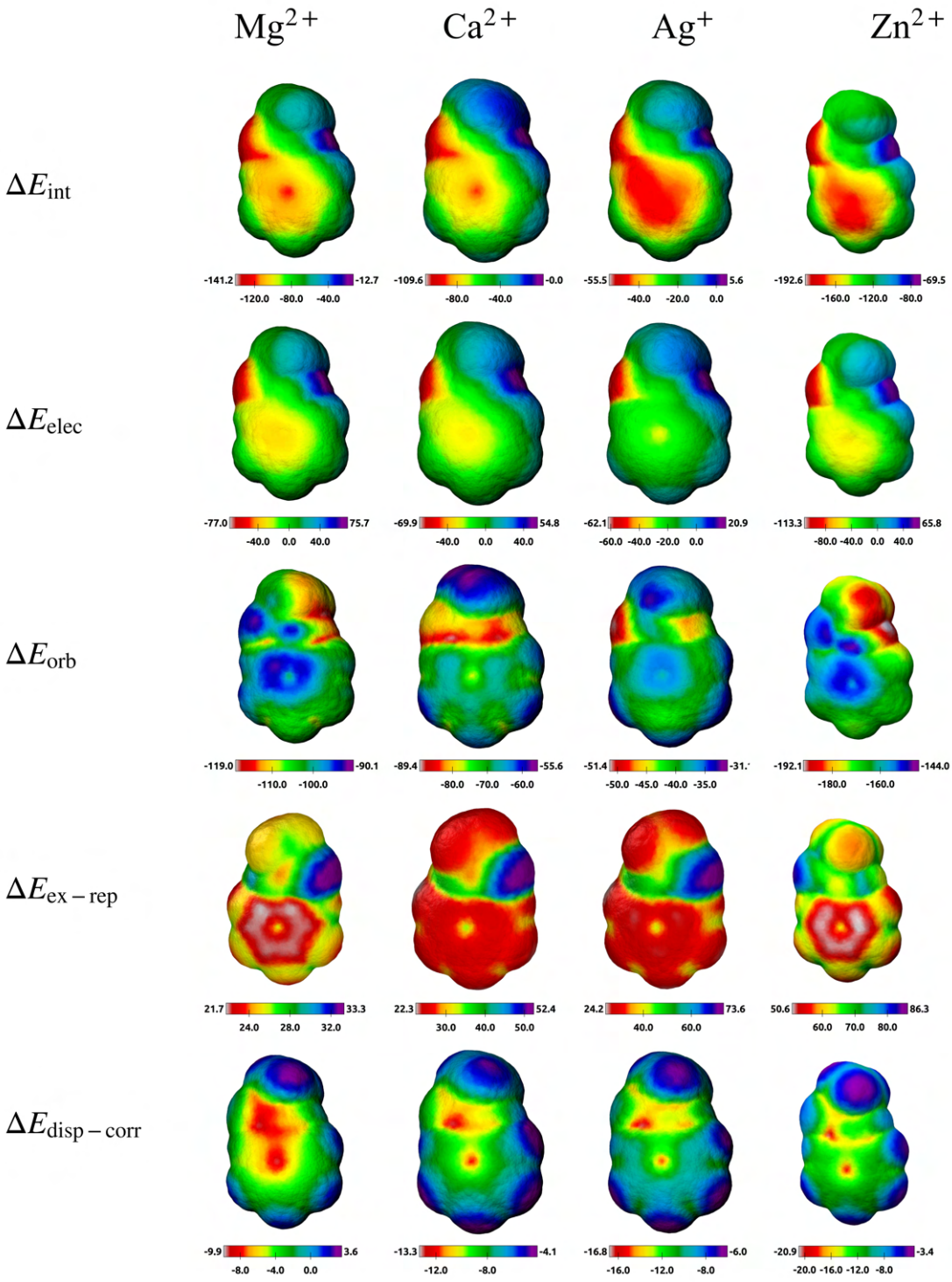

Figure S34. ΔE_{int}, ΔE_{elec}, ΔE_{orb}, $\Delta E_{\text{ex-rep}}$, and $\Delta E_{\text{disp-corr}}$ surfaces of acetanilide with Mg^{2+}, Ca^{2+}, Ag^{+}, Zn^{2+} probes.

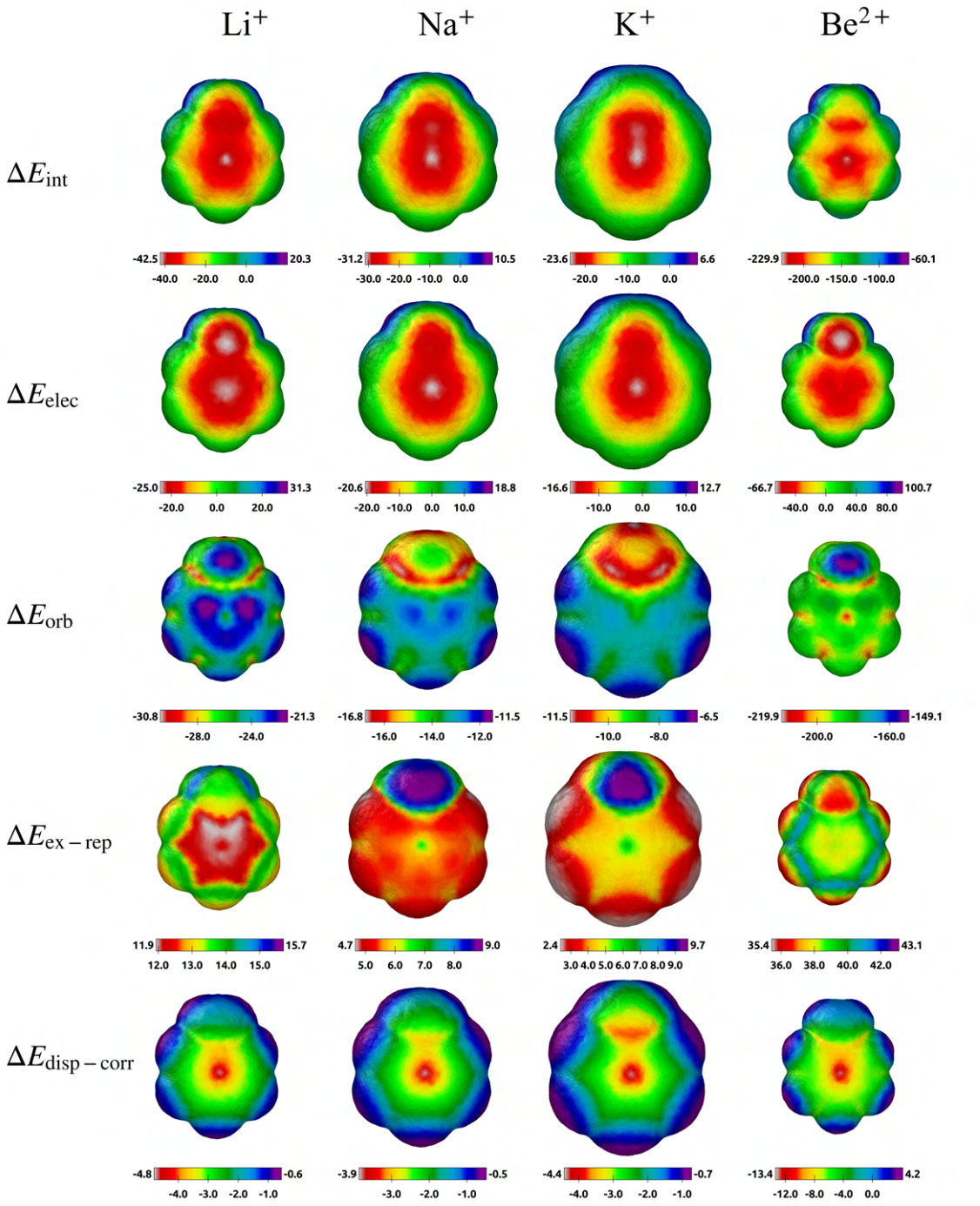

Figure S35. ΔE_{int}, ΔE_{elec}, ΔE_{orb}, $\Delta E_{\text{ex-rep}}$, and $\Delta E_{\text{disp-corr}}$ surfaces of aniline with Li^+, Na^+, K^+, Be^{2+} probes.

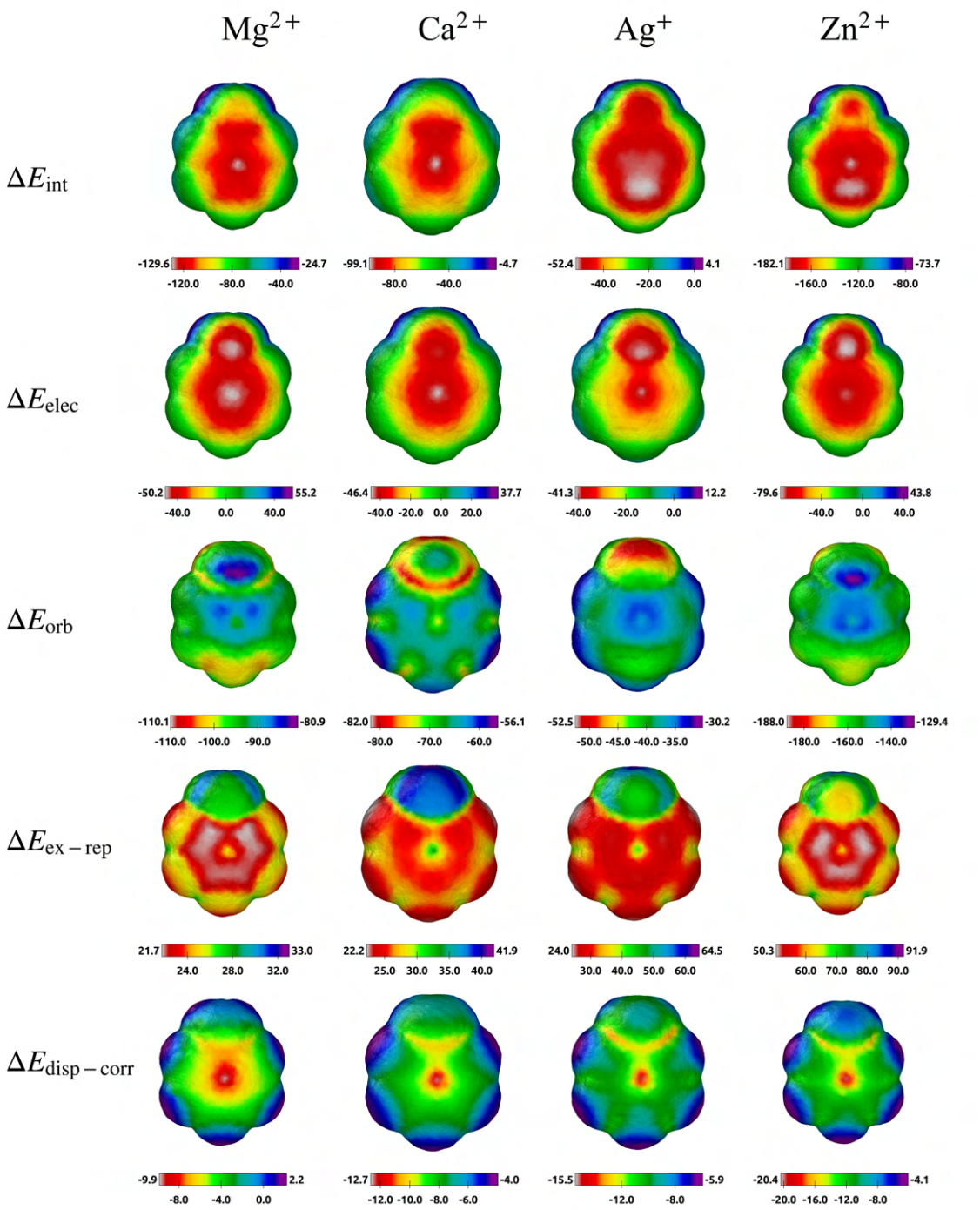

Figure S36. ΔE_{int}, ΔE_{elec}, ΔE_{orb}, $\Delta E_{\text{ex}-\text{rep}}$, and $\Delta E_{\text{disp}-\text{corr}}$ surfaces of aniline with $Mg^{2+}, Ca^{2+}, Ag^{+}, Zn^{2+}$ probes.

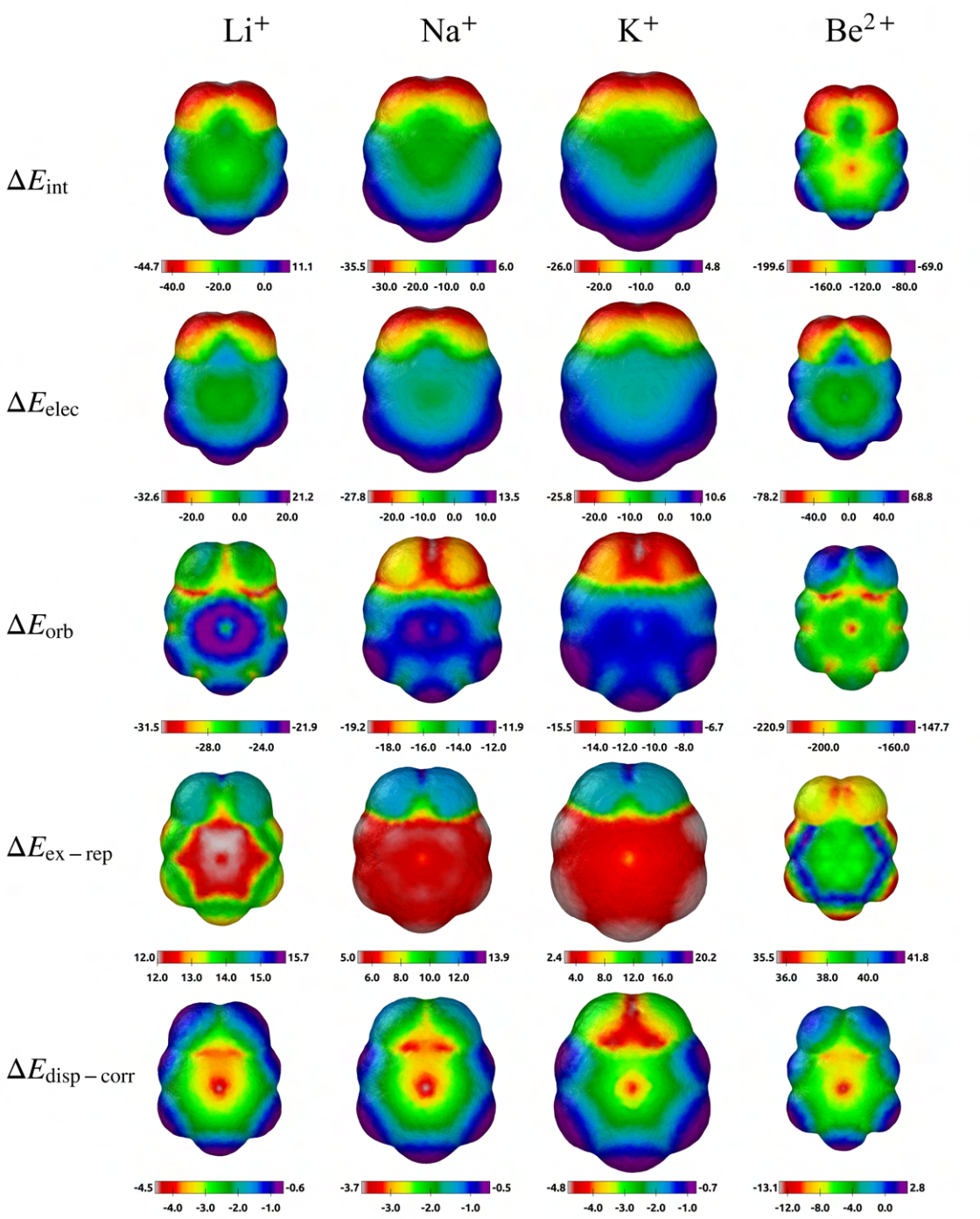

Figure S37. ΔE_{int}, ΔE_{elec}, ΔE_{orb}, $\Delta E_{\text{ex-rep}}$, and $\Delta E_{\text{disp-corr}}$ surfaces of nitrobenzene with Li^+, Na^+, K^+, Be^{2+} probes.

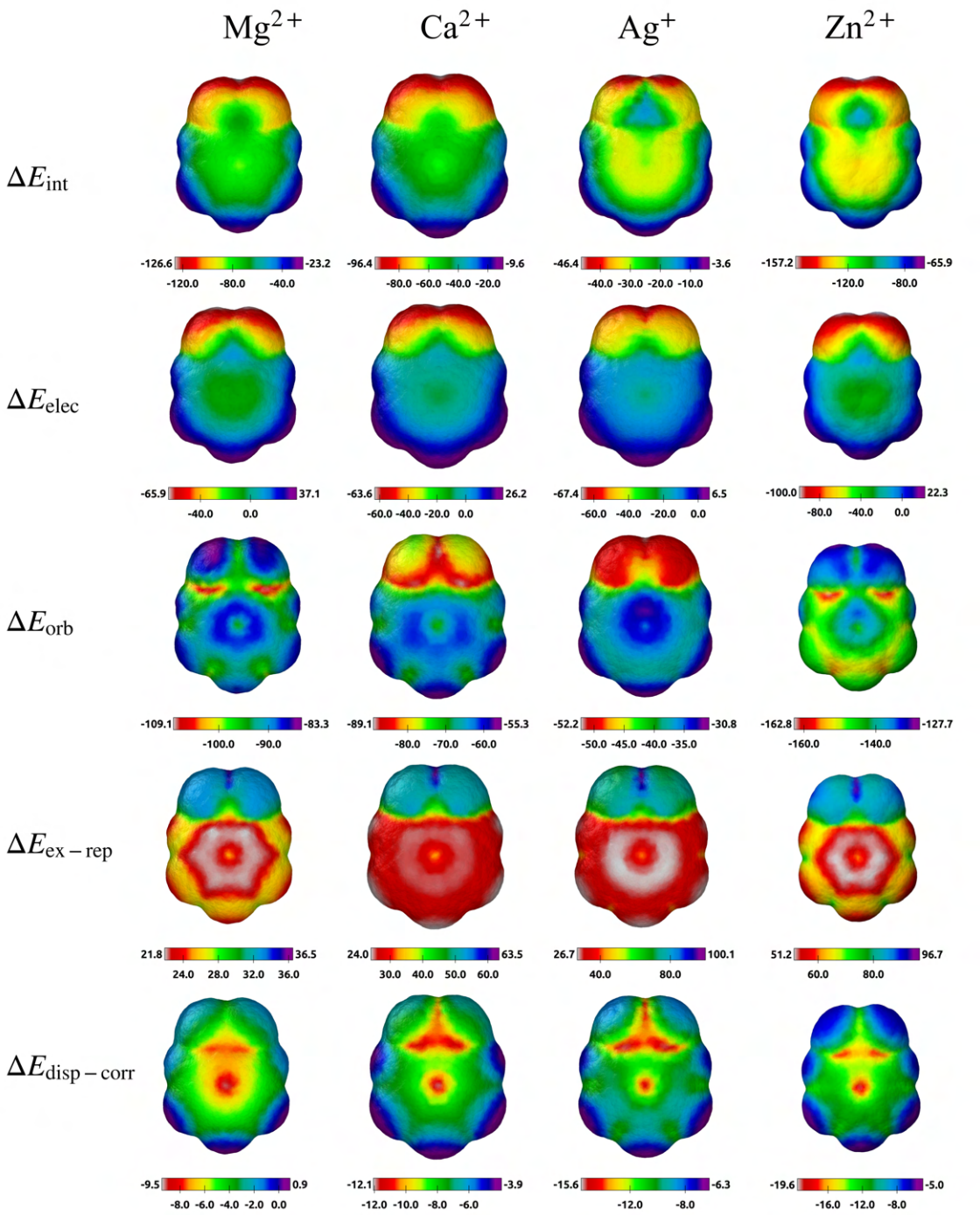

Figure S38. ΔE_{int}, ΔE_{elec}, ΔE_{orb}, $\Delta E_{\text{ex-rep}}$, and $\Delta E_{\text{disp-corr}}$ surfaces of nitrobenzene with $Mg^{2+}, Ca^{2+}, Ag^{+}, Zn^{2+}$ probes.

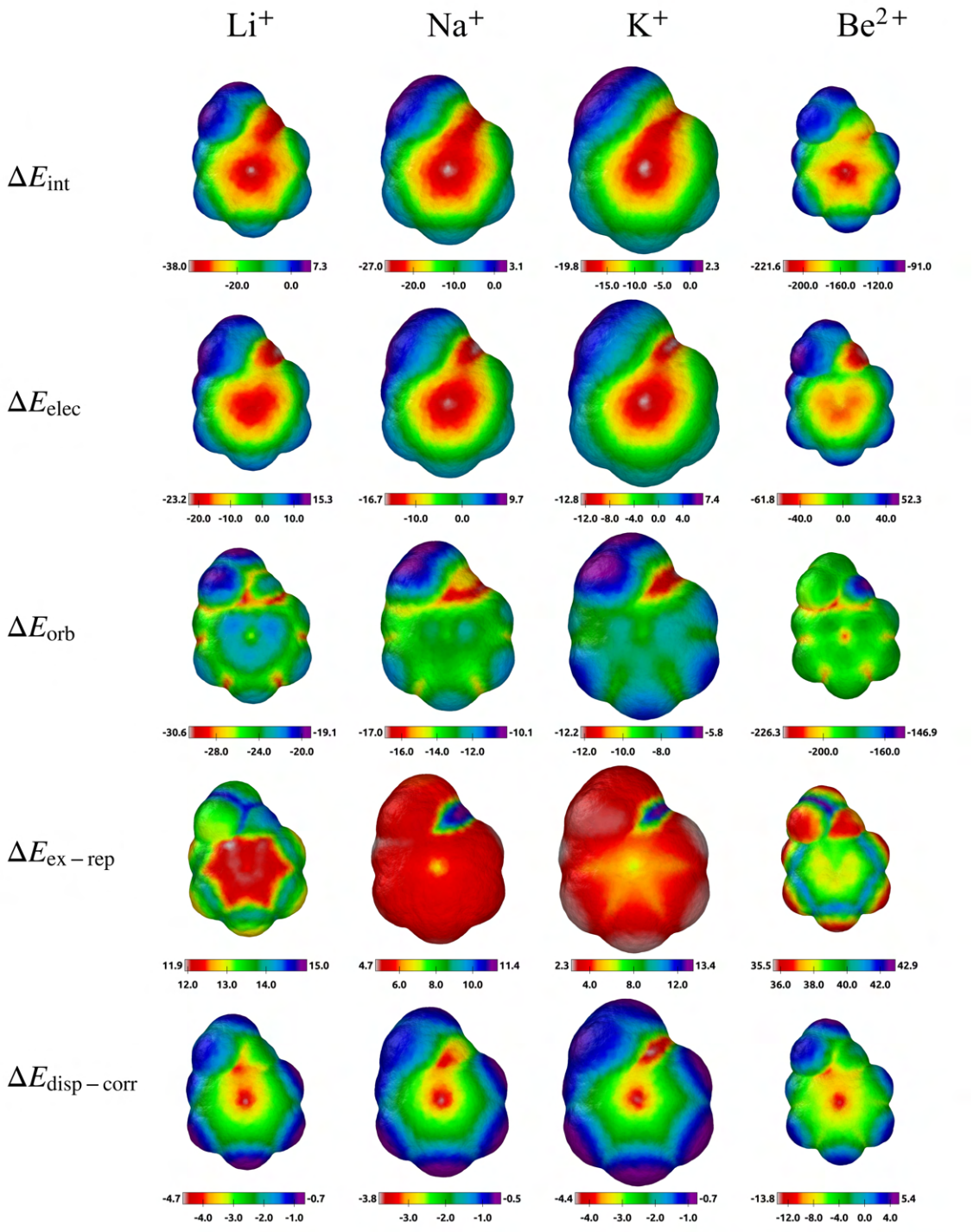

Figure S39. ΔE_{int}, ΔE_{elec}, ΔE_{orb}, $\Delta E_{\text{ex-rep}}$, and $\Delta E_{\text{disp-corr}}$ surfaces of anisole with Li^+, Na^+, K^+, Be^{2+} probes.

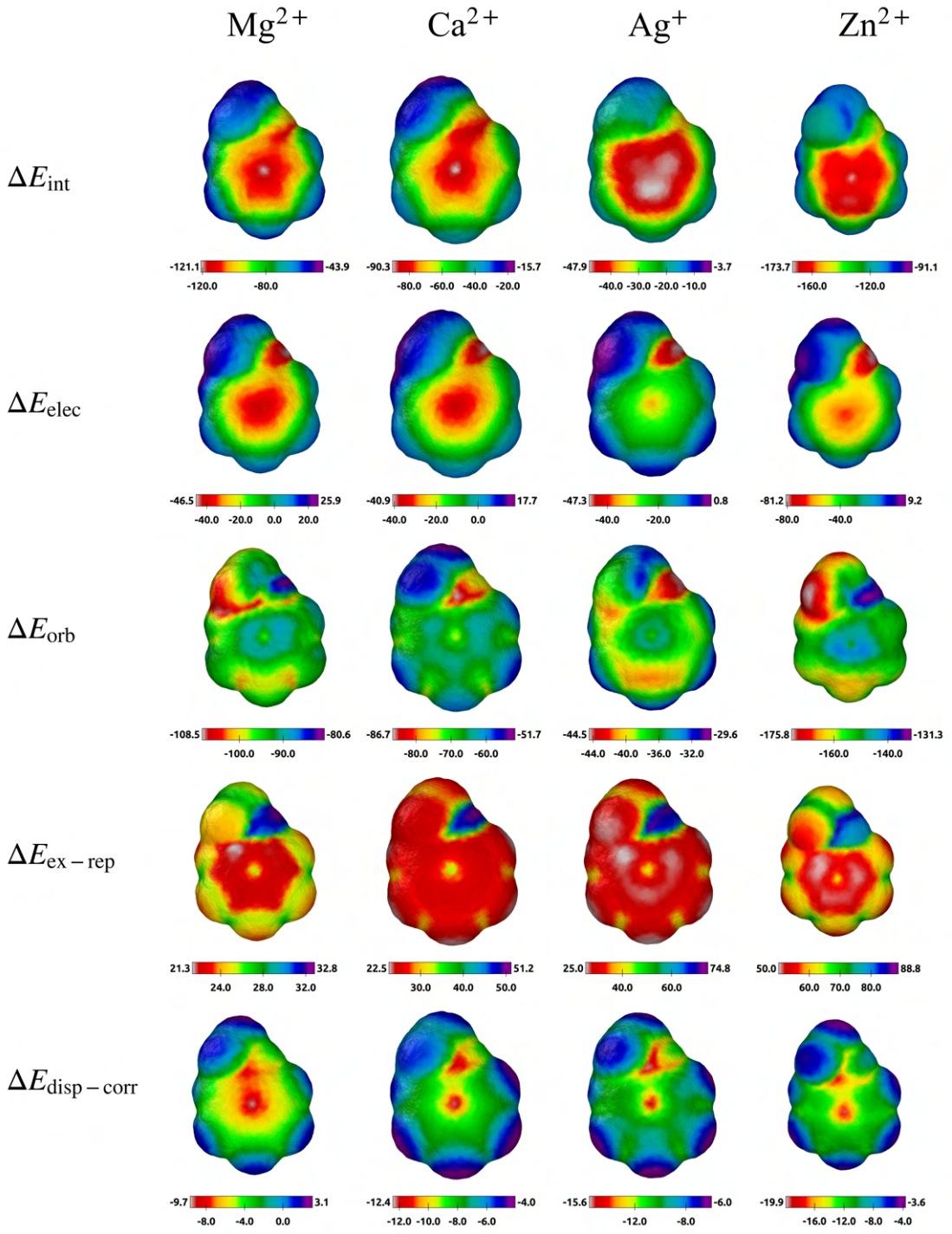

Figure S40. ΔE_{int}, ΔE_{elec}, ΔE_{orb}, $\Delta E_{\text{ex-rep}}$, and $\Delta E_{\text{disp-corr}}$ surfaces of anisole with Mg^{2+}, Ca^{2+}, Ag^{+}, Zn^{2+} probes.

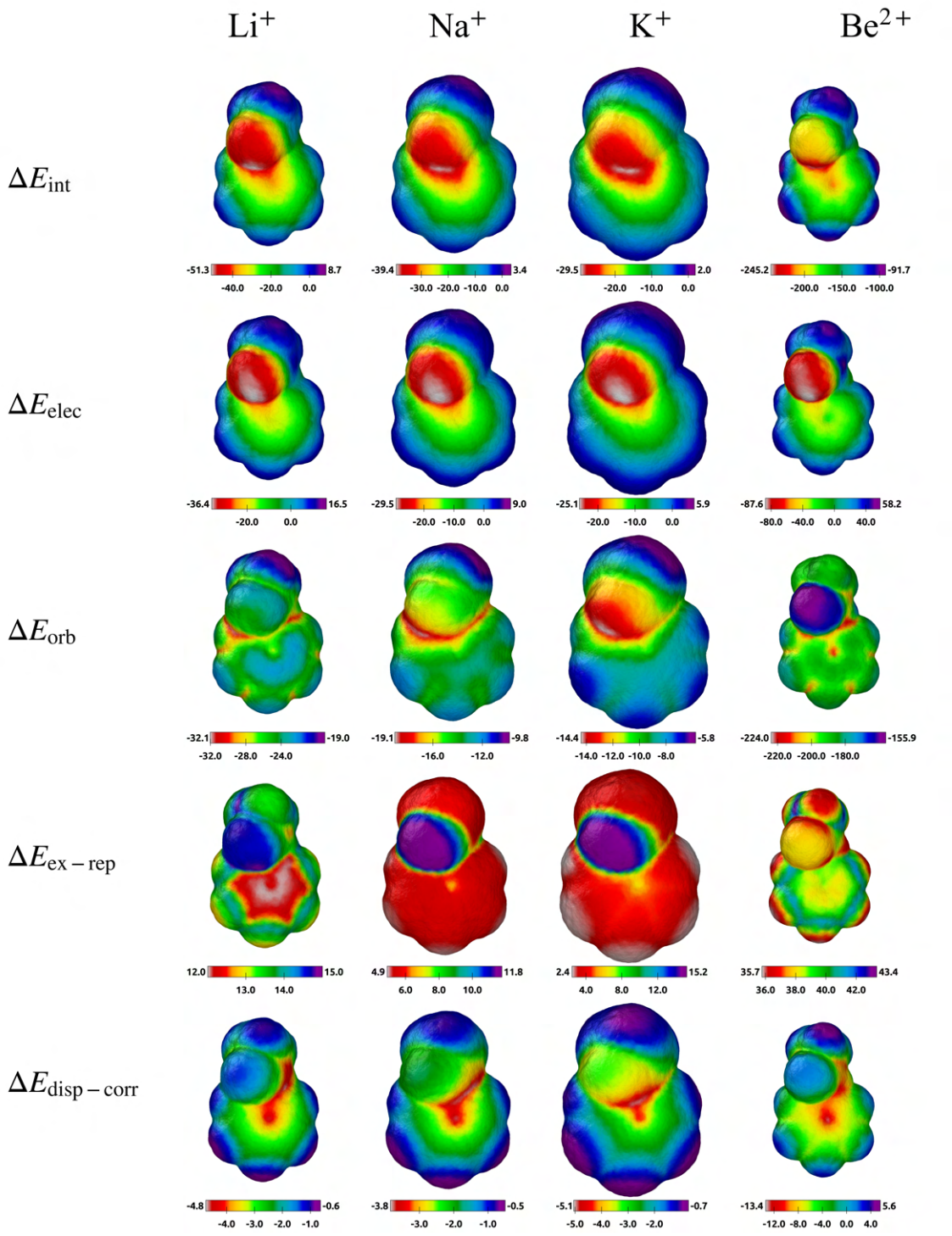

Figure S41. ΔE_{int}, ΔE_{elec}, ΔE_{orb}, $\Delta E_{\text{ex-rep}}$, and $\Delta E_{\text{disp-corr}}$ surfaces of phenyl–acetate with Li^+, Na^+, K^+, Be^{2+} probes.

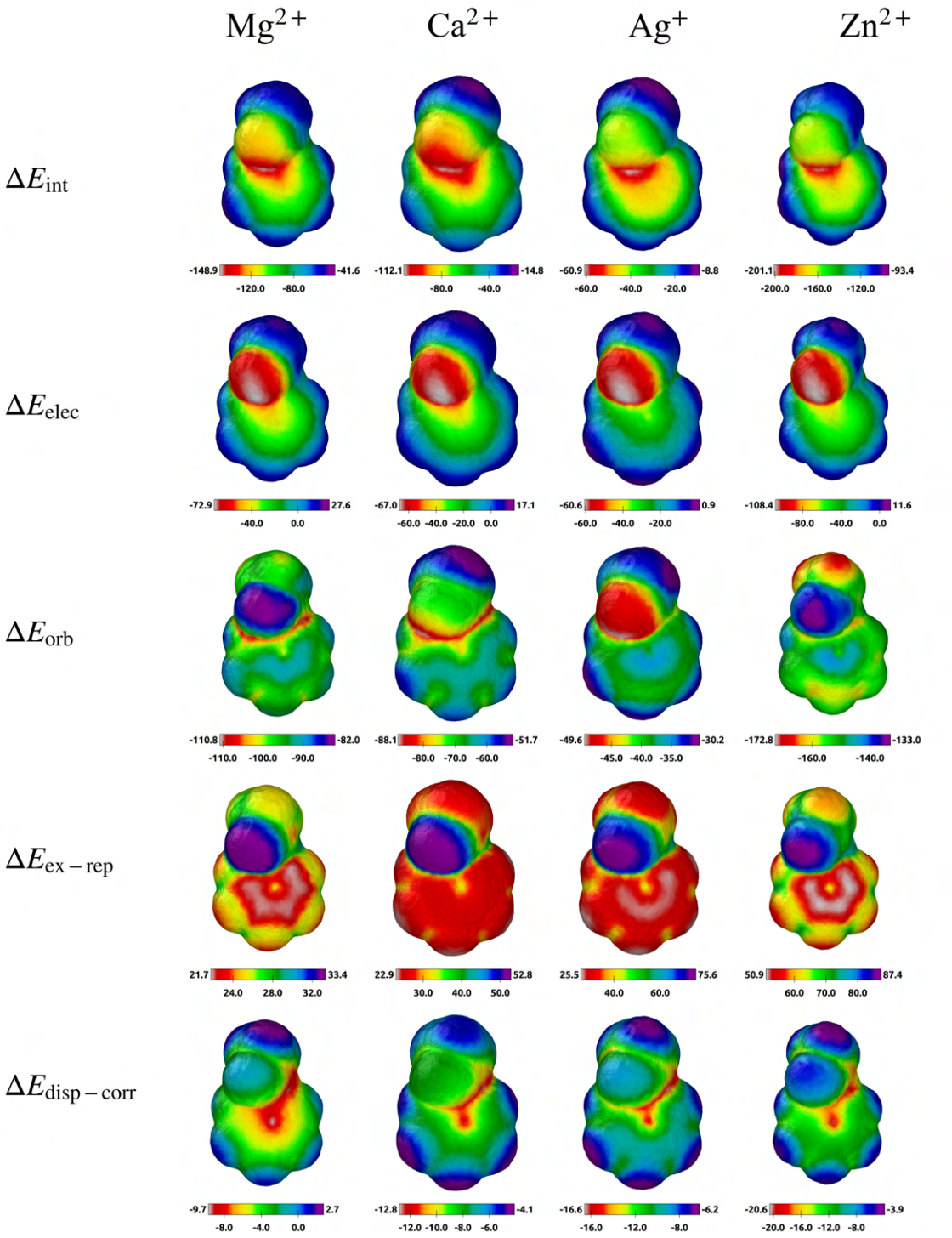

Figure S42. ΔE_{int}, ΔE_{elec}, ΔE_{orb}, $\Delta E_{\text{ex-rep}}$, and $\Delta E_{\text{disp-corr}}$ surfaces of phenyl−acetate with Mg^{2+}, Ca^{2+}, Ag^{+}, Zn^{2+} probes.

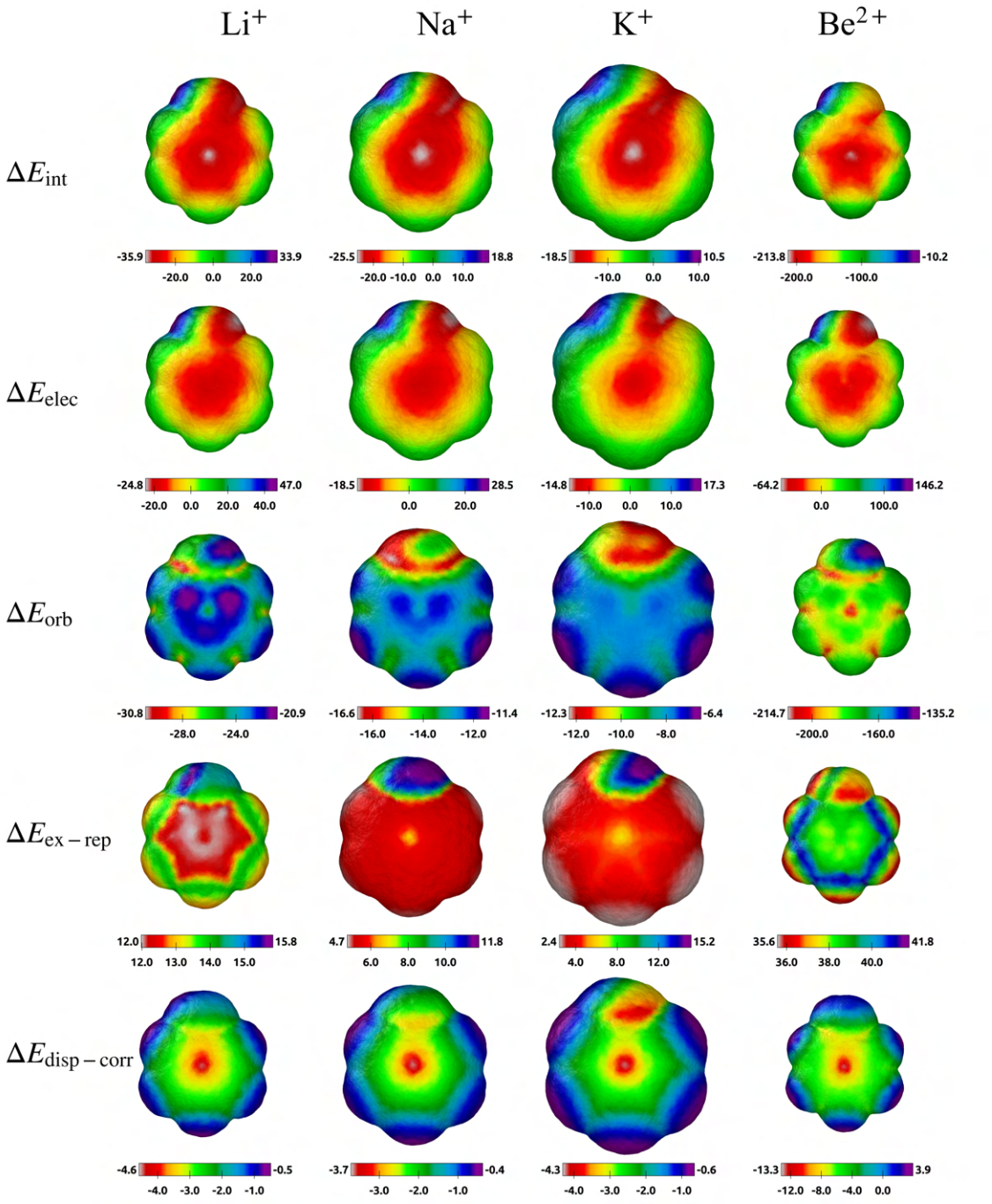

Figure S43. ΔE_{int}, ΔE_{elec}, ΔE_{orb}, $\Delta E_{\text{ex-rep}}$, and $\Delta E_{\text{disp-corr}}$ surfaces of phenol with Li^+, Na^+, K^+, Be^{2+} probes.

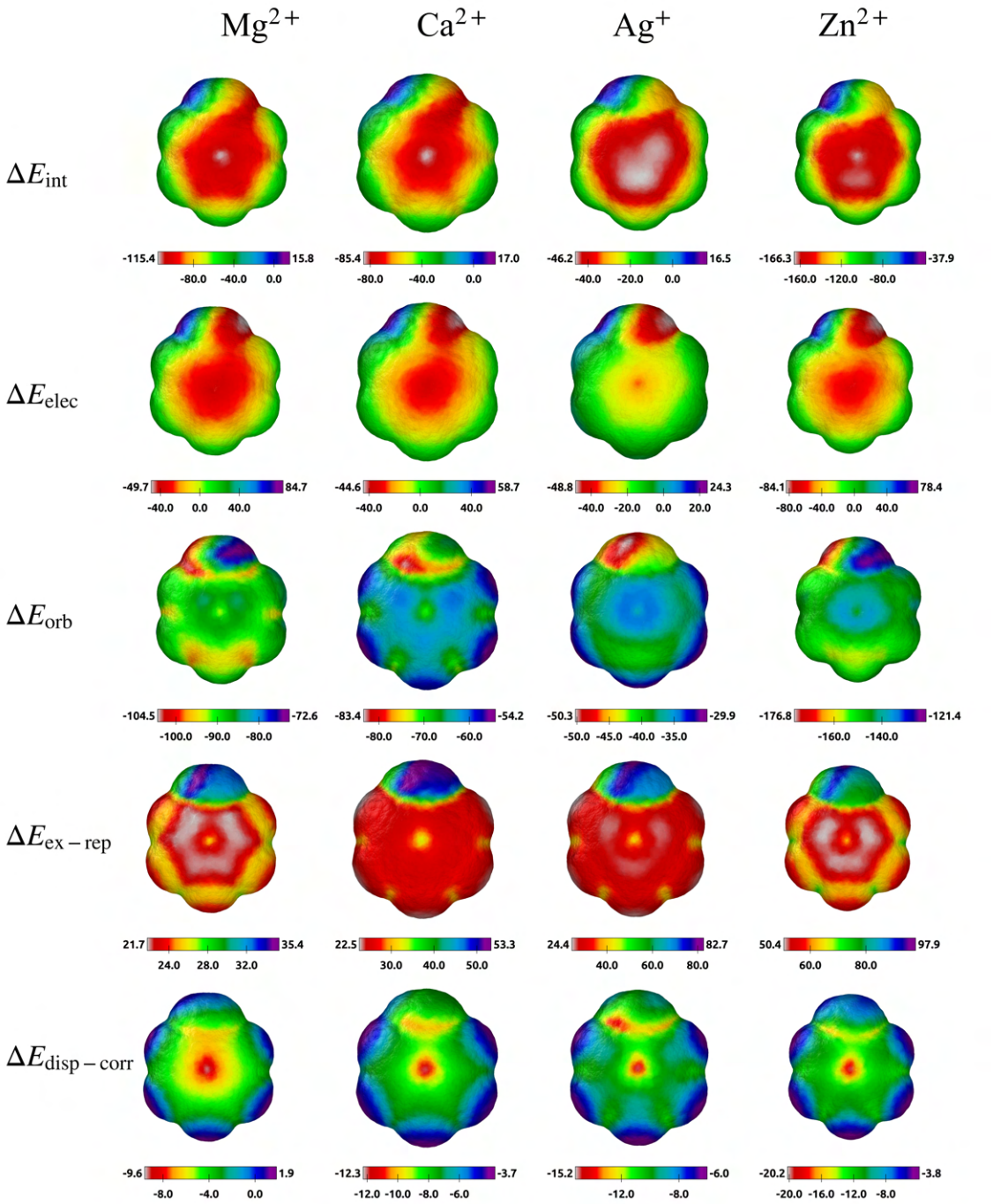

Figure S44. ΔE_{int}, ΔE_{elec}, ΔE_{orb}, $\Delta E_{\text{ex-rep}}$, and $\Delta E_{\text{disp-corr}}$ surfaces of phenol with $Mg^{2+}, Ca^{2+}, Ag^{+}, Zn^{2+}$ probes.

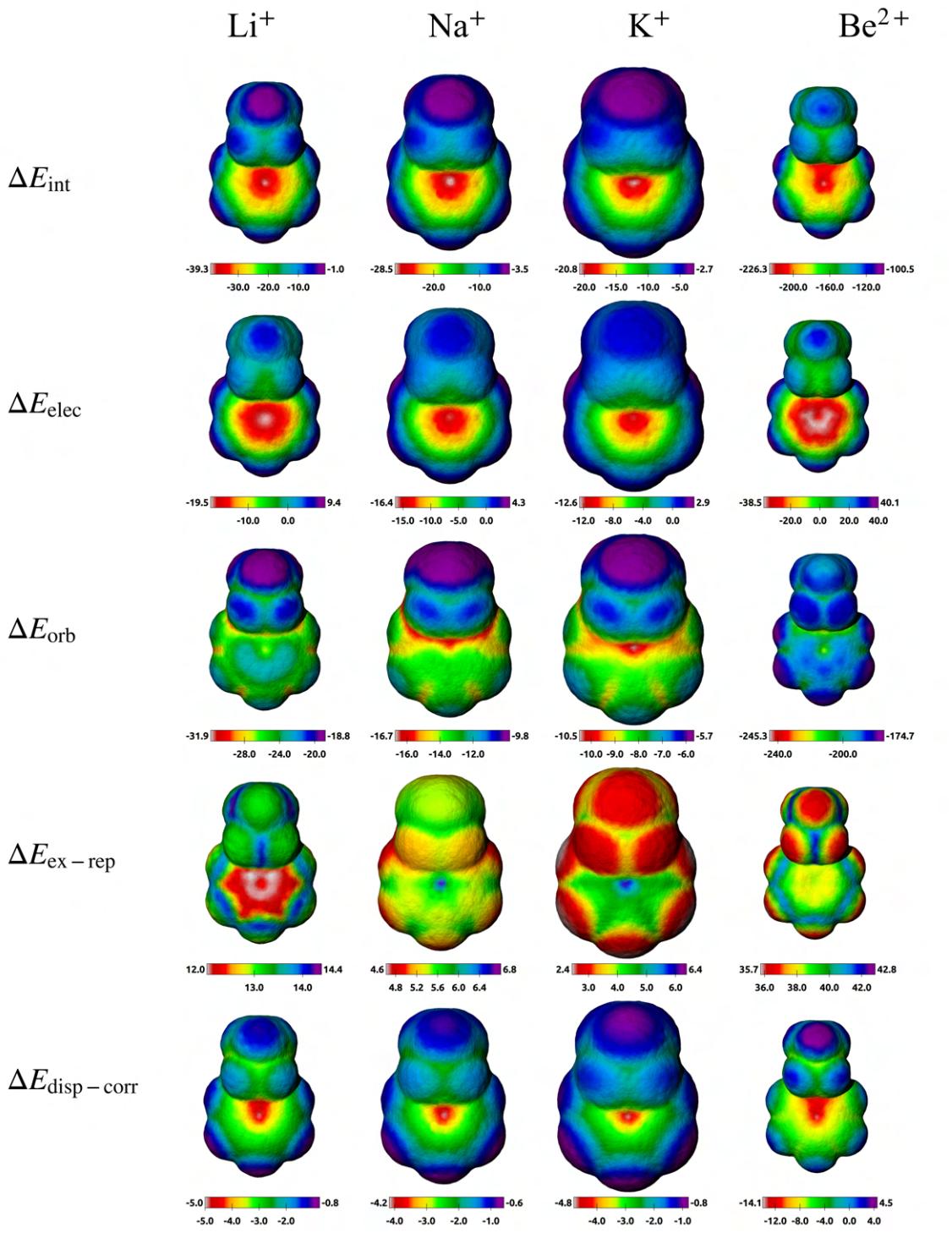

Figure S45. ΔE_{int}, ΔE_{elec}, ΔE_{orb}, $\Delta E_{\text{ex-rep}}$, and $\Delta E_{\text{disp-corr}}$ surfaces of n-propylbenzene with Li^+, Na^+, K^+, Be^{2+} probes.

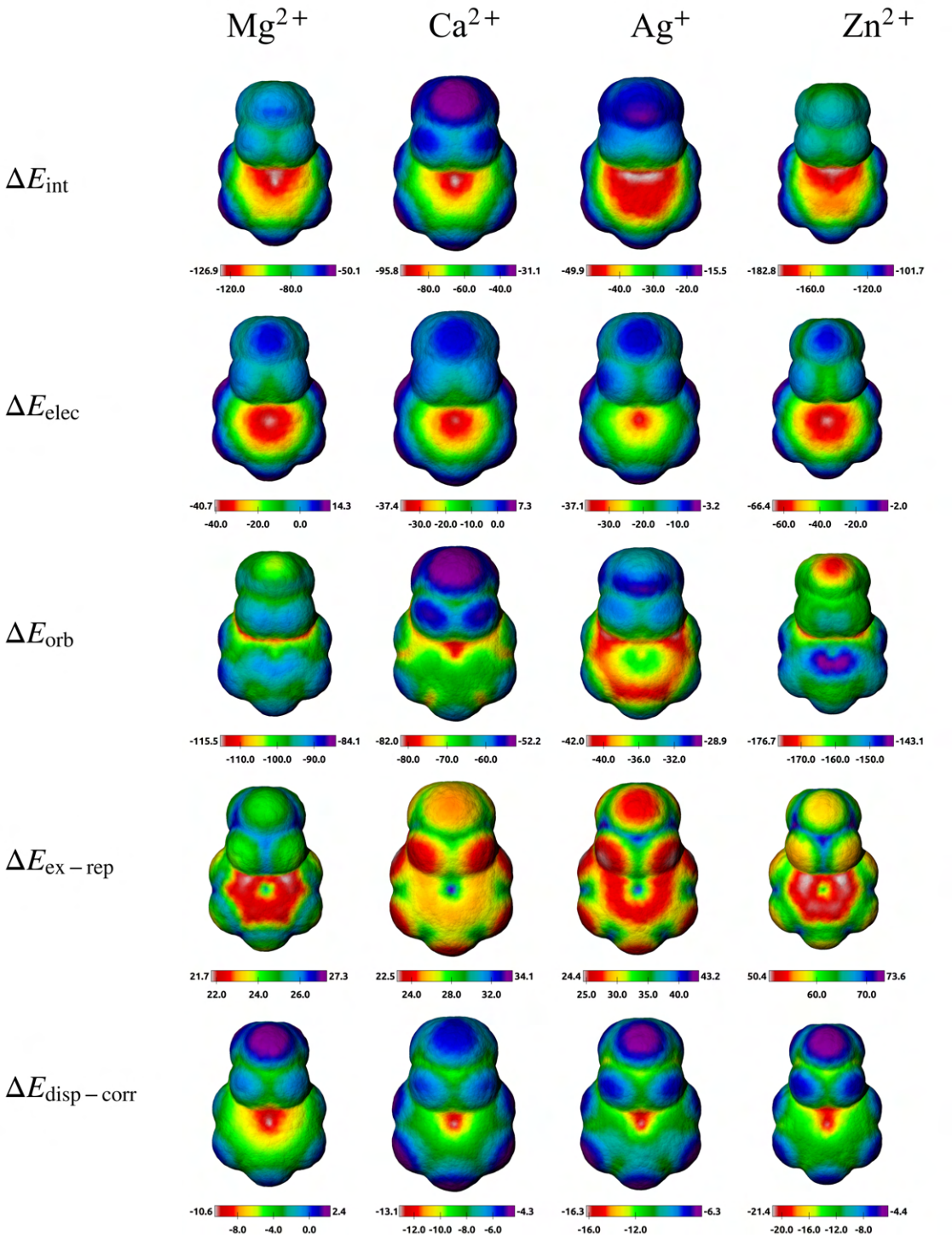

Figure S46. ΔE_{int}, ΔE_{elec}, ΔE_{orb}, $\Delta E_{\text{ex-rep}}$, and $\Delta E_{\text{disp-corr}}$ surfaces of n-propylbenzene with Mg^{2+}, Ca^{2+}, Ag^{+}, Zn^{2+} probes.

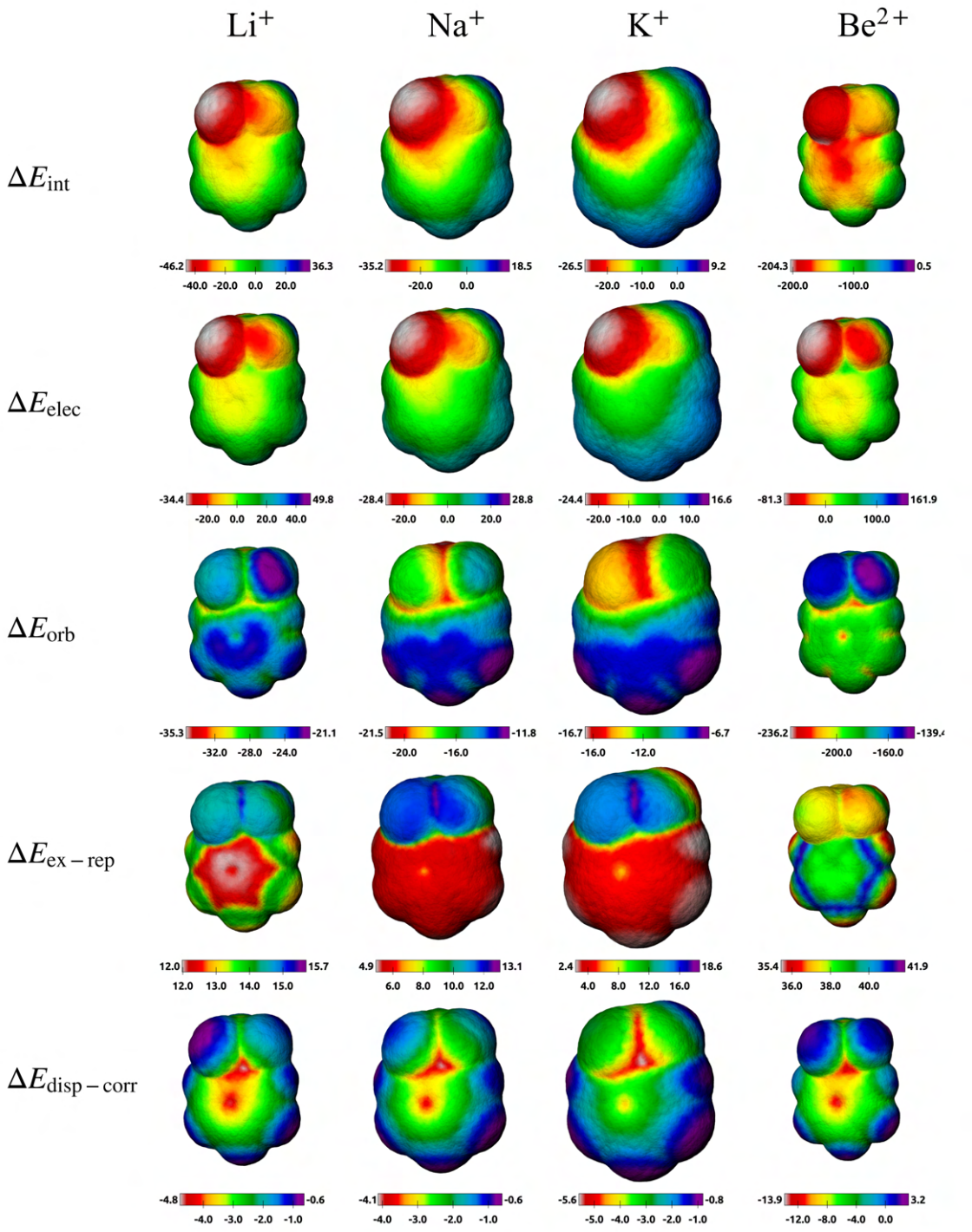

Figure S47. ΔE_{int}, ΔE_{elec}, ΔE_{orb}, $\Delta E_{\text{ex-rep}}$, and $\Delta E_{\text{disp-corr}}$ surfaces of benzenesulfonic acid with Li^+, Na^+, K^+, Be^{2+} probes.

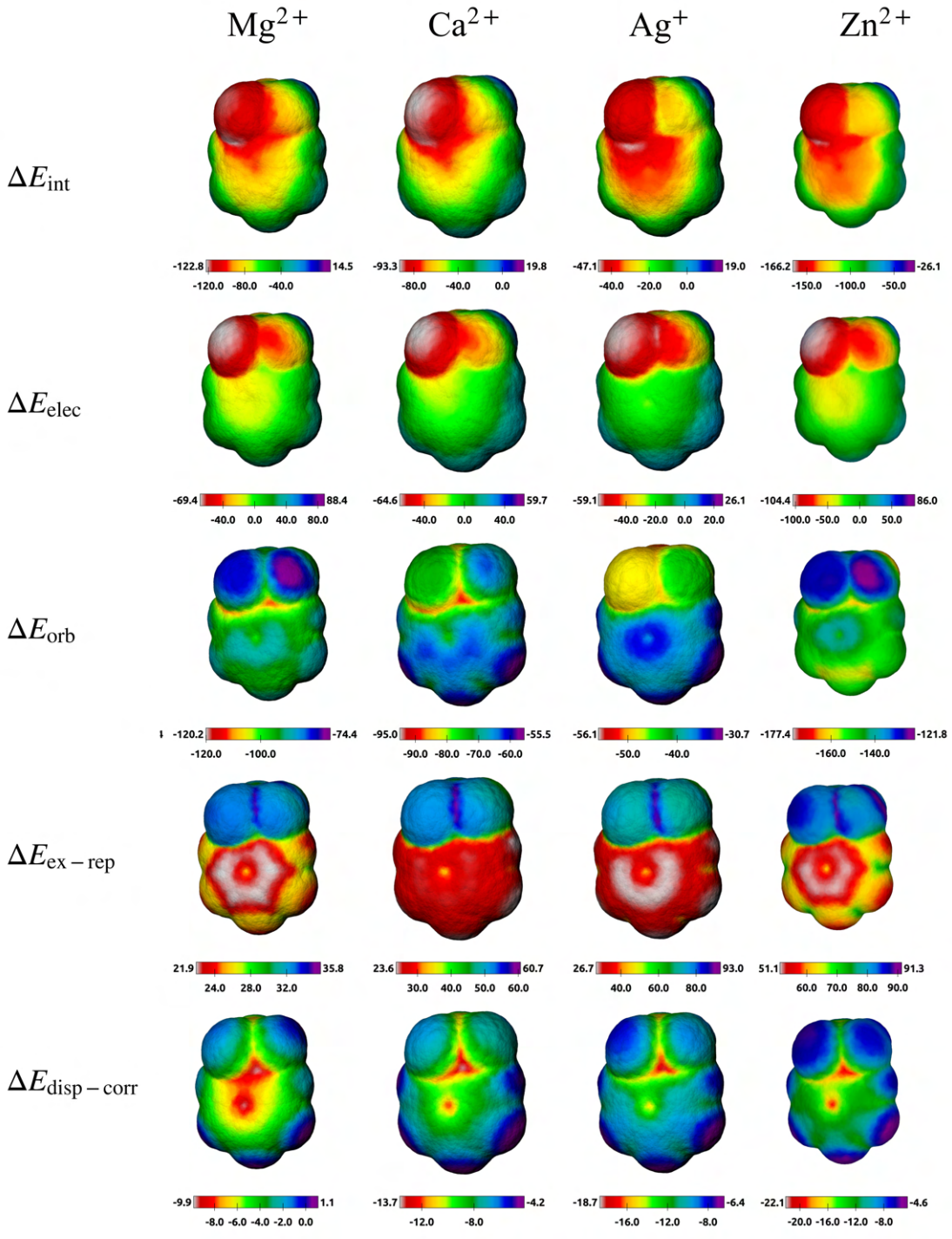

Figure S48. ΔE_{int}, ΔE_{elec}, ΔE_{orb}, $\Delta E_{\text{ex-rep}}$, and $\Delta E_{\text{disp-corr}}$ surfaces of benzenesulfonic acid with Mg^{2+}, Ca^{2+}, Ag^{+}, Zn^{2+} probes.

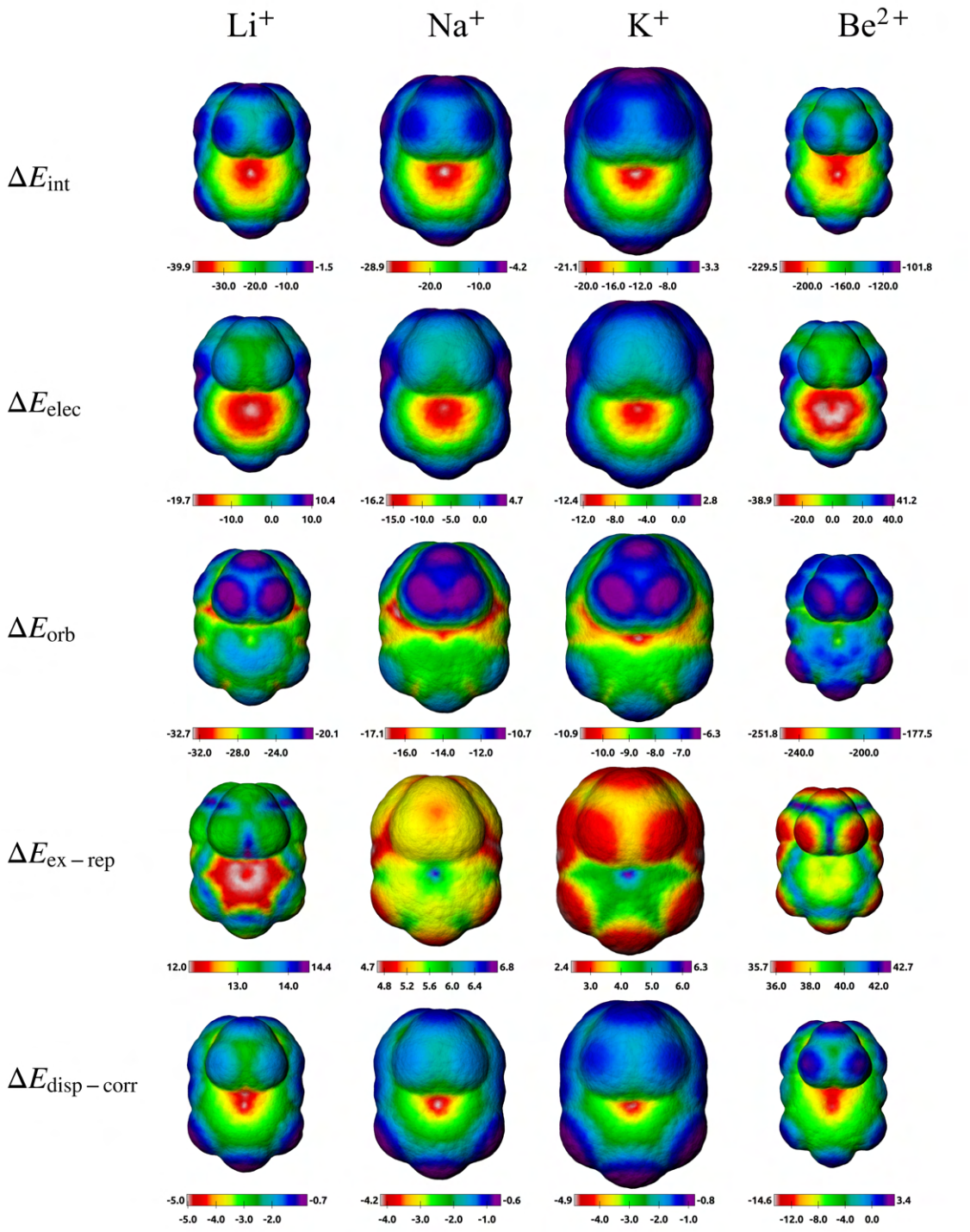

Figure S49. ΔE_{int}, ΔE_{elec}, ΔE_{orb}, $\Delta E_{\text{ex-rep}}$, and $\Delta E_{\text{disp-corr}}$ surfaces of tert – butylbenzene with Li^+, Na^+, K^+, Be^{2+} probes.

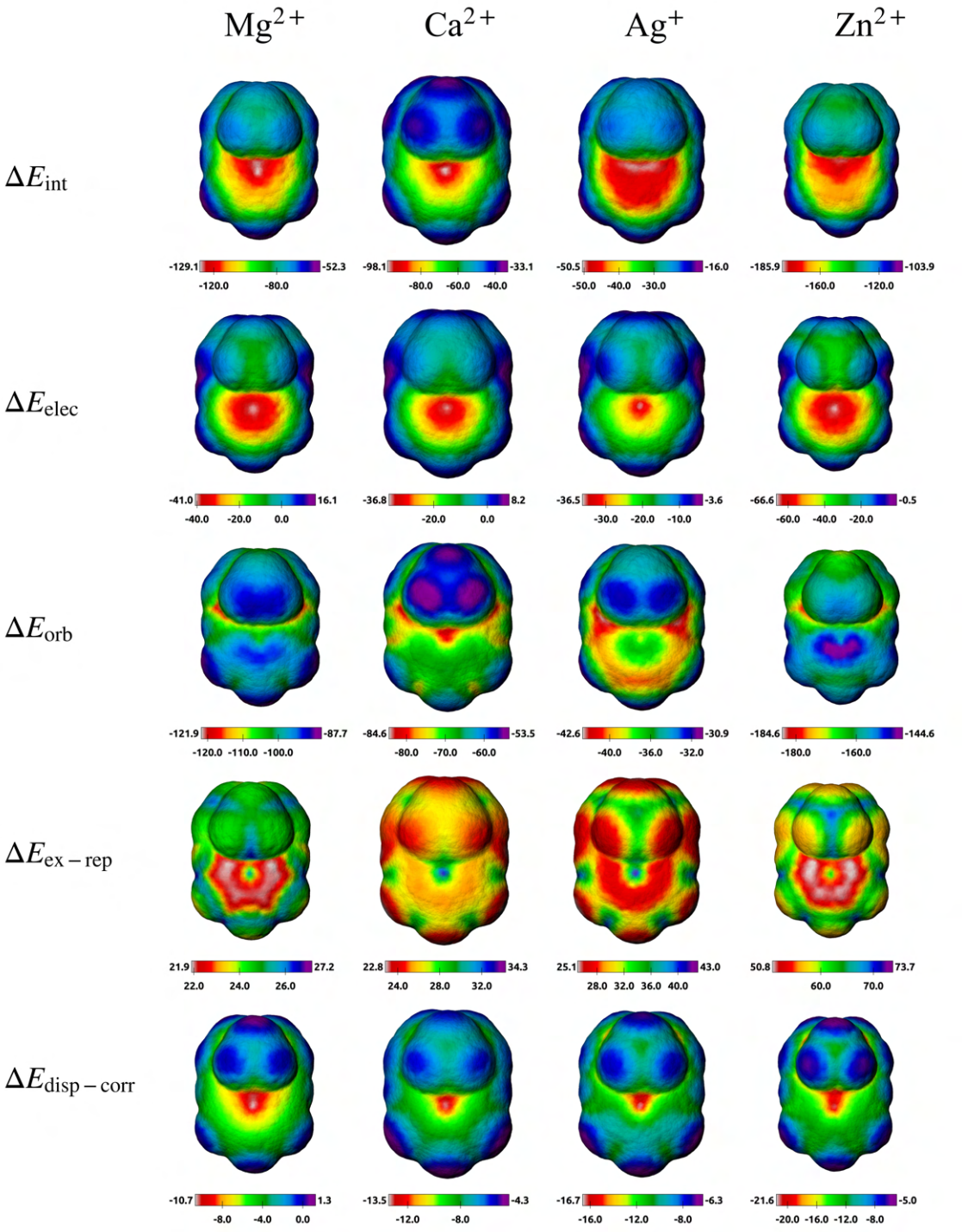

Figure S50. ΔE_{int}, ΔE_{elec}, ΔE_{orb}, $\Delta E_{\text{ex-rep}}$, and $\Delta E_{\text{disp-corr}}$ surfaces of tert – butylbenzene with Mg^{2+}, Ca^{2+}, Ag^{+}, Zn^{2+} probes.

The surfaces of mono-substituted benzene derivatives (S51) with a Na^+ probe reveal that the interaction is strongest with donating groups (NH2) and weakest with withdrawing groups (CN). The variation in ΔE_{int} tracks with ΔE_{elec}, indicating the influence is primarily electrostatic.

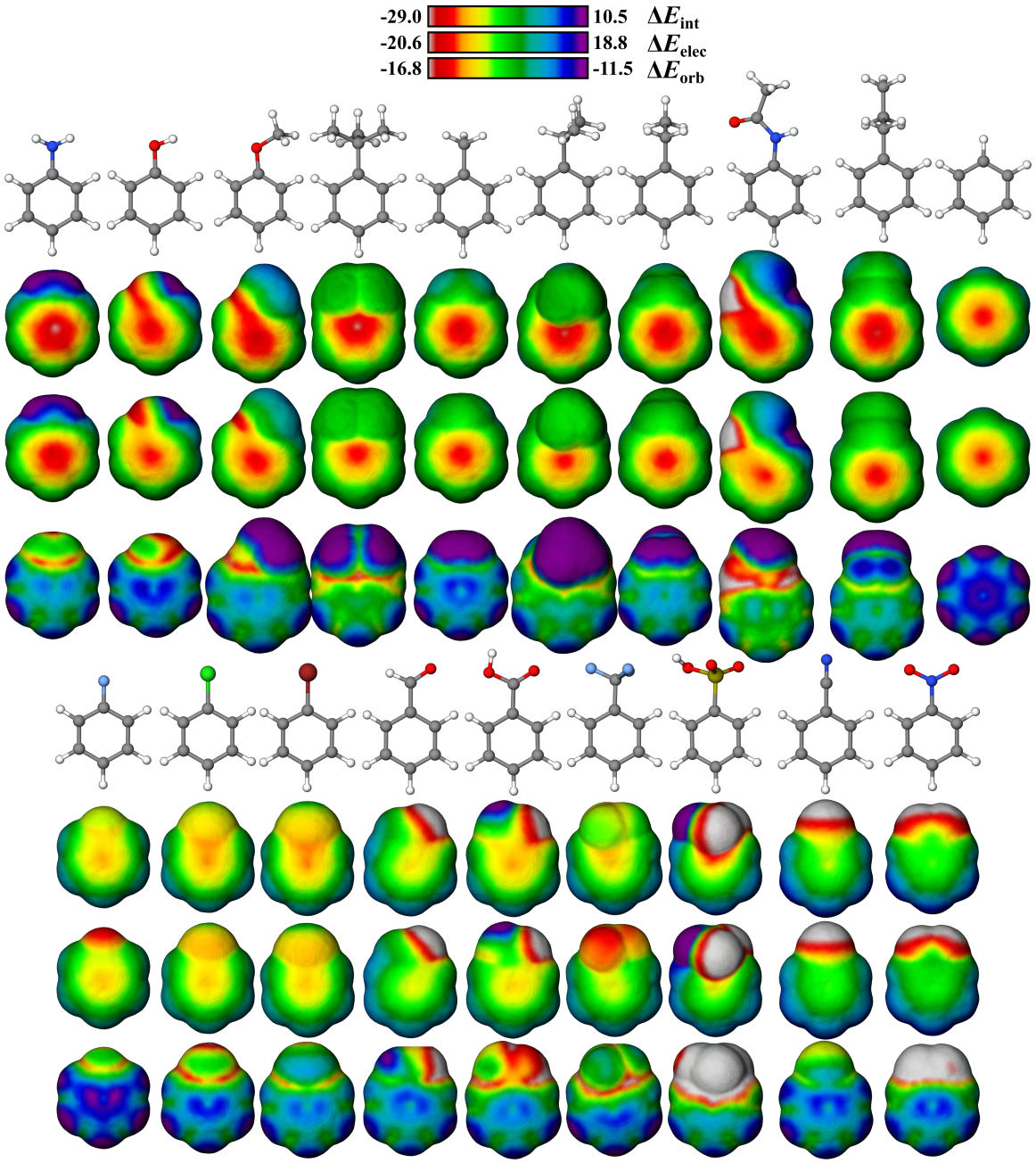

Figure S51. ΔE_{int}, ΔE_{elec}, and ΔE_{orb} surfaces of variable benzene derivatives with Na^+ probes. A constant scale is used to demonstrate substituent effects on energetics.

Furthermore, Hammett plots of ΔE_{int} and ΔE_{elec} vs. σ_{total} show strong correlation coefficients of 0.929 and 0.947 (**Figure. S52**), for benzene derivatives with Na^+, respectively. ΔE_{int} was collected from the surface region of the surface corresponding to the most favorable interaction energy within the arene π-system. ΔE_{elec} is the electrostatic component of ΔE_{int}. ΔE_{orb} did not correlate well. These results suggest that the strength of cation-π binding is strongly correlated with electrostatic effects brought on by introducing substituents and that orbital effects have minimal impact on binding strength trends.

Table S3. σ_{para}, σ_{meta}, and σ_{total} values for various benzene derivatives

	$-NH_2$	-OH	$-OCH_3$	$-$tBu	-Pr	-iPr	-Et	Bz
σ_{para}	-0.16	0.12	0.12	-0.1	-0.07	-0.07	-0.07	0
σ_{meta}	-0.66	-0.37	-0.27	-0.2	-0.13	-0.15	-0.15	0
σ_{total}	-0.82	-0.25	-0.15	-0.3	-0.2	-0.22	-0.22	0
	-CN	-COOH	-F	-Cl	-Br	-I	-CHO	
σ_{para}	0.56	0.38	0.34	0.37	0.39	0.35	0.35	
σ_{meta}	0.66	0.5	0.06	0.23	0.23	0.18	0.42	
σ_{total}	1.22	0.88	0.4	0.6	0.62	0.53	0.77	

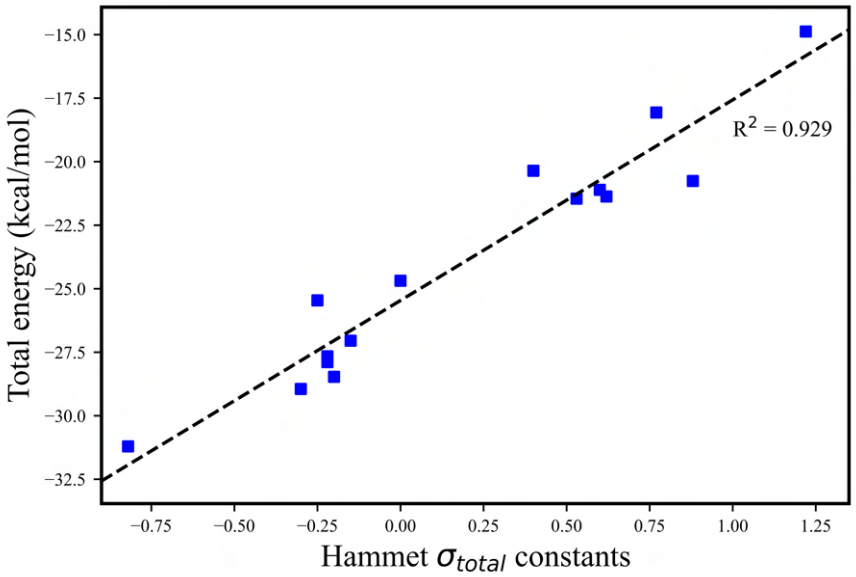

(a) ΔE_{elec} vs. σ_{total}

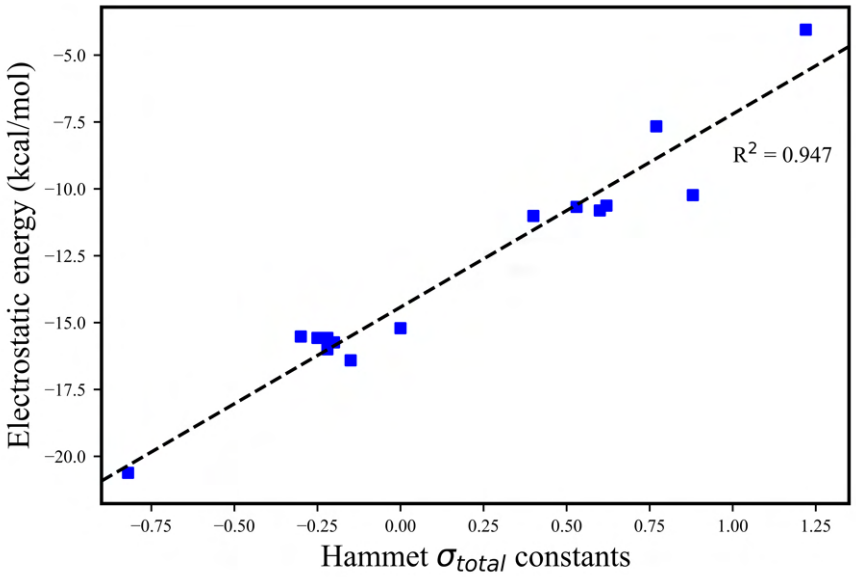

(b) ΔE_{int} vs. σ_{total}

Figure S52. Hammett plots of benzene derivatives illustrating the relationships between different energy terms and σ_{total}: (1) ΔE_{elec} vs. σ_{total} and (2) ΔE_{int} vs. σ_{total}.

10. IMIP surfaces generated with halide probes

Figures S53-S57 depict surfaces representing interactions between various halogens (F^-, Cl^-, Br^-, and I^-) and molecules known for their anion-π interactions. These molecules include hexafluorobenzene, triazine, trifluorotriazine, trinitrobenzene, and 1,2,4,5-tetracyanobenzene. Isodensities for these surfaces were established at the center of the trinitrobenzene molecule, following a restricted optimization for each halogen probe. The isodensities are listed in **Table S4**.

Table S4. Isodensities of various anion probes based on optimized interactions with benzene.

Probe	F^-	Cl^-	Br^-	I^-
Isodensity	5.62×10^{-5}	1.22×10^{-6}	$2 \times 10^{--7}$	3.15×1^{-8}

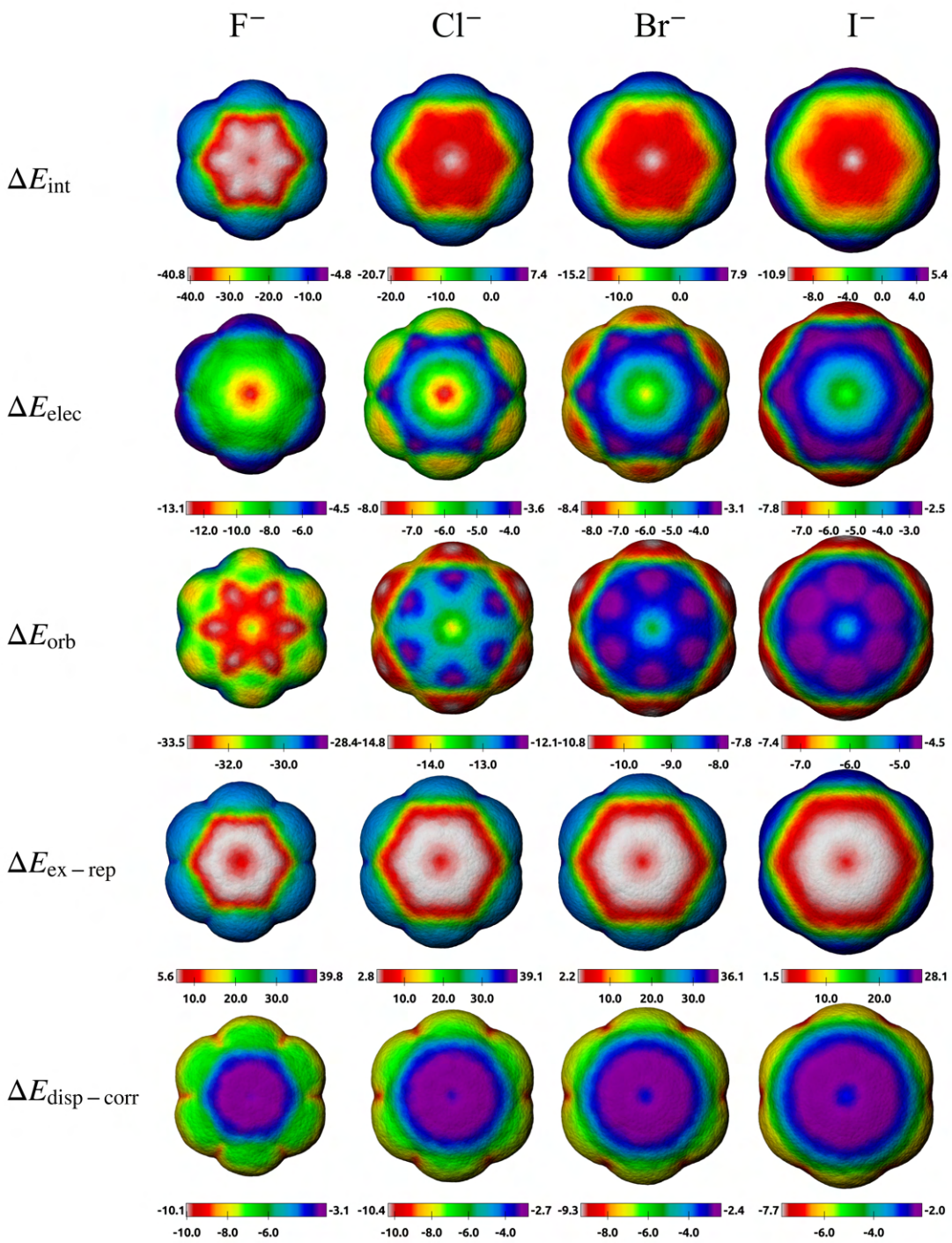

Figure S53. ΔE_{int}, ΔE_{elec}, ΔE_{orb}, $\Delta E_{\text{ex-rep}}$, and $\Delta E_{\text{disp-corr}}$ surfaces of hexflourobenzene with F^-, Cl^-, Br^-, I^- probes.

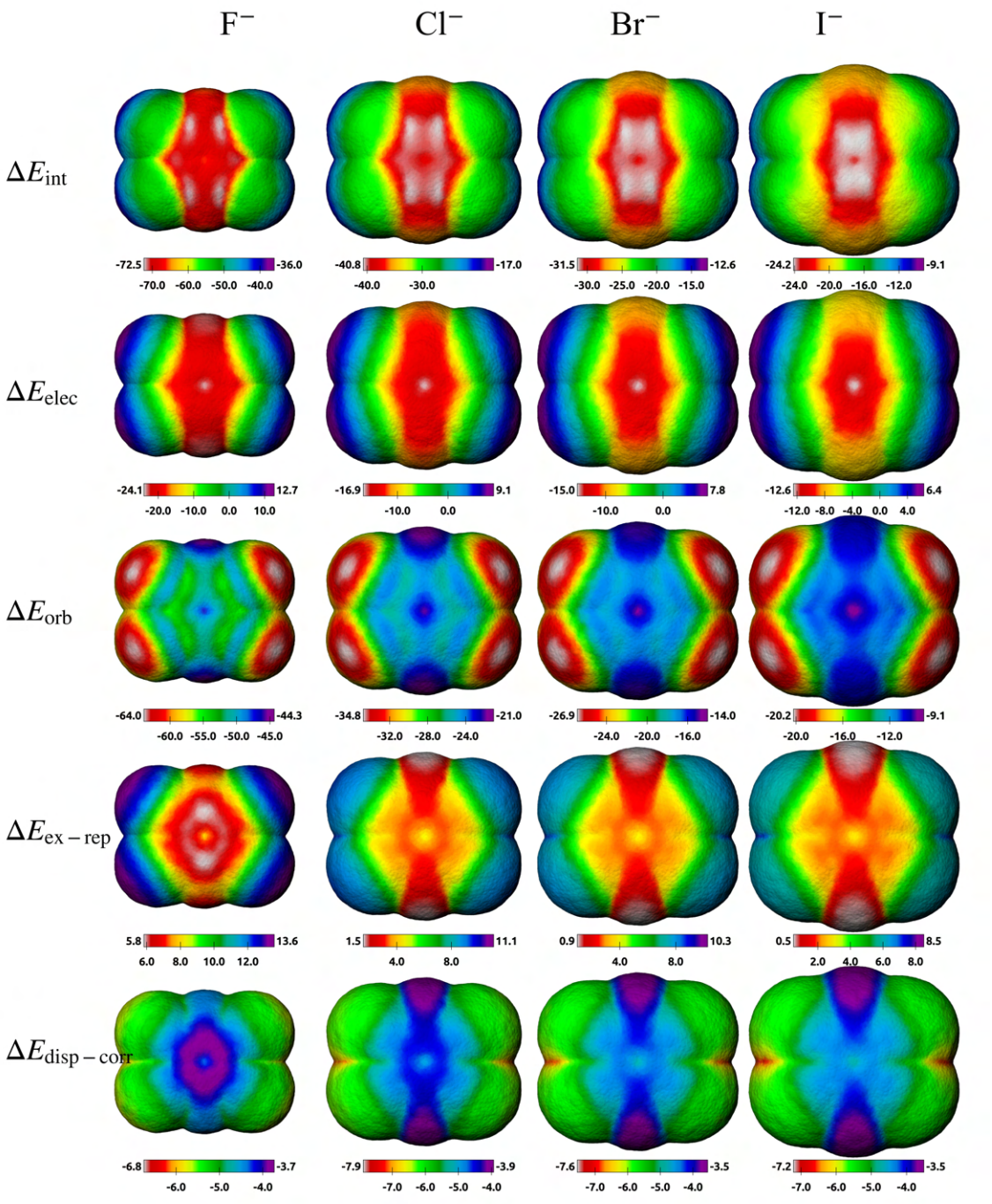

Figure S54. ΔE_{int}, ΔE_{elec}, ΔE_{orb}, $\Delta E_{\text{ex-rep}}$, and $\Delta E_{\text{disp-corr}}$ surfaces of 1,2,4,5-tetracyanobenzene with F^-, Cl^-, Br^-, I^- probes.

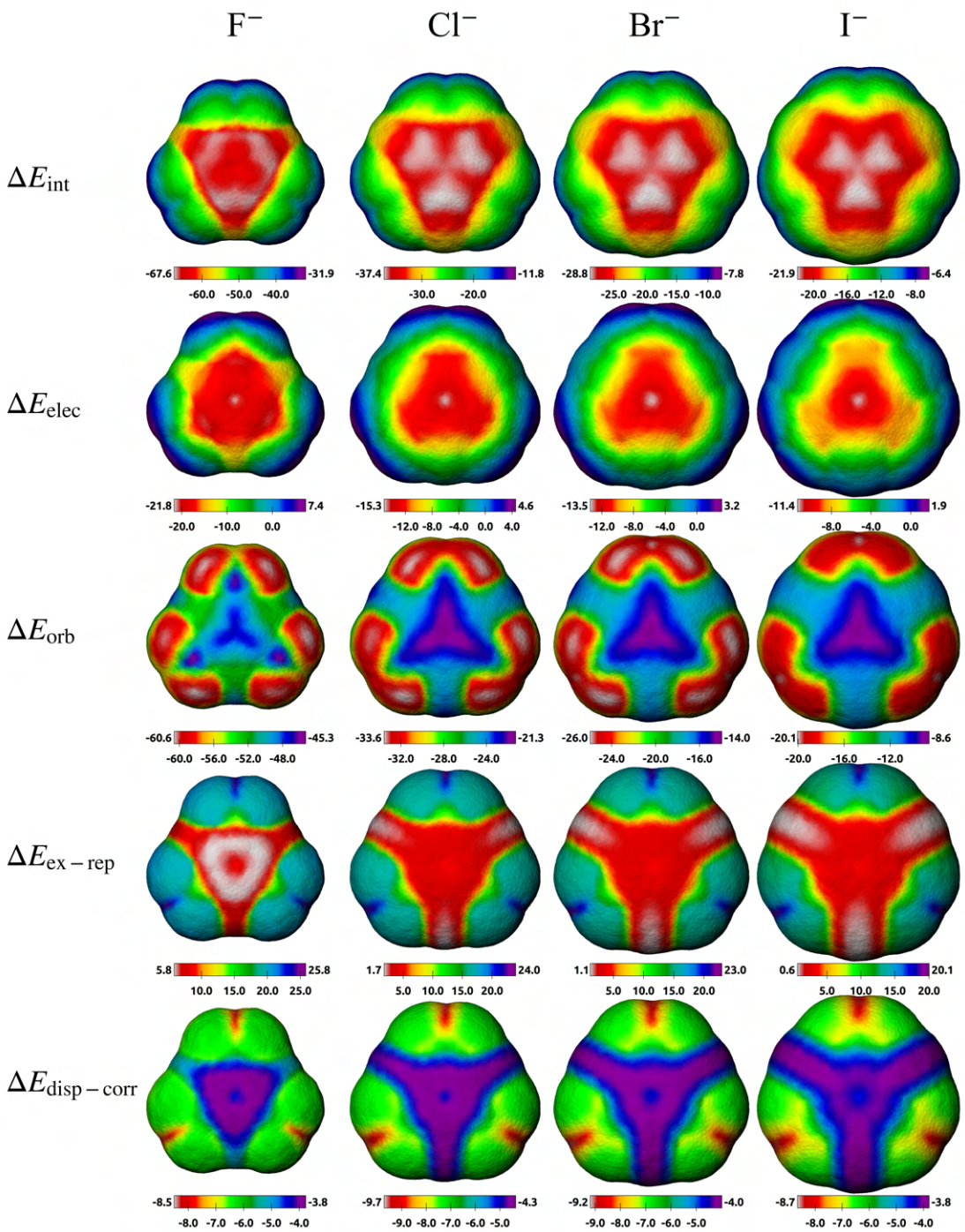

Figure S55. ΔE_{int}, ΔE_{elec}, ΔE_{orb}, $\Delta E_{\text{ex-rep}}$, and $\Delta E_{\text{disp-corr}}$ surfaces of 1,3,5-trinitrobenzene with F^-, Cl^-, Br^-, I^- probes.

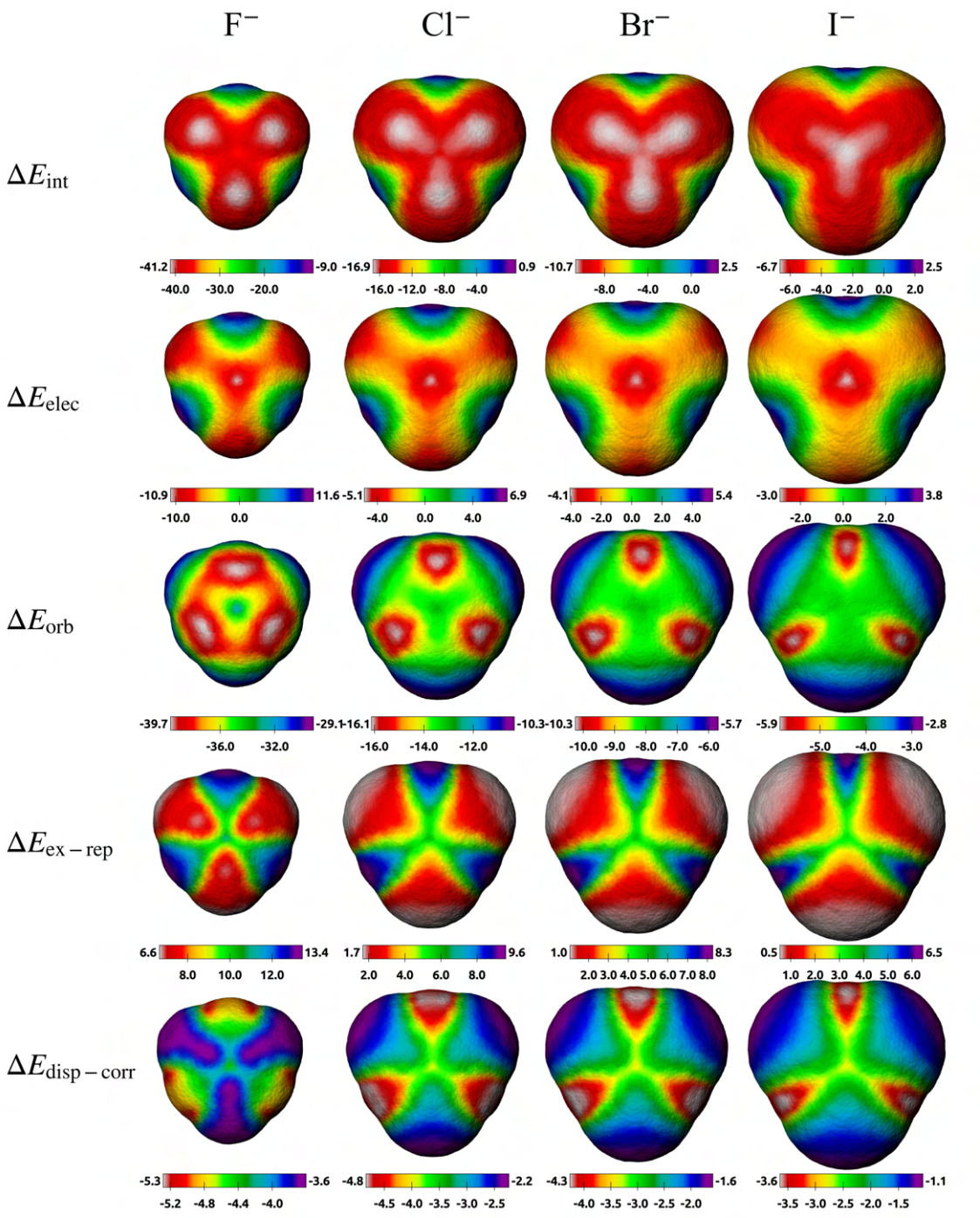

Figure S56. ΔE_{int}, ΔE_{elec}, ΔE_{orb}, $\Delta E_{\text{ex-rep}}$, and $\Delta E_{\text{disp-corr}}$ surfaces of triazine with F^-, Cl^-, Br^-, I^- probes.

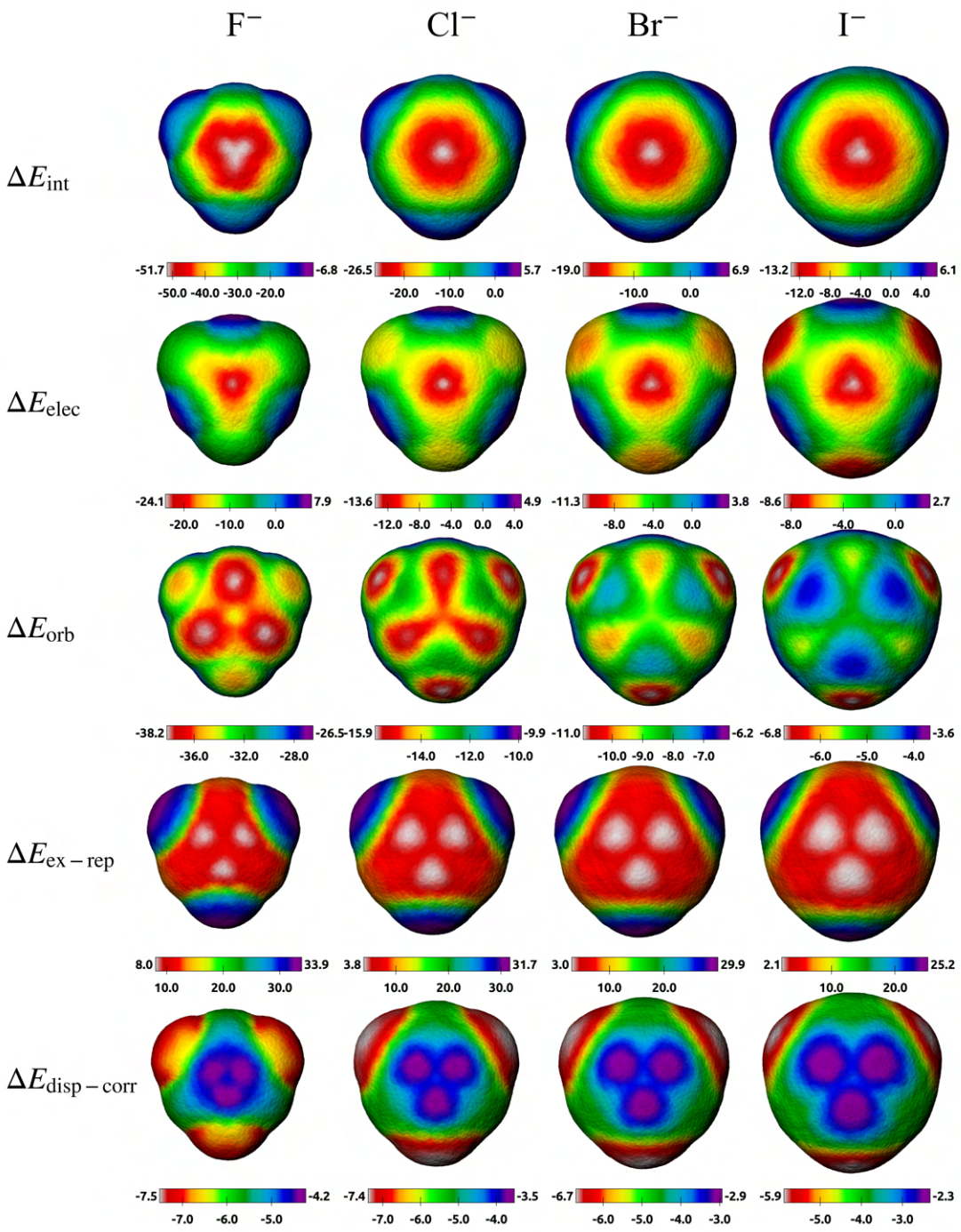

Figure S57. ΔE_{int}, ΔE_{elec}, ΔE_{orb}, $\Delta E_{\text{ex-rep}}$, and $\Delta E_{\text{disp-corr}}$ surfaces of trifluoroazine with F^-, Cl^-, Br^-, I^- probes.

11. Pd-allyl complexes

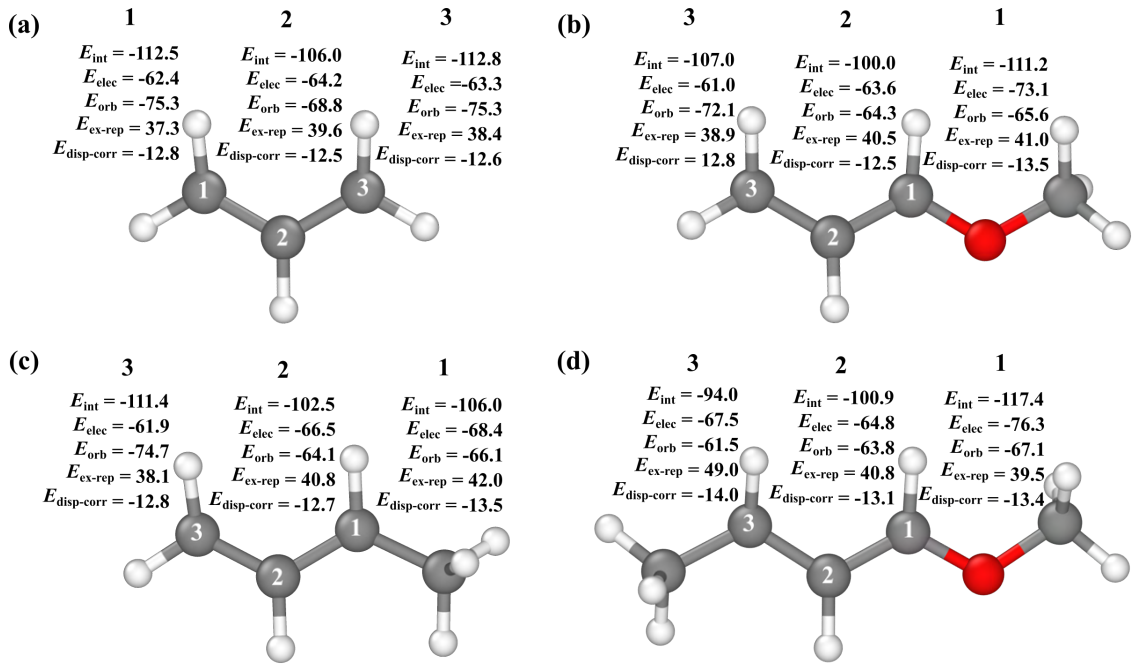

Figure S58. Most favorable interaction energies mapped onto each atom within the allyl portion of the Pd-allyl transition metal complexes, selecting and mapping the most favorable interaction within the region of each atom for: (a) unsubstituted, (b) methoxy-substituted, (c) methyl-substituted, and (d) 1-methoxy-3-methyl configurations.